AEROELASTIC ANALYSES AND TESTS OF A WING LIKE STRUCTURE WITH PAYLOAD

A THESIS SUBMITTED TO
THE GRADUATE SCHOOL OF NATURAL AND APPLIED SCIENCES
OF
MIDDLE EAST TECHNICAL UNIVERSITY

BY

ÖZGÜR SERIN

IN PARTIAL FULFILLMENT OF THE REQUIREMENTS
FOR
THE DEGREE OF MASTER OF SCIENCE
IN
AEROSPACE ENGINEERING

JULY 2019

Approval of the thesis:

AEROELASTIC ANALYSES AND TESTS OF A WING LIKE STRUCTURE WITH PAYLOAD

submitted by **ÖZGÜR SERIN** in partial fulfillment of the requirements for the degree of **Master of Science in Aerospace Engineering Department, Middle East Technical University** by,

Prof. Dr. Halil Kalıpçılar
Dean, Graduate School of **Natural and Applied Sciences**

Prof. Dr. İsmail Hakkı Tuncer
Head of Department, **Aerospace Engineering**

Assist. Prof. Dr. Mustafa Perçin
Supervisor, **Aerospace Engineering, METU**

Examining Committee Members:

Prof. Dr. Altan Kayran
Aerospace Engineering, METU

Assist. Prof. Dr. Mustafa Perçin
Aerospace Engineering, METU

Prof. Dr. Oğuz Uzol
Aerospace Engineering, METU

Assoc. Prof. Dr. Melin Şahin
Aerospace Engineering, METU

Assist. Prof. Dr. Seher Eken
Aerospace Engineering, SAMU

Date: 05.07.2019

I hereby declare that all information in this document has been obtained and presented in accordance with academic rules and ethical conduct. I also declare that, as required by these rules and conduct, I have fully cited and referenced all material and results that are not original to this work.

Name, Surname: Özgür Serin

Signature:

ABSTRACT

AEROELASTIC ANALYSES AND TESTS OF A WING LIKE STRUCTURE WITH PAYLOAD

Serin, Özgür
Master of Science, Aerospace Engineering
Supervisor: Assist. Prof. Dr. Mustafa Perçin

July 2019, 143 pages

In this study, a wing-like structure with three payloads was examined from the point of flutter characteristic by performing frequency domain flutter analyses in a commercial software ZAERO© and conducting wind tunnel flutter tests in Ankara Wind Tunnel (ART) test facility. Based upon the aeroelastic certification flow admitted by the independent aviation authorities being active across the globe, for each configuration of the wing-like structure, finite element models were created using Altair Hypermesh© software, finite element modal analyses were realized with the solver of MSC Nastran© and ground vibration tests were conducted with Simcenter Scadas© data acquisition system. For the purpose of obtaining more accurate flutter analysis results, required finite element models of the configurations were modal updated per the ground vibration test results. Afterwards, the flutter onset speeds and frequencies for each configuration were acquired with the flutter analyses realized by applying the finite element modal analysis results of both updated and non-updated finite element models. All these outputs were compared with the flutter onset speeds and frequencies ascertained in the wind tunnel tests and consistency between the analysis and the test was investigated. In addition, the influence of the installation of three payloads to the wing-like structure in different combinations was studied in the sense of flutter behavior and the reasons of unexpected results were interpreted by further analysis and tests.

Keywords: Aeroelasticity, Flutter Analysis, Ground Vibration Test, Modal Updating, Wind Tunnel Flutter Test

ÖZ

FAYDALI YÜK ENTEGRE EDİLMİŞ KANAT BENZERİ BİR YAPININ AEROELASTİK ANALİZ VE TESTLERİ

Serin, Özgür
Yüksek Lisans, Havacılık ve Uzay Mühendisliği
Tez Danışmanı: Dr. Öğr. Üyesi Mustafa Perçin

Temmuz 2019, 143 sayfa

Bu çalışmada, üzerine üç farklı faydalı yük entegre edilmiş kanat benzeri bir yapı, ticari bir yazılım olan ZAERO© ile frekans tabanlı çırpıntı analizleri yapılarak ve Ankara Rüzgâr Tüneli (ART) test merkezinde rüzgâr tüneli çırpıntı testleri gerçekleştirilerek çırpıntı karakteristiği yönünden incelenmiştir. Dünya genelinde faaliyet gösteren bağımsız havacılık otoriteleri tarafından kabul gören aeroelastik sertifikasyon akışı rehber alınarak, kanat benzeri yapının tüm konfigürasyonları için Altair Hypermesh© program kullanılarak sonlu elemanlar modeli oluşturulmuş, MSC Nastran© çözücüsü ile doğal frekans analizleri gerçekleştirilmiş ve Simcenter Scadas© veri toplama sistemi kullanılarak yer titreşim testleri yapılmıştır. Daha doğru çırpıntı analiz sonuçları elde etmek amacıyla, gerek duyulan konfigürasyonların sonlu eleman modelleri modal test sonuçlarına göre güncellenmiştir. Daha sonra güncellenmiş ve güncellenmemiş model doğal frekans analiz sonuçları kullanılarak gerçekleştirilen çırpıntı analizleri ile her bir konfigürasyonun çırpıntı başlangıç hızı ve frekansı hesaplanmıştır. Tüm bu sonuçlar rüzgâr tüneli testleri sırasında tespit edilen çırpıntı hızları ve frekansları ile karşılaştırılmış ve analiz-test tutarlılığı incelenmiştir. Ek olarak, üç farklı faydalı yükün kanat benzeri yapı üzerine farklı kombinasyonlarda entegre edilmesinin çırpıntı karakteristiği açısından etkisi incelenmiş ve beklenmedik sonuçların nedenleri ilave analiz ve test çalışmaları ile izah edilmiştir.

Anahtar Kelimeler: Aeroelastisite, Çırpıntı Analizi, Yer Titreşim Testi, Modal Güncelleme, Rüzgâr Tüneli Çırpıntı Testi

To my lover and family

ACKNOWLEDGEMENTS

Throughout the preparation of this thesis I have received considerable support and assistance. I would first like to express my gratitude and indebtedness to my supervisor Asst. Prof. Dr. Mustafa Perçin for his guidance, encouragement and patience in the course of writing the thesis. I wish also to acknowledge the assistance and advices provided by Prof. Dr. Altan Kayran.

I am profoundly grateful to my colleague and my friend Mr. Kurtuluş Ersoy for his guidance, positive and helpful criticisms and motivation. I will never forget the moral and material support he has given in difficult times. I also would like to thank to my leader Mr. Cem Genç for his help, advice and tolerance. Suggestions provided by my other colleague Mr. Mert Atasoy was greatly appreciated.

The study presented in this thesis was a part of a research objective proposed by ASELSAN A. Ş. I would like to offer my special thanks to ASELSAN for allowing me to make this study possible and bringing all computational and testing capabilities into my utilization. I would like to extend my special thanks to my director Mr. Tahir Fidan and my manager Mr. Suphi Yılmaz for their valuable support. I wish also to thank to my colleagues Mr. Tuğcan Selimhocaoğlu, Mr. Orhun Yıldız and Mr. Şenol Urgancı for their coorperation in testing and manufacturing phase.

I am especially grateful to my parents Nursel Serin and Feti Serin, my sister Ayşegül Serin and my uncle Haşim Becerik for their endless support during my educational life.

My acknowledgement will never be complete without special mention of a very valuable person for me, my lover and my wife Melis Tekiner. I am particularly grateful for her love and constant support and for keeping me sane over past few months.

TABLE OF CONTENTS

ABSTRACT v

ÖZ vii

ACKNOWLEDGEMENTS x

TABLE OF CONTENTS xi

LIST OF TABLES xiv

LIST OF FIGURES xvi

1. INTRODUCTION 1
   - 1.1. General Introduction 1
   - 1.2. History of Aeroelasticity 5
   - 1.3. Literature Survey 16
   - 1.4. Aeroelastic Certification 19
     - 1.4.1. Military Specifications 19
     - 1.4.2. Civil Regulations 20
   - 1.5. Aim and Structure of the Thesis 23
2. THEORY 27
   - 2.1. General Introduction 27
   - 2.2. Potential Flow 27
   - 2.3. Steady Flow 33
   - 2.4. Unsteady Flow 43
   - 2.5. Aeroelastic Background of ZAERO© 47
     - 2.5.1. ZAERO© Overview 47
     - 2.5.2. Aeroelastic Foundation of ZAERO© 48

2.5.3. Flutter Solution Techniques 54

2.5.3.1. K-Method 54

2.5.3.2. P-K Method 55

2.5.3.3. g-Method 56

3. WING-LIKE STRUCTURE AND DESIGN DETAILS 59

3.1. General Introduction 59

3.2. General Dimensions and Assembly of the Subparts 60

3.3. Materials 63

3.4. Definitions of the Configurations 63

4. DYNAMIC MODEL GENERATION 65

4.1. General Introduction 65

4.2. Finite Element Modal Analysis 65

4.2.1. Finite Element Modelling 65

4.2.2. Numerical Natural Frequencies and Mode Shapes of the Wing 67

4.3. Ground Vibration Test 69

4.3.1. Test Setup 69

4.3.2. Ground Vibration Test Results 72

4.4. Modal Updating 74

4.4.1. Correlation of Finite Element Analysis and Ground Vibration Test Results 74

4.4.2. Modal Updating Parameters and Responses 76

4.4.3. Modal Updating Results 77

5. FLUTTER SUBSTANTIATION 79

5.1. General Introduction 79

5.2. Flutter Analysis 79

5.2.1. Aerodynamic Model 79

5.2.2. Spline of the Aerodynamic and Structural Models..................................80

5.2.3. Flutter Analysis Parameters and Solution Method 82

5.2.4. Flutter Analysis Results 83

5.2.4.1. Non-updated Model 83

5.2.4.2. Updated Model..85

5.3. Wind Tunnel Flutter Test 87

5.3.1. Test Setup 87

5.3.2. Wind Tunnel Flutter Test Results...89

6. DISCUSSION AND INFERENCES 93

6.1. General Introduction...93

6.2. Comparison of Flutter Analysis and Test Results 93

6.3. The Effects of the Payload Configurations on the Flutter Results 94

6.4. The Effects of the Rigid Pylons on the Flutter Results 96

6.4.1. Flutter Analysis of Configuration-1 with Narrower Pylons 96

6.4.2. Wind Tunnel Flutter Test Results of Configuration-7 with Upper and Lower Pylons 97

7. CONCLUSION...99

7.1. General Conclusion 99

7.2. Recommendations for Future Works 100

REFERENCES..103

LIST OF TABLES

TABLES

Table 3-1 Materials 63

Table 4-1 Element Types and Sizes 66

Table 4-2 Finite Element Model Information 66

Table 4-3 Numerical Natural Frequencies 68

Table 4-4 Ground Vibration Test Mode Frequencies and Modal Damping 73

Table 4-5 Comparison of the Finite Element Modal Analysis and Ground Vibration Test Mode Frequencies 75

Table 4-6 Modal Assurance Criteria between Finite Element Modal Analysis and Ground Vibration Test Mode Shapes 76

Table 4-7 Configuration-6 Modal Updating Results 77

Table 5-1 Aerodynamic Model Information 80

Table 5-2 Spline Modelling Details 80

Table 5-3 Flutter Analysis Results with Non-updated Model, Onset Speeds and Frequencies 84

Table 5-4 Flutter Analysis Results with Updated Model, Onset Speeds and Frequencies of Configuration-6 85

Table 5-5 Wind Tunnel Flutter Test Results 90

Table 6-1 Comparison of the Flutter Analysis and the Wind Tunnel Test Results ... 93

Table 6-2 Comparison of Finite Element Modal Analysis Results of the Configuration-1 with Shorter Pylons and the Original Configuration-1 96

Table 6-3 Comparison of Zero Damping Flutter Analysis Results of the Configuration-1 with Narrower Pylons and the Original Configuration-1 97

Table 6-4 Comparison of Wind Tunnel Flutter Test Results of the Configuration-7 with Upper and Lower Pylons and the Original Configuration-7 97

Table 0-1 Finite Element Modal Analysis Results According to Different Mesh Densities 114

Table 0-2 Finite Element Modal Analysis Results with and without Transducers..115

LIST OF FIGURES

FIGURES

Figure 1-1 Leonardo Da Vinci Primitive Aircraft Design Sketches [1] 2

Figure 1-2 The First Flight of Wright Brothers [4] 2

Figure 1-3 Collar’s Aeroelastic Triangle[5] 4

Figure 1-4 Aeroelastic Phenomenon 5

Figure 1-5 Handley Page O/400 Bomber Biplane [11] 7

Figure 1-6 Albatros D-III Biplane Fighter [12] 7

Figure 1-7 Fokker D-VIII Monoplane Fighter [13] 8

Figure 1-8 von Schlippe’s Flight Flutter Test Techniques [6] 11

Figure 1-9 General Aeroelastic Certification Flow for Newly Designed Aircrafts ... 21

Figure 1-10 General Aeroelastic Certification Flow for Modified Aircrafts 22

Figure 1-11 The Work Flow in Present Thesis 24

Figure 2-1 Flow Around a Thin Airfoil 30

Figure 2-2 Velocity Profile in Boundary Layer 34

Figure 2-3 Infinitesimal Circulation in Boundary Layer 34

Figure 2-4 Surface Vortex Sheet at $t = 0^+$ 36

Figure 2-5 Surface and Wake Vortex Sheet at $t > 0$ 36

Figure 2-6 Vortex Sheet Modeling about an Airfoil 37

Figure 2-7 Circulation Calculation 39

Figure 2-8 An Airfoil with Angle of Attack $\boldsymbol{\alpha}$ 42

Figure 2-9 Sources and Sinks on the Thin Airfoil 44

Figure 2-10 Bound and Wake Vortices 44

Figure 2-11 Thin Aerofoil undergoing Plunging and Pitching Motion 45

Figure 2-12 Theodorsen Function on Complex Plane 47

Figure 2-13 Aeroelastic Functional Diagram (Closed Loop) 49

Figure 2-14 Aerodynamic Panel Models in ZAERO© 52

Figure 3-1 General Dimensions of the Wing-Like Structure....................................61
Figure 3-2 Payload Design Details 61
Figure 3-3 Assembly of the Payload, Pylon and Wing-Like Structure 62
Figure 3-4 Fixture Design Details..62
Figure 3-5 Definitions of Configurations..64
Figure 4-1 Finite Element Model of Configuration-1...66
Figure 4-2 Fixed Boundary Conditions and CBUSH Definitions 67
Figure 4-3 Numerical 1st Bending Mode Shape of Configuration-1..........................68
Figure 4-4 Numerical Torsion Mode Shape of Configuration-1 68
Figure 4-5 Numerical 2nd Bending Mode Shape of Configuration-1.........................69
Figure 4-6 GVT Setup and Stick Model 71
Figure 4-7 Configuration-1 GVT Setup..72
Figure 4-8 Test 1st Bending Mode Shape of Configuration-1 73
Figure 4-9 Test Torsion Mode Shape of Configuration-1 73
Figure 4-10 Test 2nd Bending Mode Shape of Configuration-1................................74
Figure 5-1 Aerodynamic Model of Configuration-1...80
Figure 5-2 Interpolated 1st Bending Mode Shapes on Aerodynamic Panel Model....81
Figure 5-3 Interpolated Torsion Mode Shapes on Aerodynamic Panel Model 81
Figure 5-4 Interpolated 2nd Bending Mode Shapes on Aerodynamic Panel Model...82
Figure 5-5 Flutter Analysis with Non-updated Model, V-g Diagram of Configuration-1...84
Figure 5-6 Flutter Analysis with Non-updated Model, V-f Diagram of Configuration-1...85
Figure 5-7 Flutter Analysis with Updated Model, V-g Diagram of Configuration-6 86
Figure 5-8 Flutter Analysis with Updated Model, V-f Diagram of Configuration-6.86
Figure 5-9 Wind Tunnel Flutter Test Model of Configuration-1...............................88
Figure 5-10 Wind Tunnel Test Setup of Configuration-1..89
Figure 5-11 Strain Gage Time History of Configuration-1 During Flutter 90
Figure 5-12 Test Flutter Frequency of Configuration-1 Acquired from FFT of Strain Gage Data...91

Figure 0-1 Finite Element Model of Configuration-2 109
Figure 0-2 Finite Element Model of Configuration-3 109
Figure 0-3 Finite Element Model of Configuration-4 110
Figure 0-4 Finite Element Model of Configuration-5 110
Figure 0-5 Finite Element Model of Configuration-6 111
Figure 0-6 Finite Element Model of Configuration-7 111
Figure 0-7 Finite Element Model of Configuration-8 112
Figure 0-8 Finite Element Model with Mesh Density 1 113
Figure 0-9 Finite Element Model with Mesh Density 2 113
Figure 0-10 Finite Element Model with Mesh Density 3 114
Figure 0-11 PCB Piezotronics, Model 288D01, Mechanical Impedance Sensor 116
Figure 0-12 PCB Piezotronics, Model 356A16, Triaxial ICP Accelerometer 117
Figure 0-13 Analysis 1st Bending Mode Shape of Configuration-2 118
Figure 0-14 Analysis Torsional Mode Shape of Configuration-2 118
Figure 0-15 Analysis 2nd Bending Mode Shape of Configuration-2 118
Figure 0-16 Analysis 1st Bending Mode Shape of Configuration-3 119
Figure 0-17 Analysis Torsion Mode Shape of Configuration-3 119
Figure 0-18 Analysis 2nd Bending Mode Shape of Configuration-3 119
Figure 0-19 Analysis 1st Bending Mode Shape of Configuration-4 120
Figure 0-20 Analysis Torsion Mode Shape of Configuration-4 120
Figure 0-21 Analysis 2nd Bending Mode Shape of Configuration-4 120
Figure 0-22 Analysis 1st Bending Mode Shape of Configuration-5 121
Figure 0-23 Analysis Torsion Mode Shape of Configuration-5 121
Figure 0-24 Analysis 2nd Bending Mode Shape of Configuration-5 121
Figure 0-25 Analysis 1st Bending Mode Shape of Configuration-6 122
Figure 0-26 Analysis Torsion Mode Shape of Configuration-6 122
Figure 0-27 Analysis 2nd Bending Mode Shape of Configuration-6 122
Figure 0-28 Analysis 1st Bending Mode Shape of Configuration-7 123
Figure 0-29 Analysis Torsion Mode Shape of Configuration-7 123
Figure 0-30 Analysis 2nd Bending Mode Shape of Configuration-7 123

Figure 0-31 Analysis 1st Bending Mode Shape of Configuration-8 124

Figure 0-32 Analysis 2nd Bending Mode Shape of Configuration-8........................124

Figure 0-33 Analysis Torsion Mode Shape of Configuration-8 124

Figure 0-34 Test 1st Bending Mode Shape of Configuration-2 125

Figure 0-35 Test Torsion Mode Shape of Configuration-2 125

Figure 0-36 Test 2nd Bending Mode Shape of Configuration-2..............................125

Figure 0-37 Test 1st Bending Mode Shape of Configuration-3 126

Figure 0-38 Test Torsion Mode Shape of Configuration-3 126

Figure 0-39 Test 2nd Bending Mode Shape of Configuration-3..............................126

Figure 0-40 Test 1st Bending Mode Shape of Configuration-4 127

Figure 0-41 Test Torsion Mode Shape of Configuration-4 127

Figure 0-42 Test 2nd Bending Mode Shape of Configuration-4..............................127

Figure 0-43 Test 1st Bending Mode Shape of Configuration-5 128

Figure 0-44 Test Torsion Mode Shape of Configuration-5 128

Figure 0-45 Test 2nd Bending Mode Shape of Configuration-5..............................128

Figure 0-46 Test 1st Bending Mode Shape of Configuration-6 129

Figure 0-47 Test Torsion Mode Shape of Configuration-6 129

Figure 0-48 Test 2nd Bending Mode Shape of Configuration-6..............................129

Figure 0-49 Test 1st Bending Mode Shape of Configuration-7 130

Figure 0-50 Test Torsion Mode Shape of Configuration-7 130

Figure 0-51 Test 2nd Bending Mode Shape of Configuration-7..............................130

Figure 0-52 Test 1st Bending Mode Shape of Configuration-8 131

Figure 0-53 Test 2nd Bending Mode Shape of Configuration-8..............................131

Figure 0-54 Test Torsion Mode Shape of Configuration-8 131

Figure 0-55 V-g and V-f Diagrams of Configuration-2..133

Figure 0-56 V-g and V-f Diagrams of Configuration-3..133

Figure 0-57 V-g and V-f Diagrams of Configuration-4..133

Figure 0-58 V-g and V-f Diagrams of Configuration-5..134

Figure 0-59 V-g and V-f Diagrams of Configuration-6..134

Figure 0-60 V-g and V-f Diagrams of Configuration-7..134

Figure 0-61 V-g and V-f Diagrams of Configuration-8 135
Figure 0-62 Strain Gage Time History and Its FFT Result of Configuration-2 137
Figure 0-63 Strain Gage Time History and Its FFT Result of Configuration-3 138
Figure 0-64 Strain Gage Time History and Its FFT Result of Configuration-4 139
Figure 0-65 Strain Gage Time History and Its FFT Result of Configuration-5 140
Figure 0-66 Strain Gage Time History and Its FFT Result of Configuration-6 141
Figure 0-67 Strain Gage Time History and Its FFT Result of Configuration-7 142
Figure 0-68 Strain Gage Time History and Its FFT Result of Configuration-8 143

CHAPTER 1

INTRODUCTION

1.1. General Introduction

The human beings have always imagined themselves being able to fly, float among the clouds like a bird and see the earth surface as a carpet pattern since the very beginning of the recorded history. This craving has reflected to their histories and formed their sense or art. Especially the mythology of many cultures includes many allegorical and unsubstantial figures whom are capable of flying as a symbol of their so-called everlasting power. Myths and legends spreading through the mankind have had a great impact on this increasing desire; if one can fly, then he can get rid of his troubles on the earth and easily close to the gods.

This endless dream has come up with some primitive trails such as tower jumping which has unfortunately ended in serious injuries or deaths due to the lack of understanding of the theory underlying lift, stability and control in the later of first millennium. In the era of Renaissance some investigators eventually have begun to understand the basics of the aircraft design. Among them the most notable one belonged to Leonardo da Vinci who has studied the bird flight and comprehend the principles of aerodynamics in the last years of 15th century. He has sketched many designs for flying crafts including ornithopters, fixed-wing gliders and rotorcrafts (Figure 1-1).

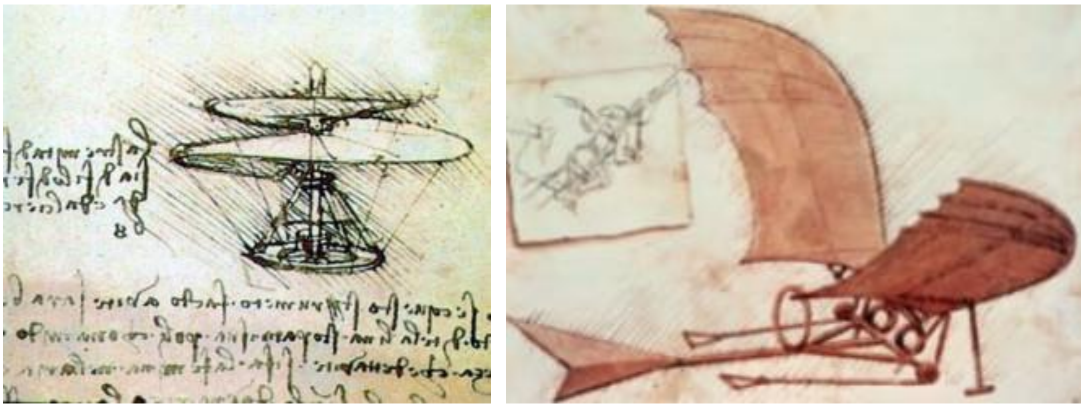

Figure 1-1 Leonardo Da Vinci Primitive Aircraft Design Sketches [1]

In opposition to the studies and experiences with wings, the first flight of humans has been realized by Montgolfier brothers with a balloon in 1783 [2]. It has been followed by the first zeppelin flight with Zeppelin LZ-I in 1900 [3]. At the same time period, Wright brothers had been struggling with their experimentations in flight and have accomplished on December 17, 1903 [4]. Orville Wright has aviated the first power-driven aircraft and covered a distance of 120 feet from 20 feet height. It is remarkable to note that the distance flown in the first flight was smaller than the wingspan of Boeing 747, however it is the fountain head of all state of the art aircrafts today.

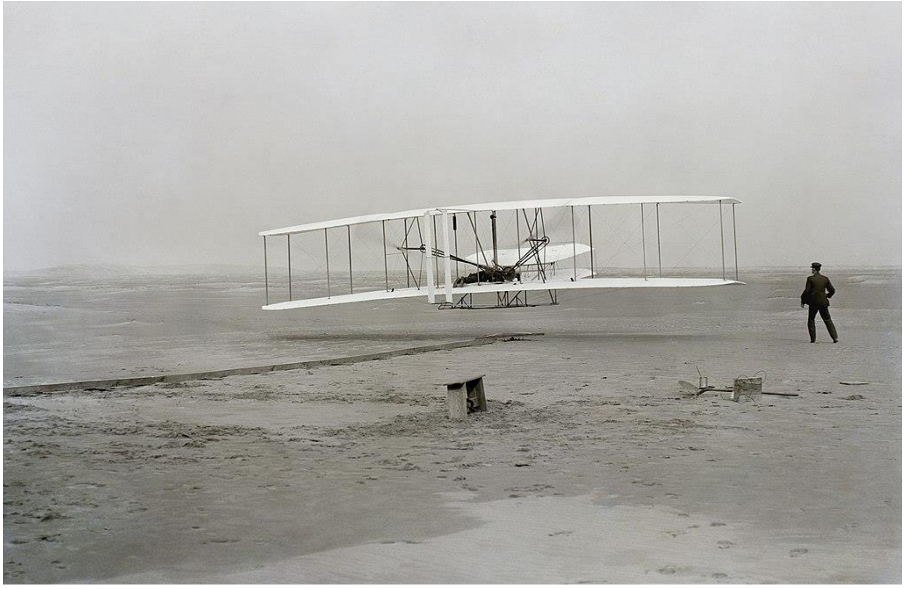

Figure 1-2 The First Flight of Wright Brothers [4]

From the inspiring studies of Leonardo to the modern aircrafts utilized today, engineers, scientists and pilots have confronted many troubles in designing, experimenting or flying the aircrafts. It is surely beyond doubt that one of the most difficult among them is to comprehend the aeroelastic effects and take them into considerations in the designing phase of the aircraft.

This chapter is devoted to give general introductory information to the science of aeroelasticity and the definitions of most known aeroelastic phenomenon, overview of striking aeroelastic events in the history and to discuss some inspiring studies leading the development process of the present thesis. The aim and the structure of the work are then presented.

Aeroelasticity is a discipline examining the interaction between the elastic deformation of a structure in an airflow and the subsequent aerodynamic forces [5]. The interdisciplinary nature of the study of aeroelasticity is summarized most clearly by the Collar's aeroelastic triangle as indicated in Figure 1-3 [5]. The diagram manifests how major disciplines of flight mechanics, structural dynamics and static aeroelasticity interact each other. If all three forces are taken into consideration, then the dynamic aeroelastic effects occur.

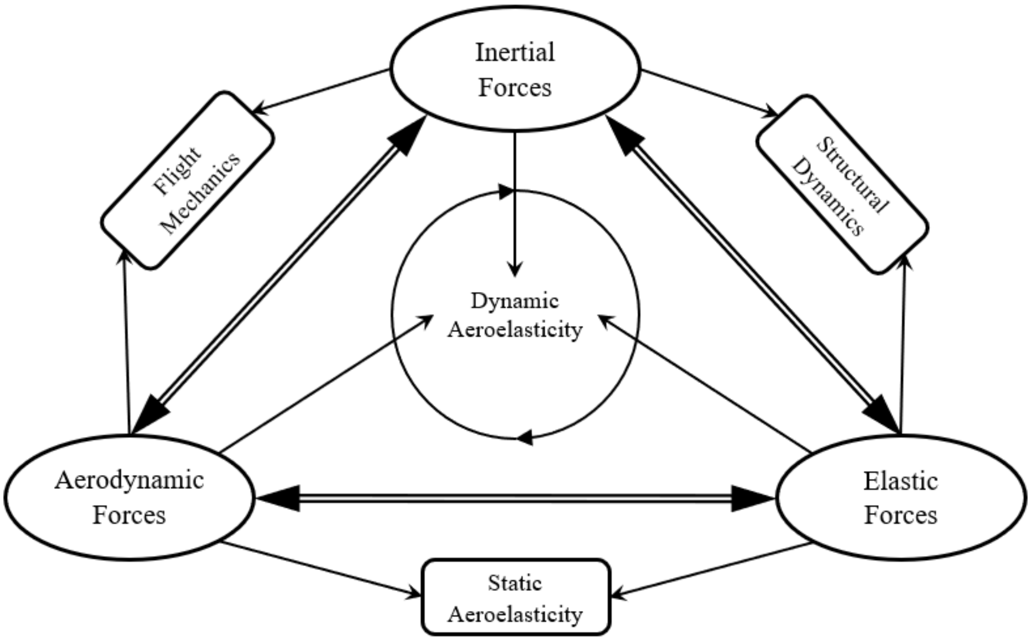

Figure 1-3 Collar's Aeroelastic Triangle[5]

The discipline of aeroelasticity basically is divided into two main branches as it is shown in Collar's diagram; static aeroelasticity and dynamic aeroelasticity. Those two also cover many aeroelastic phenomenon. For instance, static aeroelasticity, whose effects are experienced due to the interaction of aerodynamic and elastic forces, investigates the divergence and load distribution that are both originated from undesirable structural deformation of lifting surfaces in steady-state flight conditions. Dynamic aeroelastic problems, on the other hand, are the subjects undergoing intense study at the present time. Especially flutter and limit cycle oscillation (LCO) are the most-known and challenging ones with which aeroelasticity experts struggle in the industry. Further aeroelastic phenomenon are summarized in Figure 1-4.

All aeroelastic occurrences depend on the additive effects between aerodynamic forces and structural response. If a lifting surface is in an airstream, it is structurally deformed due to the aerodynamic forces naturally. Then these deformations may induce the aerodynamic force distribution acting on the structure and implicitly those additional effects may lead to further deformations till to entail the structural failure.

Namely, it can be concluded that if the aircraft structures are sufficiently rigid, aeroelastic problems would not exist.

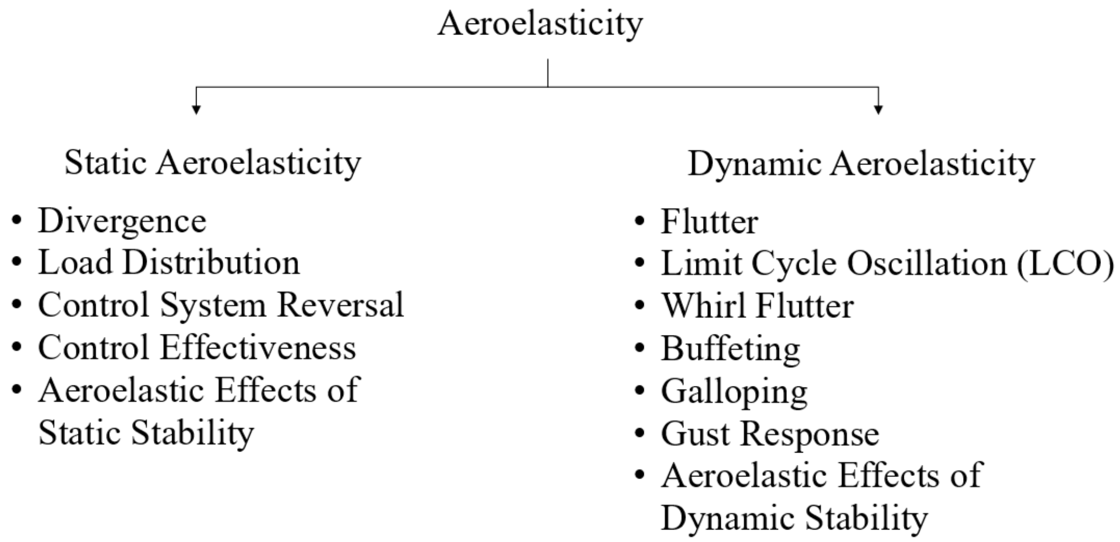
Aeroelasticity
Static Aeroelasticity
• Divergence
• Load Distribution
• Control System Reversal
• Control Effectiveness
• Aeroelastic Effects of Static Stability
Dynamic Aeroelasticity
• Flutter
• Limit Cycle Oscillation (LCO)
• Whirl Flutter
• Buffeting
• Galloping
• Gust Response
• Aeroelastic Effects of Dynamic Stability

Figure 1-4 Aeroelastic Phenomenon

1.2. History of Aeroelasticity

This sub-chapter is devoted to the historic context of the aeroelasticity, important milestones in the field and inspirational studies forming a basis of today's holistic perspective.

Starting from the early days of the manned flight, aeroelastic effects observed during the flights had been hard to overcome and sometimes unable to even apprehend. Engineers or pilots had realized only some anomalies that show up in defiance of their analytical calculations. They have perhaps associated the unexpected problems with structural weakness of the aircraft, but they have not been aware of the main reason.

In their historic flights, Wright brothers have succeeded in capitalizing on aeroelastic impacts on roll control of their aircraft by utilizing of wing warping system in lieu of ailerons. They have also noticed the adverse aeroelastic effects on the propeller blades' performance due to the twist after experimenting their wider and thinner propellers [6], [7] .

On December 8, 1903, Professor Samuel P. Langley has failed while trying to launch his powered tandem monoplane from the Potomac River. In both trails, the tandem monoplane has fallen into the river after structural failures occurred during launch. Although the reason of failure has been predicated on a mechanical problem in the catapult and aerodrome could not be released as it was planned, the second one had not been understood. It has been later assumed that the aeroelastic affects may come into play and G.T.R. Hill has raised that the failure was originated from the insufficient wing-tip stiffness ending up with wing torsional divergence [6], [8].

The first flutter case has been investigated by a British engineer and scientist F. W. Lanchester during the World War I over the anti-symmetric oscillation problem of the fuselage and tail experienced on Handley Page O/400 biplane (Figure 1-5). He has analyzed the problem and ended up with a text of only three pages stating two important concepts

1. The oscillations observed were not derived from the vibratory sources but were self-excited.
2. Increasing the torsional stiffness of the elevators could solve the oscillation problem [6], [9]

After a while later, a similar tail flutter case has occurred on Havilland DH-9 biplane and the solution is the same with the one suggested by Lanchester [6].

After Lanchester’s first conceptual assessment of the flutter problem, Leonard Baristow, who was professor of Aerodynamics at Imperial College, has provided analytical background of the problem of Handley Page biplane. The paper written by Baristow and Fage is currently counted as first theoretically flutter analysis [6], [10].

Figure 1-5 Handley Page O/400 Bomber Biplane [11]

In World War I, the only aeroelastic phenomena encountered in the operations was not only the flutter. Two German fighter aircrafts, the Albatros D-III and the Fokker D-VIII (Figure 1-6), has experienced fatal structural failures because of the static aeroelastic divergence problem. Albatros D-III fighter was a biplane with a lower wing that has a narrow single spar and is connected to upper part with V-strut not contributing to the global torsional stiffness of the whole wing. All of these caused that the wing was inclined to twist and in high-speed diving maneuvers eventuated in wing deformation divergence [6].

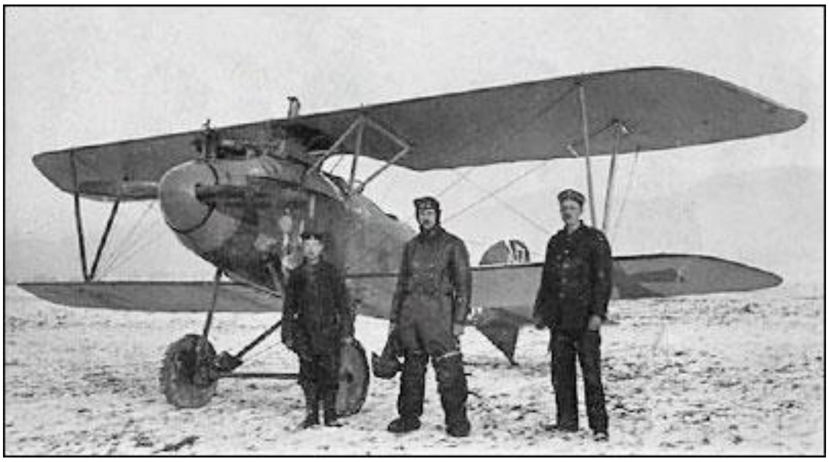

Figure 1-6 Albatros D-III Biplane Fighter [12]

Approaching the end of the war gradually, Fokker has released the Fokker D-VIII (Figure 1-7), which was a cantilever personal monoplane. They have rushed into production phase of it due to its superior performance. However, after it was used in service, serious problems were confronted regarding wing failures especially in high-speed dives. To apprehend the problem, the German Army has conducted the static tests on dozens of prototype wings and observed that they were over-designed to support the desired ultimate loads with a factor of six. However, there was a small difference between the prototypes and in-service aircrafts which were strengthened in rear spar region over the request by the Army. This modification naturally shifted the elastic axis behind and triggered the aeroelastic divergence of the wing [6].

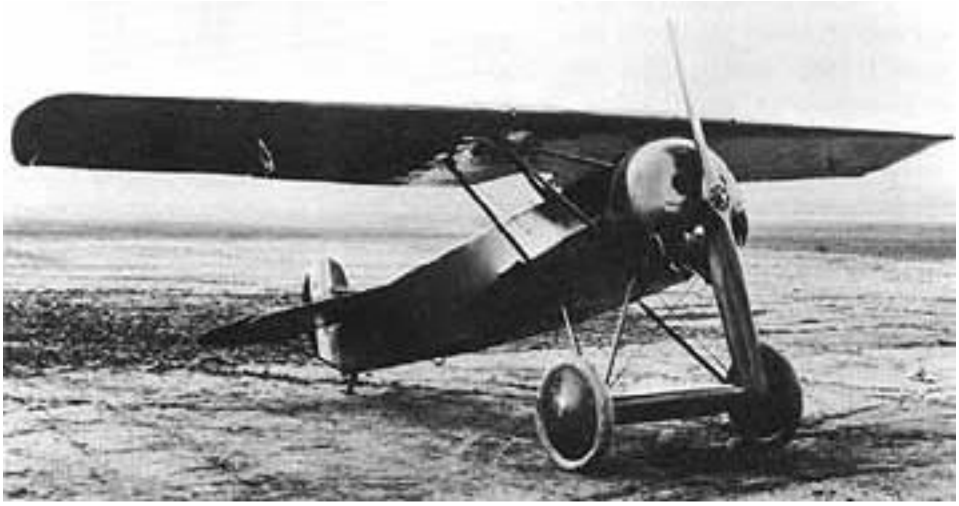

Figure 1-7 Fokker D-VIII Monoplane Fighter [13]

After World War I, a systematic study has been performed for the van Berkel W.B. monoplane whose aileron was experienced severe flutter. A. G. von Baumhauer and C. Koning have undertaken several experimental and theoretical investigations in 1923 and discovered that decoupling the interacting structural modes of the wing and aileron by means of mass balance of the control surface could remediate the problem [6], [14].

During this period, in the field of unsteady aerodynamics, preliminary but essential studies had been being carried out at full tilt. In 1923 and 1925, as a result of a thesis work assigned by Professor Prandtl, W: Birnbaum has published two important papers respectively laying a foundation of the solution techniques for the aerodynamic part of the aeroelastic problems [6], [15].

As time passes by the relevance to aeroelastic studies had been considerably increased. In the United States one study regarding flutter was that of the horizontal tail oscillations experienced on the Navy MO-1 airplane. After eliminating the main wing wake effect, that is an effective exterior excitation on the tail, Zahm and Bear have conducted an analysis for flutter and realized that the problem have arisen from the two-spar system whose bending and torsional structural modes interacts each other and results in flutter [6], [16].

In 1927, Manfred Rauscher initiated some flutter studies at the Massachusetts Institute of Technology (MIT) by through the disposability of the wind tunnel models for the purpose of flutter testing. These preliminary works have ended up with the foundation of MIT Aeroelastic and Structures Research Laboratory under the leadership of Rauscher at the outset of World War II [6], [17].

In 1932, many accidents have occurred with the fatalities and severe damage by the de Havilland Puss Moth airplane. ARC Accidents Investigation Subcommittee have then published a comprehensive report summarizing more than 50 separate investigations and concluded that not only main wing flutter but also control surface flutter like rudder and elevator may be included in those accidents, V-strut bracing method may trigger the wing flutter and some starting impulsive effects like turbulent flow may result in control surface flutter [6], [18].

Cox and Pugsley and Duncan and MacMillan have discovered new aeroelastic control problem, which is aileron reversal wherein as the flight speed increases the undesirable deflection of the aileron produces wing twist in ways that the effectiveness of the aileron diminishes and after a certain point it acts in opposite direction. It is crucial to stress that this problem was not a stability problem but a flight control problem due to the aeroelastic effects [6], [19], [20].

In the U.S., Theodore Theodorsen has concentrated to the flutter problems in 1934 and in consequence of intensive work within a few months he has published NACA Rept. No. 496, which had a big role in constituting the methods of flutter analysis in aviation industry [21]. He has given a telegraphic theory of two-dimensional oscillating flat plate having translational and torsional degrees of freedom. He has separated the circulatory and non-circulatory parts of the velocity potential and relates them to Theodorsen's function of C(k) derived from Bessel functions and depending on so-called reduced frequency, k. This work was the cornerstone of the exact estimation of the flutter for lifting surfaces [6].

In 1938, Theodorsen and Garrick have released a memorandum report prescribing the impacts of some parameters such as center of mass, moments of inertia, mass ratio, bending to torsional mode frequency ratio etc. on the flutter characteristics of the wings depending on several experimental studies [6], [22].

In 1935, Küssner has correlated many flutter incidents and accidents to apply an empirical formula which is dependent on torsional reduced frequency value. It was only a ballpark estimate for the flutter onset speed for current type of aircrafts. Similar empirical approach had been performed by Roxbee Cox in 1933 but he has attributed his formula to bending and torsional stiffnesses of the wing unlike the torsional frequency [6].

In 1936, besides all theoretical and analytical studies von Schlippe has brought in something new in Germany and employed the resonance testing techniques in flight for the purpose of reducing the risks emerging from flutter. The method is basically to check a new or modified aircraft by diving its maximum speed and hope for the best. After the test is done, the assessment has made by plotting the resonant amplitudes against airspeed and frequency at specific flight speed as shown in Figure 1-8 [6], [23].

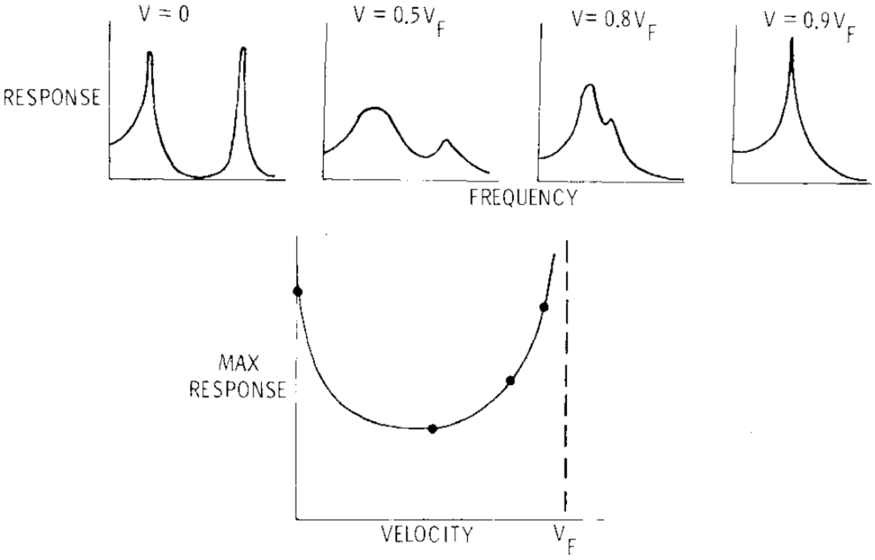

Figure 1-8 von Schlippe's Flight Flutter Test Techniques [6]

In prewar period (1938), a unique textbook by Frazer, Duncan and Collar has been published on matrices and their applications with the inclusion of several flutter examples. Their intentions were basically to emphasize the requirement of more degrees of freedom to be comprised in the flutter calculations to estimate better [24]. 3 years later, S. J. Loring has given a paper explaining a general utilization of matrix method specifically in flutter problems. However, this approach naturally has brought with the necessity of extensive computational capability for the big size of matrix calculations. These works underlie the current flutter estimation methods [6], [25].

In 1936, as a result of the increasing interest in designing the airplanes that are capable of flying near the sound speed, the investigations on compressible aerodynamics have accelerated. A significant paper by Prandtl in 1936 has been published on steady aerodynamics in a compressible medium being such as to set the stage for the equivalent studies in unsteady aerodynamics. He has introduced a nonconventional but useful method regarding the utilization of acceleration potential in lieu of velocity potential [6], [26].

During the World War II, rapid changes have taken place in aircraft designs as expected. The general intend was to develop aircrafts being able to fly higher speeds, cover long distance, carry payloads under the wing such as fuel tank, bombs etc. A tip-tank flutter problem, for instance, has occurred on the Lockheed P-80 fighter because of mass balance difference compared to the original configuration of the aircraft [6].

Smilg and Wasserman have given an advantageous table of several unsteady aerodynamic coefficients depending on the preeminent theory of Theodorsen in a document. These tables have served as an engineering handbook for flutter analysis for a few years. Their flutter estimation approach has also introduced a very important structural damping concept including the parameter g enabling to exhibit the flutter solution graphically by V-g flutter diagram [6], [27].

Alongside of all analytical solution methods, researchers and aircraft designers have placed emphasis on the reliable experimental data acquired from aeroelastic model tests in wind tunnels also supported by the mathematical analysis [6].

Hall has cited totally 53 published studies regarding aerodynamic derivative measurements in oscillating environment between the years of 1940-1956 in a survey released in 1962. It has summarized that those studies have been conducted by British and U.S. investigators mostly by the fact that measurements at low subsonic speeds have been acquired by Brits while transonic and supersonic flight regimes have awakened Americans' interest. However, since the earliest attempt to gather the air load data from the test specimen, it has been noticed that establishment of a reliable testing techniques was very crucial and hard to achieve [6], [28].

The problems in measuring the air loads on oscillating surfaces have been handled with an ingenious but simple electrical measurement technique offered by Bratt, Wight and Tilley. It is known as "wattmeter" harmonic analyzer which has expanded the accuracy of data gathering for attainment of oscillatory aerodynamic derivative [6], [29].

After internalizing the usefulness of the wind-tunnel flutter models to validate the mathematical analysis and then determine the margins of safety for small aircrafts, an additional requirement has arisen to develop a down scaled aeroelastically representative wind-tunnel model for relatively big full-metal constructed and high speed aircrafts. For this purpose polyvinyl-chloride has been utilized due to its advantages of representing the internal and external construction of the aircraft easily. Wasserman and Myktow has given their experiences in AGARD Aeroelasticity Manual in 1961 [30]. Moreover 1/4 -scaled complete replica of wing model of the PBM-1 seaplane has been tested in the NACA Propeller Research Tunnel by Nagel, Bergen, Miller and Hartman. However the popularity of utilizing plastic flutter models in the wind tunnel tests has abated due to the limitations in capability of processing, fluctuation in material properties with changing ambient temperature and humidity and high cost of fabrication [6].

In 1946, exclusively for flutter testing at high subsonic Mach numbers up to 0.8, a special 4 ft wind tunnel had been constructed at the Langley Laboratory. A remarkable feature of the wind-tunnel is the test medium, which could be either air or freon gas, enables the investigators to adjust the density and speed of sound of the flow. This tunnel has later been modified such that it had transonic testing capability and served as a vanguard facility in the field of aeroelasticity until today [6].

With the furtherance in aircraft designs being capable of flying at transonic regimes, new and challenging aeroelastic problems, some of which still burning issues today, have come to exist. One of them was the severe oscillation problems encountered on the aileron of new P-80 airplane during the high speed flights in 1944. This aeroelastic phenomenon has been later called as “aileron buzz” originated from the coupling of control surface rotation and chordwise motion of shock waves on the wing. In spite of the fact that mass balance method was thought as a remedy for the problem, wind-tunnel tests has manifested that it had no tangible effects. Eventually the solution has converged to increased control stiffness, dampers and airfoil shape changes [6], [31].

In 1945, the wing sweep has been introduced as a new design feature to achieve transonic speed efficiently by R. T. Jones. The wing sweep has been firstly used in Boeing B-47 bomber and corresponding aeroelastic tailoring has been performed. The utilization of this new design feature has led to open new areas of research from the point of all aeroelastic phenomenon such as divergence and flutter [6].

The lack of non-linear transonic flow theory and the nonexistence of the fully operable transonic wind-tunnels at those days have forced to aircraft designers to find some alternative experimental techniques to assure the effectivities of the new designs and they came up with four methods by the help of radar and telemetry technologies allowing for remote data collection in 1946

1. Free-falling of the body dropped from a high-flying aircraft
2. Ground launching of a specially designed rocket-propelled models
3. The placement of the model (or scaled model) on upper surface of an airplane wing in a region where transonic flow can be achievable
4. Rocket sled acceleration of the body to the transonic flight regime [6]

Due to the high costs in these extreme testing methods, the inevitable result was the foundation of the transonic wind tunnels by 1950s. At Langley aforementioned 4 ft Freon Tunnel has been firstly converted to a 2 ft transonic tunnel for the use of flutter researchers [6].

With the rapid advent of aircraft designs, flutter has been begun to be evaluated in supersonic speed experienced mostly during dive maneuver. Some analytical approaches to supersonic flutter assessment have been introduced by Temple and Jahn in England, by von Borbely in Germany and by Garrick and Rubinow in U.S [6], [32]–[34].

The NACA Subcommittee on Vibration and Flutter in 1956 has published a state-of-the-art survey in which there are numbers of the flutter incidences and their details for U.S. military aircrafts during the period of 1947-1956. Although the resulting table has been far from being complete and not included the commercial and civilian aircrafts data, it has proven the severity of the phenomenon. For instance, it was noted that the number of 21 experienced transonic control surface buzz, for which there was no reliable theory or design guidelines in those years [6], [35].

After the World War II, development of computing machines has accelerated in a way to be in two paths, analog and digital. The first analog device, which was the differential analyzer of Vannevar Bush could solve linear differential equations with variable coefficients. Digital computing devices, on the other hand, have shown up gradually toward the end of the 1940s. With the developments in the computing machines, of course, the equations whose solutions take too much time with hand calculations have become worth the effort and this implicitly helped the replacements of classical flutter methods with the advanced ones being capable of catching more accurate results [6].

With the increase on the number of the flutter incidences and the challenging problems encountered during the aircraft design regarding aeroelastic phenomenon, Federal Aviation Agency (FAA) has given importance on this issue and in order to standardize the precautions that must be taken for the purpose of preventing the designs from failure, added related requirements in Federal Aviation Regulations (FAR) when they released Part 23, 25, 27 and 29 in 1965 [36]. Hereby, the first civil certification requirement regarding aeroelasticity has been noticed. In 1971, in addition to the civil aviation requirements, the first military specification MIL-A-8870A (Notice-1) has been published regarding aeroelasticity [37].

Thanks to the enhancements in high performance computers, advanced wind tunnel testing and instrumentation techniques, aeroelastic assessments are currently performed more comprehensively and professionally compared to the past, surely depending on cumulative knowledge mentioned above. To get an approval for the first flight, all related efforts from analytical calculations to high risky flight test results are presented to certification authority for showing compliance with the requirements prescribed in the regulations and specifications.

1.3. Literature Survey

The work described in this thesis was performed for the purpose of simulating the flutter certification procedure of a modified aircraft with a simple wing-like structure by conducting linear frequency domain flutter analyses, ground vibration tests, modal updating activity and wind tunnel flutter tests to correlate the results. This sub-chapter presents an overview of the studies regarding aforementioned efforts, encountered problems and resulting solutions preceded the work prescribed in the thesis

A. F. Zahm and R. M. Bear have performed a study of wing flutter and published gotten results in a technical report in a way to be three parts. The first prescribes vibration experiments conducted in wind-tunnel for simple airfoils and tail wing of MO-1 aircraft. Flow around the tail model is investigated also in this part. The second part arises a stability criterion for wing vibrations observed in pitch and roll axes and gives principal design rules to preclude instability. In the third part, a guideline is offered for designing spars such that they flex equally under aero-loading to prevent the wing from undesirable twist in pitch [16].

In 1940, T. Theodorsen and I. E. Garrick have given the basic flutter theory in a simpler and more comprehensive form compared to previous ones, depending on a number of tests carried out on cantilever wings for validating the proposed theory and observing its suitability to real three-dimensional problems [22].

By the early of 1950s, J. G. Barmby, H. J. Cunningham and I. E. Garrick have investigated the flutter of sweptback cantilever wings which were just arisen as a new design concept and published a technical report in which resulting outputs are presented in 1951. They have compared their analytical approach for swept wings with the experiments and concluded that it can reasonably give main effects of sweep on flutter characteristics [38].

In 1953, his preeminent study, William J. Bursnall has presented the comparison of the results acquired separately from wing flutter testing conducted in Langley transonic blowdown wind-tunnel and free-fall flight flutter tests. In the tunnel, he has utilized scaled wing model whose full-size version had already fluttered in the flight test. With highly correlated results between flight testing and wind-tunnel analysis, it was apprehended that using wind-tunnels to certify the new designs is more feasible in lieu of high-costly flight tests [39].

In 1954, Raymond Herrera and Robert H. Barnes have published their work regarding several flutter experiments with quadrilateral wings having several aspect ratios at different Mach numbers from 0.6 to 1.1. The materials of the test specimens were solid aluminum or steel and 2, 4 and 6 percent thick. The most prominent inference from the test results was the dependency of the flutter triggering structural modes to the given angle of attack. That is, while the first bending mode is dominant at low angles of attack, the torsional mode of the structure starts to be involved in as angle of attack rises [40].

In 1954, W. G. Molyneux has committed a paper to summarize the results of an extensive experimental study performed to observe the effects of the sweep angle, taper ratio and position of the elastic axis on flutter onset speed. He has also compared the test results with two different analytical approaches for acquiring the flutter speed. The resulting table has provided very helpful information towards to the wing designs which are desired to be free from flutter [41].

In a similar experimental study, W. J. Tuovila and John Locke McCarty have examined effects of high Mach numbers, different sweepback angles and center of gravity locations on flutter results by using cantilever wing models in 1955. The results have manifested that as center of gravity goes back in the direction of chord with the increasing sweep angle, stiffening the wing becomes essential to prevent the wing from flutter [42].

In addition to experimental flutter assessments, the requirement of undertaking the design problems with a correlated analytical approach has forced Carson Yates to develop a method based on Rayleigh type analysis for estimating the flutter characteristic of wings having finite span, being swept or unswept in subsonic and supersonic aerodynamic regimes. He has achieved a good correlation between hand-calculated and experimental results [43].

With the development of highly maneuverable fighter jets being capable of carrying external payloads underneath wing, the flutter evaluation of several different configurations has become a crucial requirement. S. J. Pollock, W. A. Sotomayer, L. J. Huttsell and D. E. Cooley have investigated the evaluation methods for wing/store flutter estimation and active flutter suspension thanks to the sponsorship of Flight Dynamics Laboratory. They have utilized both analytical and experimental calculations to observe the influence of store aerodynamics on the flutter characteristics [44].

In order to enhance existing and emerging unsteady aerodynamic codes and methods dedicated for especially aeroelastic problems, E. Carson Yates has published the AGARD Report No: 765 in which the results of experimental studies are given for NACA 445.6 wing. In the report, all details of the NACA 445.6 wing model such as geometrical dimensions, equivalent structural properties and test boundary conditions are prescribed. Additionally, all test results are attached as they are in the Appendix section of the report. Due to the inclusion of all valuable data, this report has become a useful reference document that is used by the scientists trying to develop their own aeroelastic codes [45].

Alongside of experimental enhancements in aeroelasticity, analytical calculation has gained importance due to the high costs and difficulties in arrangement of wind tunnels for different types of wing geometries. P. C. Chen has contributed to this accumulation of knowledge and presented the g-method depending on damping perturbation in the general flutter equation. In actuality, the g-method is a generalized form of K-method and P-K method for the sake of more reliable damping prediction. The g-method is still utilized in an aeroelastic solver ZAERO© offered by ZONA Technology Inc [46].

Raja Samikkannu and A. R. Upadhya have studied on aeroelastic characteristics of a T-tail structure of a transport aircraft. They have firstly fabricated a scaled model of the T-tail in a way to have same structural properties with the real stabilizer utilizing composite structures. Wind-tunnel test then has been conducted to see the flutter characteristics of the model [47].

In 2012, Wang Libo, Shen Long, Chen Lei, Wu Zhigang and Yang Chao has published a paper to explain their comprehensive study including essentially design of a wind tunnel test model for flutter analysis of a semispan aircraft. They have performed ground vibration test (GVT), modal updating and flutter analyses based on P-K flutter solution method. At the end, they have correlated their results with the wind tunnel tests [48].

In the scope of his thesis study, M. Burak Dalmış has investigated flutter behavior of a plate in low subsonic aerodynamic regime by conducting frequency domain flutter analyses in ZAERO$^{©}$. Then, he validated his results by carrying out wind tunnel flutter tests in Ankara Wind Tunnel. He has also examined the effects of payload integrated on the wing tip on flutter onset speed with a scaled wing model similar to F-16 wing [49].

1.4. Aeroelastic Certification

After aeroelastic phenomenon had been examined in detail; underlying reasons and their effects on aircraft designs have been well-apprehended, convenient and robust solutions to the encountered problems have been started to be applied and ultimately a requirement has shown up to standardize the aircraft design effort in a specific way based on accumulated experiences. In a new aircraft design, depending on whether it is for military or civil purposes, there are some certain rules, i.e. regulations that the design holders have to fulfill regarding aeroelastic stability. These requirements are given in different specifications. The following ones are the most-known specifications / regulations extensively utilized in aerospace industry.

1.4.1. Military Specifications

1. MIL-HDBK-516C, Subchapter 5.2 Structural Dynamics
    a. 5.2.1. Aeroelastic Design – General

    b. 5.2.2. Aeroelastic Design – Aeroservoelasticity
    c. 5.2.3. Aeroelastic Design – Control Surfaces and Other Components
    d. 5.2.4. Aeroelastic Design – Fail Safe
2. MIL-A-8870C Airplane Strength and Rigidity, Vibration, Flutter and Divergence
3. Royal Air Force Defense Standards, DEF-STAN 00-970 Part 1 Section, Design and Airworthiness Requirements for Service Aircraft, Design and Construction, Subpart 4.8 Aero-elasticity, Flutter and Vibration
    a. Leaflet 23 Aero-elasticity, Flutter Clearance Program
    b. Leaflet 24 Aero-elasticity, Main Surface Flutter
    c. Leaflet 25 Aero-elasticity, Flutter of Control Surfaces (Ailerons, Elevators, Rudders)
    d. Leaflet 26 Aero-elasticity, Spring and Servo Tab Flutter
    e. Leaflet 27 Aero-elasticity, Model Testing in Wind Tunnels
    f. Leaflet 28 Aero-elasticity, Stiffness Tests
    g. Leaflet 29 Aero-elasticity, Hydraulic Actuator Impedance
    h. Leaflet 30 Aero-elasticity, Still Air Resonance Tests
    i. Leaflet 31 Aero-elasticity, Flight Flutter Tests
    j. Leaflet 32 Flutter and Vibration, Flight Vibration Survey
4. MIL-HDBK-1763 Chapter 4 General Requirements Subchapter 4.1.4.4 Aeroelastic Analyses
5. STANAG 4671, UAV Systems Airworthiness Requirements, USAR 629 Flutter

1.4.2. Civil Regulations

1. CFR 14 Part 23 Sec. 23.629 Flutter
2. CFR 14 Part 25 Sec. 25.629 Flutter, Deformation and Fail-Safe Criteria
3. CFR 14 Part 27 Sec. 27.629 Flutter
4. CFR 14 Part 29 Sec. 29. 629 Flutter and Divergence

All these specifications and regulations both describe the requirement and show how to satisfy it. While some of them explain the methods and means of compliance internally, some address additional documents such as advisory circulars prescribing the points to take into account and the expectations of the certification authority for the approval of the design.

While designing a new aircraft or modifying an existing one that has been already certified, the design holder has to show compliance to the project related certification authority regarding the aircraft's aeroelastic stability. Independently of in question regulation, the general aeroelastic certification flows for newly designed and modified aircraft are given in Figure 1-9 and Figure 1-10 respectively. For both, the major steps are same. Since the dynamic characteristics of the aircraft is quite important to be able to determine the aeroelastic behavior of the aircraft, these properties have to be extracted by Ground Vibration Test (GVT). In this way, the global structural mode frequencies and mode shapes can be calculated together with the corresponding damping ratios. These data are then utilized for updating the initial Finite Element Model (FEM) of the aircraft. After aeroelastic calculations are performed with updated FE model, all results are correlated with the flight tests and entire set of compliance documents are presented to the admittance of the authority.

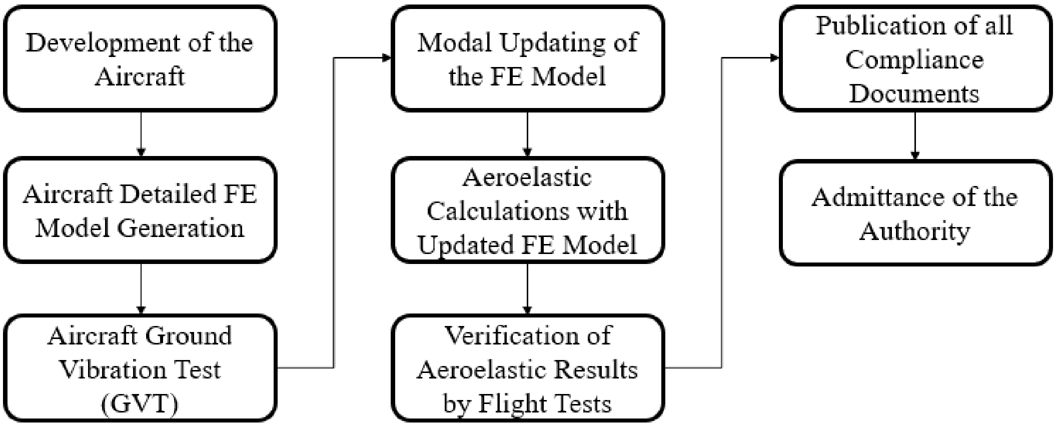
Development of the Aircraft
Aircraft Detailed FE Model Generation
Aircraft Ground Vibration Test (GVT)
Modal Updating of the FE Model
Aeroelastic Calculations with Updated FE Model
Verification of Aeroelastic Results by Flight Tests
Publication of all Compliance Documents
Admittance of the Authority

Figure 1-9 General Aeroelastic Certification Flow for Newly Designed Aircrafts

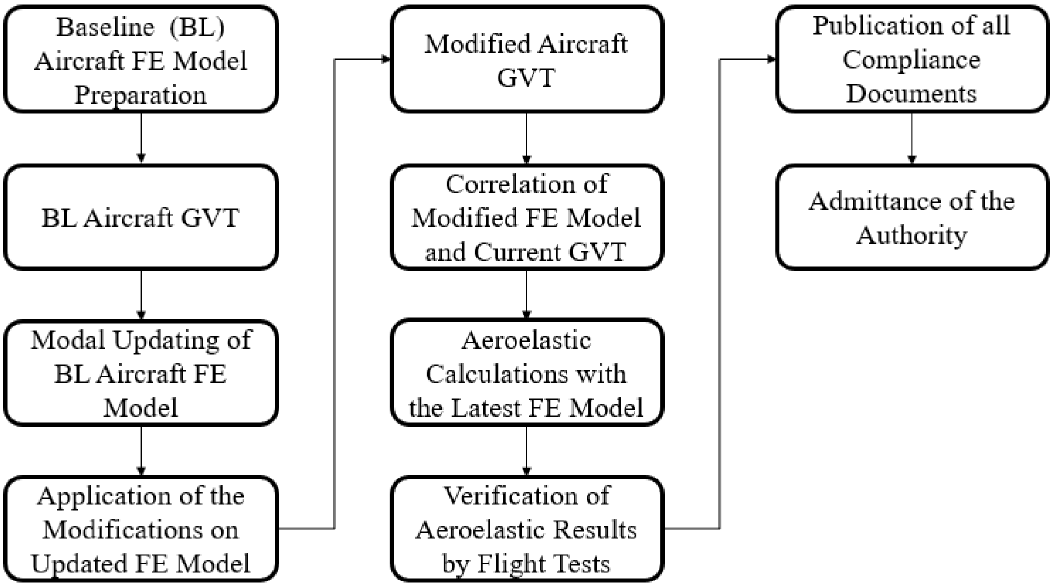
Baseline (BL) Aircraft FE Model Preparation
BL Aircraft GVT
Modal Updating of BL Aircraft FE Model
Application of the Modifications on Updated FE Model
Modified Aircraft GVT
Correlation of Modified FE Model and Current GVT
Aeroelastic Calculations with the Latest FE Model
Verification of Aeroelastic Results by Flight Tests
Publication of all Compliance Documents
Admittance of the Authority

Figure 1-10 General Aeroelastic Certification Flow for Modified Aircrafts

Flight test is a critical phase in an aircraft certification process to verify the aeroelastic results [50]–[52]. Such testing activities are conducted to determine a flight envelope in which the aircraft has acceptable properties. Civil or military certification authorities give consequence to the flight data being capable of clearly demonstrating a flight envelope that is free from any adverse aeroelastic effects such as flutter.

In aeroelastic certification process, wind tunnel tests have an important role especially when aerodynamic and structural behavior of new configurations are doubtful. To support the certification work and update the numerical models used in simulations, dynamically scaled models, which are equivalent with the full-scale aircraft in aerodynamic and structural manner, are fabricated. However, such testing is not adequate to substitute for flight tests which is always obligatory for flutter certification [51].

1.5. Aim and Structure of the Thesis

The aim of this thesis is twofold:

1. To determine the grade of accuracy of frequency domain flutter simulation results of wing-like structure together with the effects of the payloads in incompressible flow by comparing them with wind tunnel flutter test results
2. To simulate the aeroelastic certification process with a simple wing-like structure, observe the possible problems and find effective solutions to enhance the methodology used for real aeroelastic certification projects

In this study, a wing-like structure is designed such that it can experience flutter at low subsonic speed by adjusting the taper ratio, location of the elastic axis and the sweep angle [41]. To investigate the effects of payloads on flutter characteristics, three of them are added in different stations under the wing-like structure. Flutter analyses of all configurations are realized in ZAERO$^{©}$, which is a commercial aeroelastic solver supplied by ZONA Technology Inc. The modal information such as natural frequencies and corresponding mode shapes necessitated by ZAERO$^{©}$ are acquired from MSC Nastran$^{©}$. All structural finite element models are created in Altair HyperMesh$^{©}$. The ground vibration test (GVT) of the wing-like structure, on the other hand, is performed with Simcenter Scadas$^{©}$ data acquisition system and test natural frequencies and mode shapes are extracted utilizing the Polymax algorithm embedded in Simcenter Testlab$^{©}$. The modal updating of the FE model depending on the GVT results is conducted in FEMtools$^{©}$. Finally, the wind tunnel flutter tests are done in Ankara Wind Tunnel (ART) test facility. In these tests strain data are gathered from the root of the wing-like structure by using Dewesoft R4$^{©}$ data acquisition system and the data are examined with HBM nCode Glyphworks$^{©}$.

It is important to stress that the study includes all the steps required for aeroelastic certification process summarized in Figure 1-9 apart from only the flight flutter tests as shown in Figure 1-11. In lieu of it, there are wind tunnel flutter tests to correlate numerical analysis results. Although any laboratory test, even aerodynamically and structurally equivalent test article is established, does not substitute the flight flutter test, since there is not a real aircraft being obliged to be certified in this study, the wind tunnel tests are realized for the correlation purpose. If it is a real aircraft design or modification project comprising aeroelastic certification requirements, the authority surely demands to see flight flutter test results for the admittance of the design.

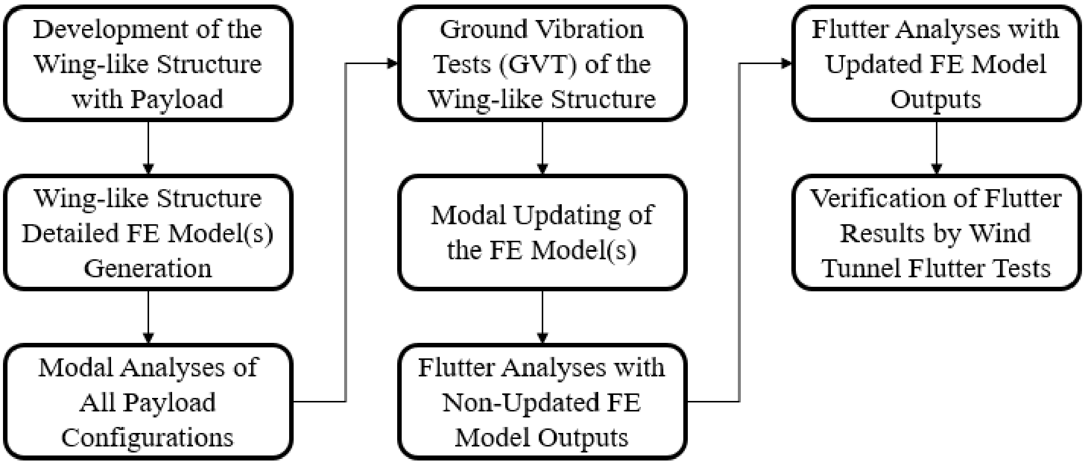
Development of the Wing-like Structure with Payload
Wing-like Structure Detailed FE Model(s) Generation
Modal Analyses of All Payload Configurations
Ground Vibration Tests (GVT) of the Wing-like Structure
Modal Updating of the FE Model(s)
Flutter Analyses with Non-Updated FE Model Outputs
Flutter Analyses with Updated FE Model Outputs
Verification of Flutter Results by Wind Tunnel Flutter Tests

Figure 1-11 The Work Flow in Present Thesis

This introductory chapter is followed by Chapter 2, in which the basics of linear potential flow theory, steady and unsteady aerodynamics are given to facilitate the understanding of aeroelastic background of ZAERO©. Starting from the definition of velocity vector, the essentials of the steady flow theory and the unsteady aerodynamic which is the fundamental of aeroelastic numerical analysis are detailed. In the last part of this chapter, the eigenvalue problem constructed in ZAERO© is outlined with the discussion of the flutter solution techniques and their differences by putting forward the g-Method.

The details of specially designed wing-like structure are then presented in Chapter 3. General dimensions of the design, the sequence of assembly of the sub-components, materials to be used and their properties and definitions of the configurations are summarized in this section.

In Chapter 4, the studies for dynamic model generation are summarized. It includes three major sections. The section of 4.2 gives the finite element modal analysis results of all configurations. The finite element modelling philosophy together with the element types and sizes and boundary conditions are presented. Then numerical mode frequencies and shapes are shared. The section 4.3 includes the results of ground vibration tests for all configurations. The GVT setup, the instrumentation of transducers and the method of excitation of the structure are detailed. At the end, test resonant frequencies, their modal damping values and test mode shapes are given. In compatible with the aeroelastic certification, modal updating study is introduced in section 4.4 with a distinct focus on the influence of boundary conditions on the dynamic characteristic of the structure. The results of modal updating study belonging to the configuration(s) that needs to be updated per the correlation of the finite element modal analysis and the ground vibration test results are given in this part.

Chapter 5 is devoted to the flutter substantiation studies of the wing-like structure. The section of 5.2 gives the results of all frequency domain flutter analysis. The preparation of the aerodynamic panel model in ZAERO$^{©}$ is outlined with the explanation of the chosen aerodynamic parameters for the analyses in this sub-chapter. Then the graphical flutter results which are acquired by updated and non-updated modal information, are introduced. The wind tunnel flutter test details are given in section 5.3 with the explanations of the test set-up and the instrumentation details of the strain gage used for the flutter onset speed monitoring. The test flutter results are incorporated in this section for different store configurations.

Chapter 6 outlines comparisons and inferences of the flutter analysis and test results. The influences of different store configurations on flutter results are then discussed. Inferences of unexpected flutter speed trend between the configurations are introduced with some further numerical analysis and test results.

Finally, Chapter 7 gives the conclusions of the present study and recommendations for the future works.

CHAPTER 2

THEORY

2.1. General Introduction

In this study, aeroelastic stability characteristic of a simple wing-like structure is investigated via the ZAERO©, which is a commercial software that provides required modules to solve for the structural and aerodynamic parts of the aeroelasticity problem simultaneously. The ZAERO© has the capability of solving aeroelastic problems in four different aerodynamic regimes, i.e., subsonic, transonic, supersonic and hypersonic. Utilizing user defined aerodynamic panel model, ZAERO© computes Aerodynamic Influence Coefficient (AIC) matrix at any Mach number by solving the integral equation of the unsteady linearized potential equation with the assumption of the simple harmonic motion which is based on a fundamental unsteady aerodynamic parameter called reduced frequency, k. Then, it combines the AIC matrix with externally provided modal information (i.e. eigenvalues and eigenvectors) by an appropriate spline methodology and realize the flutter analysis by both the g-method and k-method.

This chapter is devoted to give the basics of linear potential flow theory, steady and unsteady aerodynamics. Underlying aeroelastic theory of ZAERO© is then presented.

The sub-sections of 2.2, 2.3 and 2.4 are referenced from the comprehensive textbook of Fundamentals of Modern Unsteady Aerodynamic by Prof. Dr. Ülgen GÜLÇAT, Istanbul Technical University. The reader can refer to it for further details [53].

2.2. Potential Flow

The velocity vector in cartesian coordinates can be defined as follows:

$$\vec{q} = u\vec{\imath} + v\vec{\jmath} + w\vec{k}$$

where u, v and w denotes the velocity components in x, y and z directions, respectively and $\vec{\imath}$, $\vec{\jmath}$ and $\vec{k}$ are the corresponding unit vectors. The continuity, momentum, energy and state equations in a vector notation are given below for an inviscid flow, respectively:

$$\frac{D\rho}{Dt} + \rho\nabla \cdot \vec{q} = 0 \tag{2.1}$$

$$\frac{D\vec{q}}{Dt} + \frac{1}{\rho}\nabla\mathrm{p} = 0 \tag{2.2}$$

$$\frac{D}{Dt}\left(\frac{a^2}{\gamma - 1} + \frac{q^2}{2}\right) - \frac{1}{\rho}\frac{\partial p}{\partial t} = 0 \tag{2.3}$$

$$p = \rho RT \tag{2.4}$$

Here the density is denoted by ρ, time by t, the pressure by p, the speed of sound by a, the specific heat ratio by γ, the gas constant by R and lastly the temperature by T.

It is crucial to stress that the air is assumed to be a perfect gas and besides the gravitational and surface to surface interaction forces (i.e. body forces and frictional forces, respectively) are neglected.

Under the aforementioned assumptions the Kelvin's theorem states

$$\Gamma = \oint q \cdot ds \tag{2.5}$$

$$\frac{D\Gamma}{Dt} = -\oint \frac{dp}{\rho}. \tag{2.6}$$

For a flow definition in which the fluid density does not change or the pressure is only dependent on density, that is barotropic fluid, the right-hand side of the Kelvin's theorem goes to zero.

$$\frac{D\Gamma}{Dt} = 0 \tag{2.7}$$

This means that the circulation does not change under these conditions with respect to time. For a flow with a constant free-stream, the circulation is equal to zero and accordingly the velocity vector $\vec{q}$ can be acquired from the gradient of an arbitrary scalar potential ϕ as follows:

$$\vec{q} = \nabla\phi. \tag{2.8}$$

Then the momentum equation can be modified based on the assumptions of constant free stream and barotropic flow

$$\nabla \cdot \left(\frac{\partial\phi}{\partial t} + \frac{q^2}{2} + \int \frac{dp}{\rho} \right) = 0. \tag{2.9}$$

In general, the scalar terms under gradient operator are only dependent on time

$$\frac{\partial\phi}{\partial t} + \frac{q^2}{2} + \int \frac{dp}{\rho} = F(t) \tag{2.10}$$

Here $F(t)$ is an arbitrarily chosen, time-dependent function. If it is assumed to be zero, the classical Kelvin's equation is obtained

$$\frac{\partial\phi}{\partial t} + \frac{q^2}{2} + \int \frac{dp}{\rho} = 0 \tag{2.11}$$

Utilizing the classical Kelvin's theorem, the continuity equation in terms of velocity potential and the definition of the speed of sound, the equation below is acquired ultimately

$$\nabla^2\phi - \frac{1}{a^2}\left(\frac{\partial^2\phi}{\partial t^2} + \frac{\partial q^2}{\partial t} + \vec{q} \cdot \nabla \frac{q^2}{2} \right) = 0. \tag{2.12}$$

This equation is a scalar non-linear equation in which the velocity vector is expressed in terms of the velocity potential with only one unknown, speed of sound. Thanks to this equation, a wide range of aerodynamic problems can be modelled with the application of appropriate boundary conditions.

In order to specify proper boundary conditions, the starting point is to give the equation of a surface for a 3-D moving body in a flow field according to a cartesian coordinate system such that x-axis is the flow direction and z-axis is the normal to the flow

$$B(x,y,z,t) = z - z_a(x,y,t) = 0. \tag{2.13}$$

Here a single valued surface equation is denoted by z_a and it is based on time and position on the xy-plane. The material derivative of above equation in the flow field $\vec{q}$ yields vertical velocity component w which is so-called downwash velocity in aerodynamics.

$$w = \frac{\partial z_a}{\partial t} + u\frac{\partial z_a}{\partial x} + v\frac{\partial z_a}{\partial y} \tag{2.14}$$

Eq. (2.14) is a non-linear boundary condition which is imposed to Eq. (2.12) to be able to model certain problems. However, these two are non-linear equations which can only be solved by linearizing them.

Let us start with the linearization of the boundary conditions utilizing the small perturbation method. Consider steady and irrotational flow around a thin airfoil as shown in Figure 2-1

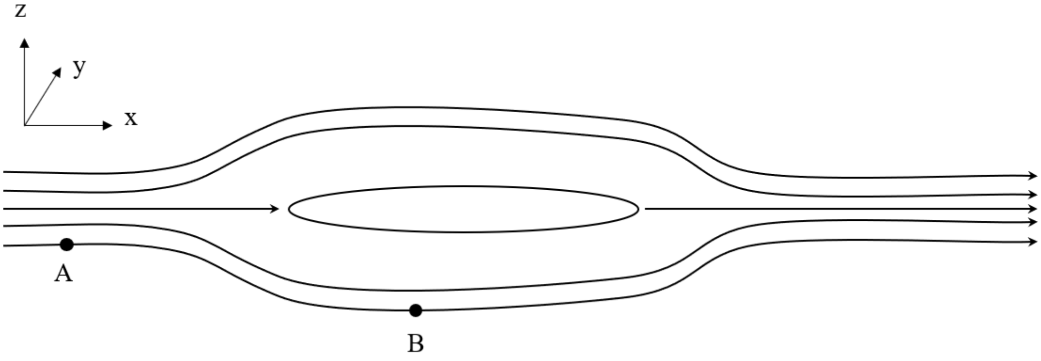

Figure 2-1 Flow Around a Thin Airfoil

At position A, the velocity of the free stream is only in the x-direction. However, relatively approaching body disturbs the velocity components of the free stream at position B. Let us define the velocity vector at far field (i.e. position A) as $\vec{q} = U\vec{\imath}$.

Let u', v' and w' are the perturbation velocity components in cartesian coordinate system at position B and their relations with the perturbation potential function ϕ' are as follows

$$\phi = \phi' + Ux \qquad \frac{\partial \phi'}{\partial x} = u' \qquad \frac{\partial \phi'}{\partial y} = v' \qquad \frac{\partial \phi'}{\partial z} = w'$$

Small perturbation method is essentially based upon the assumption that free stream speed is quite bigger than the perturbation speed components such that u', v', $w' \ll U$. Furthermore, under the assumption of thin airfoil as illustrated in Figure 2-1, slopes of the single valued surface equation z_a are quite small

$$\frac{\partial z_a}{\partial x} \ll 1 \qquad \frac{\partial z_a}{\partial y} \ll 1$$

Then the non-linear boundary condition in Eq. (2.14) becomes

$$w = \frac{\partial z_a}{\partial t} + U\frac{\partial z_a}{\partial x} + u'\frac{\partial z_a}{\partial x} + v'\frac{\partial z_a}{\partial y} \quad \text{where} \quad u'\frac{\partial z_a}{\partial x}, v'\frac{\partial z_a}{\partial y} \ll U\frac{\partial z_a}{\partial x}$$

Then approximate expression of linearized boundary condition is as follows

$$w = \frac{\partial z_a}{\partial t} + U\frac{\partial z_a}{\partial x} \tag{2.15}$$

For upper and lower surfaces linearized downwash velocity expressions can be written as shown below

$$\begin{aligned} &\text{Upper Surface } (u) \quad : \quad w = \frac{\partial z_u}{\partial t} + U\frac{\partial z_u}{\partial x}; z = 0^+ \\ &\text{Lower Surface } (l) \quad : \quad w = \frac{\partial z_l}{\partial t} + U\frac{\partial z_l}{\partial x}; z = 0^- \end{aligned} \tag{2.16}$$

To obtain an expression for linearized pressure coefficient, Eq. (2.10) can be utilized. Term by term linearization process is summarized as shown below:

1st Term: $\frac{\partial \phi}{\partial t} = \frac{\partial \phi'}{\partial t} \; since \; \phi = \phi' + Ux$

2nd Term: $\frac{q^2}{2} = \frac{(U+u')^2 + v'^2 + w'^2}{2} = \frac{U^2}{2} + Uu'$

3rd Term: $\int_{p_\infty}^{p} \frac{dp}{\rho} = \frac{p - p_\infty}{\rho_\infty}$ $where\ p\ is\ any\ value\ of\ pressure$

4th Term: $F(t) = \frac{U^2}{2} \longrightarrow arbitrarily\ chosen$

Then Eq. (2.10) becomes

$$\frac{p - p_\infty}{\rho_\infty} = -\left(\frac{\partial \phi'}{\partial t} + U\frac{\partial \phi'}{\partial x}\right). \tag{2.17}$$

Then utilizing the definition of pressure coefficient C_p, linearized version of it can be extracted as follows:

$$C_p = \frac{2}{-U^2}\left(\frac{\partial \phi'}{\partial t} + U\frac{\partial \phi'}{\partial x}\right). \tag{2.18}$$

Now Eq. (2.12) can be linearized again by using small perturbation approach. Focusing the non-linear terms in the parenthesis

$$\begin{aligned} \frac{\partial q^2}{\partial t} &\cong 2U\frac{\partial u'}{\partial t} \\ &= 2U\frac{\partial^2 \phi'}{\partial t \partial x} \qquad where\ \vec{q} = U\vec{\imath} + \nabla\phi' \\ &\qquad\qquad\qquad\quad = U\vec{\imath} + u'\vec{\imath} + v'\vec{\jmath} \\ \vec{q}\cdot\nabla\frac{q^2}{2} &\cong U^2\frac{\partial u'}{\partial x} \qquad\qquad + w'\vec{k} \\ &= U^2\frac{\partial^2 \phi'}{\partial x^2} \end{aligned} \tag{2.19}$$

By knowing that $\frac{\partial^2 \phi}{\partial t^2} = \frac{\partial^2 \phi'}{\partial t^2}$ and by use of Eq. (2.19), Eq. (2.12) becomes

$$\nabla^2\phi - \frac{1}{a^2}\left(\frac{\partial^2 \phi'}{\partial t^2} + 2U\frac{\partial^2 \phi'}{\partial t \partial x} + U^2\frac{\partial^2 \phi'}{\partial x^2}\right) = 0$$

Ultimately the closed form of the equation

$$\nabla^2\phi - \frac{1}{a^2}\left(\frac{\partial}{\partial t} + U\frac{\partial}{\partial x}\right)^2 \phi' = 0 \tag{2.20}$$

Eq. (2.20) is not totally linearized version of Eq. (2.12) due to presence of the square of the speed of sound that is the only remaining non-linear term in the equation. Let us define the local speed of sound with respect to free stream speed of sound and perturbation speed of sound as

$$a = a_\infty + a'.$$

Utilizing the energy equation, i.e. Eq. (2.3), it can be concluded that the perturbation speed of sound is quite smaller than the free stream speed of sound and the approximate value of the local speed of sound is said to be equal to the free stream speed of sound. Therefore, the linearized potential flow equation is finally acquired as

$$\nabla^2\phi - \frac{1}{a_\infty^2}\left(\frac{\partial}{\partial t} + U\frac{\partial}{\partial x}\right)^2 \phi' = 0. \qquad (2.21)$$

2.3. Steady Flow

The primitive mathematical modelling approach for the external flow is essentially based upon the thin airfoil theory at small angle of attack. The main assumption in order to model external flow is that the profile starts to move impulsively from the rest and has a constant speed of U on the instant. This results in a velocity field $\vec{V} = \vec{V}(x, z)$ on the airfoil parallel to the surface. In the boundary layer, the magnitude of the velocity goes to zero on airfoil surface due to the no slip condition as shown in Figure 2-2.

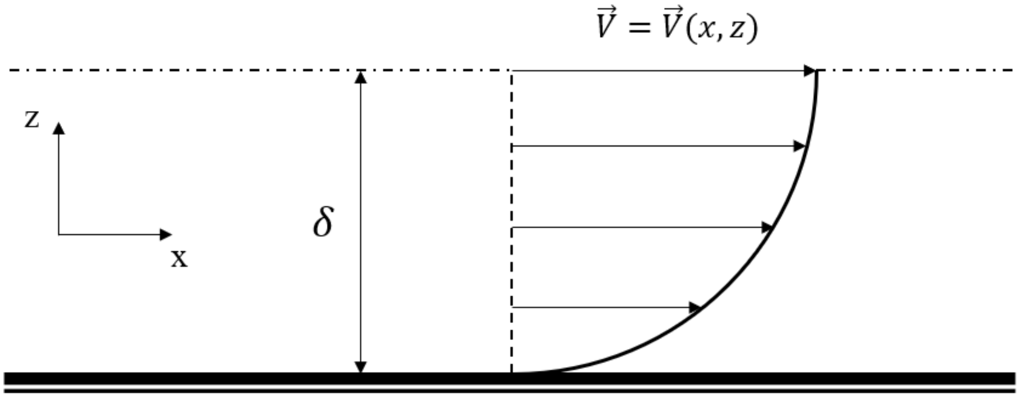

Figure 2-2 Velocity Profile in Boundary Layer

Outside of the boundary layer the flow stays potential and this region can be modelled utilizing the potential flow theory. Inside the boundary layer, however, viscous effects produce circulation that helps the generation of lift and this region can be modelled as a vortex sheet.

If an infinitesimal circulation $d\Gamma$ is calculated in the boundary layer whose thickness is δ over a rectangular boundary as shown in Figure 2-3

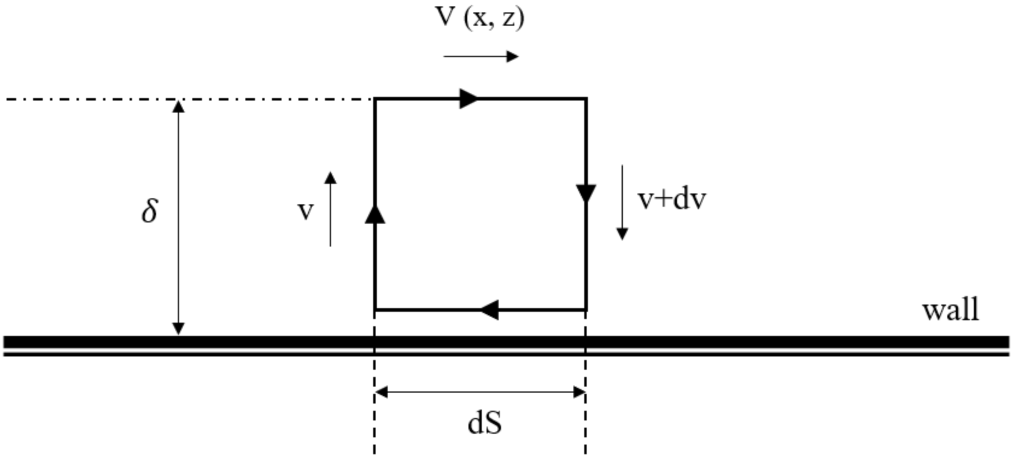

Figure 2-3 Infinitesimal Circulation in Boundary Layer

The infinitesimal circulation in clockwise direction can be calculated as $d\Gamma = 0.dS + v.\delta + V(x,z).dS - (v + dv).\delta = V(x,z).dS - dv.\delta$. If second order term of $dv.\delta$

is neglected, infinitesimal circulation becomes $d\Gamma = V(x,z).dS$. Then the strength of the vortex sheet in the boundary layer is $\gamma = d\Gamma/dS = V(x,z)$.

According to Kelvin's theorem presented in Section 2.2, the total circulation stays constant over the course of the motion. Because the impulsive motion prescribed above starts from the rest, the total circulation initially is zero and remains zero accordingly.

$$\Gamma = \oint \gamma.dS = 0$$

The closed integral above is to be evaluated around the airfoil on a closed loop which can be chosen as airfoil surface for convenience. To be able to comprehend the rationale of modelling the boundary layer region as vortex sheets let us focus on what occurs on the airfoil surface when it moves impulsively from rest at time $t = 0^+$ and $t > 0$. Figure 2-4 and Figure 2-5 shows surface and wake vortex sheets and total circulations at $t = 0^+$ and $t > 0$ respectively. As seen in Figure 2-5 there are two different circulations, which are both evaluated on clockwise direction. Γ_a denotes the bound circulation that is zero at the beginning and reaches a constant value on the airfoil soon after the impulsive motion starts. According to the Kelvin's theorem at any instant during the motion the total circulation should be zero which makes the wake circulation value $-\Gamma_a$.

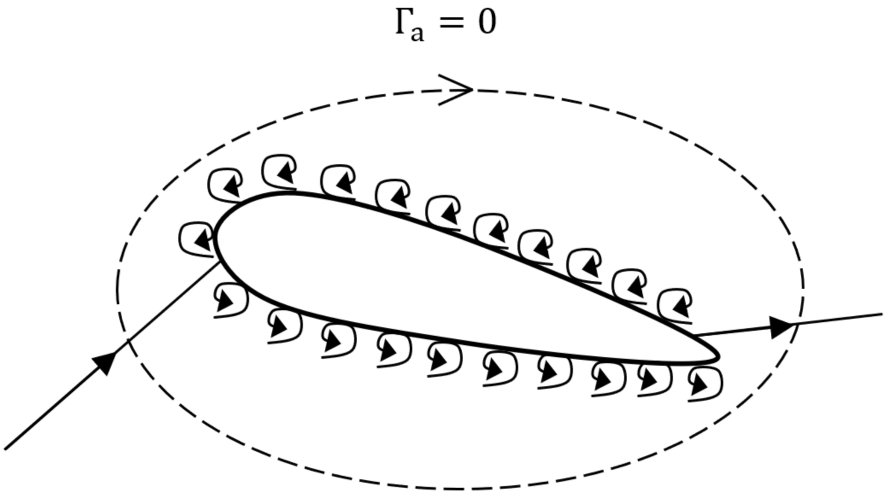

Figure 2-4 Surface Vortex Sheet at $t = 0^+$

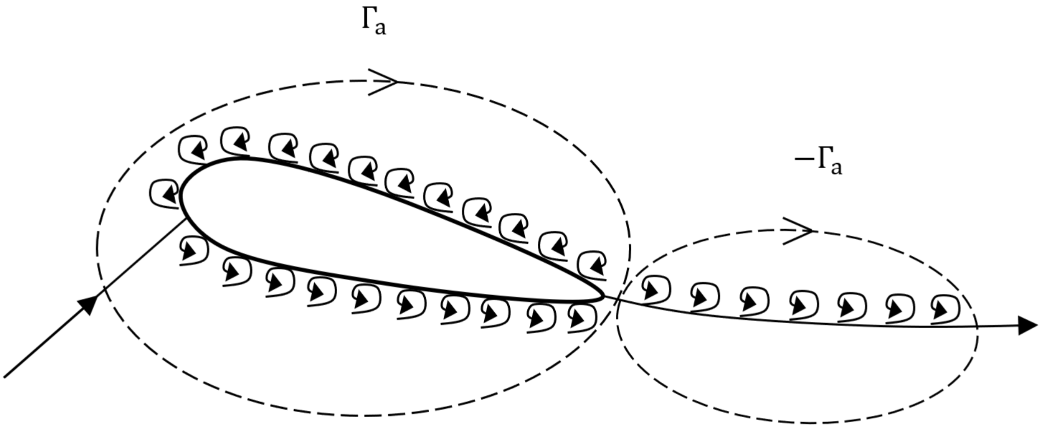

Figure 2-5 Surface and Wake Vortex Sheet at $t > 0$

As time goes on and the flow turn out to be stable on the airfoil, the strengths of the vortex sheet on upper and lower surfaces at the trailing edge become equal in magnitude but opposite in sign. This results in the velocity at the sharp trailing edges being zero and this condition is known as the Kutta condition. The Kutta condition is responsible for the generation of positive circulation, hence the lifting force. It was experimentally proven that 90% of the total lift is created within 3 chord lengths of travel of the airfoil after the impulsive motion starts.

When the Kutta condition is satisfied at the trailing edge, the flow reaches steady state. In steady flow, as it is mentioned before, there are two sources of circulation; the first one is the bound vortex and second one is the wake (starting) vortex. Since the wake vortex is distant from the airfoil, its effect can be neglected. In contrary, the vortex sheets of upper and lower surfaces are the effective ones which have to be taken into consideration in the mathematical calculation of lifting force.

If the thickness of the airfoil is smaller than 0.12c where c denotes the chord length of the profile, it can be assumed that the upper and lower surface vortices are close enough to merge them into one vortex sheet by adding their strengths for the sake of simplicity.

$$\gamma_a(x) = \gamma_u(x) + \gamma_l(x)$$

Under this assumption, Figure 2-6 displays the vortex sheet modeling about an airfoil whose chord length is 2b in magnitude and the chordline coincides with the x-axis.

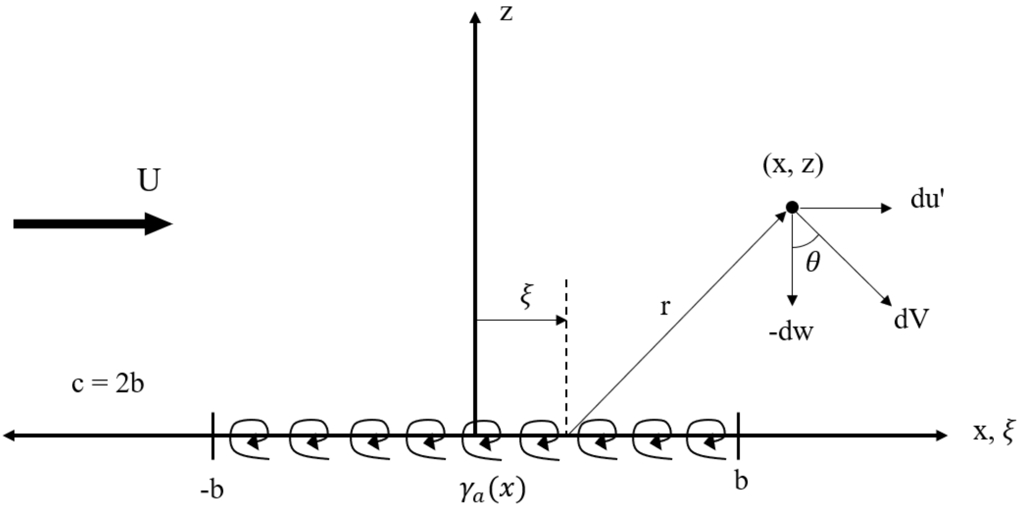

Figure 2-6 Vortex Sheet Modeling about an Airfoil

In definition the magnitude of rotational velocity vector that is tangent to the closed contour on which the line integral is evaluated to find the circulation can be found as follows:

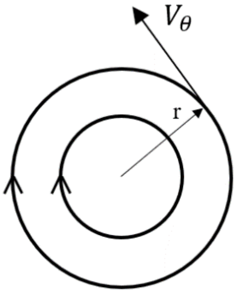

$$\Gamma = \oint \vec{V} \cdot \overrightarrow{dS} = V_\theta \oint dS = V_\theta 2\pi r$$

$$\Rightarrow V_\theta = \frac{\Gamma}{2\pi r}$$

Based on the definition of the circulation prescribed above and according to the Biot-Savart law, the differential velocity at a random point on xz-plane is expressed below:

$$dV = \frac{d\Gamma}{2\pi r} = \frac{\gamma_a(\xi)d\xi}{2\pi r}$$

Then the horizontal and vertical components of differential velocity can be acquired as

$$du' = dVsin\theta = \frac{z\gamma_a(\xi)d\xi}{2\pi r^2} \qquad dw = -dVcos\theta = \frac{(x-\xi)\gamma_a(\xi)d\xi}{2\pi r^2}$$

In order to find u' and w as functions of x and z, let us take the integral of above expressions along the chord of the profile

$$u'(x,z) = \frac{1}{2\pi}\int_{-b}^{b}\frac{z\gamma_a(\xi)d\xi}{(x-\xi)^2+z^2} \qquad w(x,z) = -\frac{1}{2\pi}\int_{-b}^{b}\frac{(x-\xi)\gamma_a(\xi)d\xi}{(x-\xi)^2+z^2}$$

Thanks to the above integrands, it is clear that the function of u' is anti-symmetric and function of w is symmetric. That is

$$u'(x,0^+) = -u'(x,0^-) \qquad w(x,0^+) = w(x,0^-)$$

This information helps us to relate the strength of the vortex sheet to the perturbation speed u' with the circulation calculation in an infinitesimal rectangle shown in Figure 2-7

$$\begin{aligned}\gamma_a(x)dx &= [U+u'(x,0^+)]dx-(w+dw)dz-[U+u'(x,0^-)]dx+wdz\\ &= u'(x,0^+)dx-u'(x,0^-)dx-dwdz\end{aligned}$$

Neglecting the second order term

$$\gamma_a(x) = u'(x, 0^+) - u'(x, 0^-) = 2u'(x, 0^+) \tag{2.22}$$

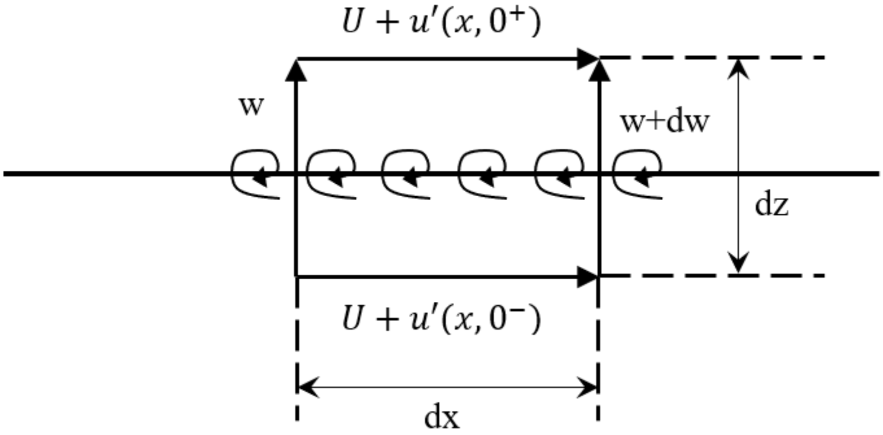

Figure 2-7 Circulation Calculation

Now we can find the downwash at the surface, $z = 0$

$$w(x, 0) = -\frac{1}{2\pi} \int_{-b}^{b} \frac{\gamma_a(\xi) d\xi}{(x - \xi)} \tag{2.23}$$

The integral in Eq. (2.23) can be evaluated by Cauchy's Integral Theorem. If it is considered that $\gamma_a(x)$ is the unknown function and $w(x, 0)$ is known, utilizing Eq. (2.15) with the steady-state assumption

$$w(x, 0) = U \frac{dz_a}{dx} = -\frac{1}{2\pi} \int_{-b}^{b} \frac{\gamma_a(\xi) d\xi}{(x - \xi)}$$

In order to invert above equation for the unknown function $\gamma_a(x)$ it is better to use non-dimensional coordinates as follows

$$x^* = \frac{x}{b} \qquad \xi^* = \frac{\xi}{b} \qquad \Rightarrow \qquad \begin{aligned} w(x^*, 0) &= U \frac{dz_a(x^*)}{dx^*} \\ &= -\frac{1}{2\pi} \int_{-1}^{1} \frac{\gamma_a(\xi^*) d\xi^*}{(x^* - \xi^*)} \end{aligned}$$

Then the inverted form of Eq. (2.23) is obtained as below

$$\gamma_a(x^*) = \frac{2}{\pi}\sqrt{\frac{1-x^*}{1+x^*}}\int_{-1}^{1}\sqrt{\frac{1+\xi^*}{1-\xi^*}}\frac{w(\xi^*)}{x^*-\xi^*}d\xi^* \tag{2.24}$$

Eq. (2.24) satisfies the Kutta condition at the trailing edge since the vortex sheet is equal to zero at $x = b \Rightarrow x^* = 1$. Now, the bound vortex sheet strength can be correlated with the lifting pressure coefficient. To do this, use of the Bernoulli equation written between upper and lower surfaces of the profile and the definition of pressure coefficient is a good starting point.

$$p_u + \frac{1}{2}\rho(U + u'_u)^2 = p_l + \frac{1}{2}\rho(U + u'_l)^2$$

where subscripts u and l represent upper and lower surfaces, respectively. Let us remind the relation between perturbation speeds of lower and upper surfaces and Eq. (2.22)

$$u'_u = -u'_l \qquad\qquad \gamma_a(x) = 2u'(x, 0^+) = 2u'_u$$

Then the Bernoulli equation becomes

$$p_u + \frac{1}{2}\rho\left(U^2 + 2Uu'_u + {u'_u}^2\right) = p_l + \frac{1}{2}\rho\left(U^2 - 2Uu'_u + {u'_u}^2\right)$$

$$\frac{p_u - p_l}{\frac{1}{2}\rho} = -4Uu'_u \qquad \Rightarrow \qquad \frac{p_u - p_l}{\frac{1}{2}\rho U^2} = c_{p_a} = -\frac{4u'_u}{U}$$

The pressure coefficient with respect to the strength of the vortex sheet is finally obtained as

$$c_{p_a}(x) = -\frac{2\gamma_a(x)}{U} \tag{2.25}$$

Now utilizing Eq. (2.25) sectional lifting force l can be found as follows

$$l = \int_{-b}^{b} -(p_u - p_l)dx = \int_{-b}^{b} -\left[c_{p_a}(x)\frac{1}{2}\rho U^2\right]dx = \int_{-b}^{b} \rho U \gamma_a(x)dx$$

$$= \rho U \int_{-b}^{b} \gamma_a(x)dx = \rho U \Gamma_a$$

$$l = \rho U \Gamma \tag{2.26}$$

where Γ is the total circulation on the airfoil and Eq. (2.26) is the Kutta-Joukowski theorem .

Furthermore, we can calculate sectional lift by using Eq. (2.24) with non-dimensional parameters

$$l = \rho U \int_{-b}^{b} \gamma_a(x)dx = \rho U b \int_{-1}^{1} \gamma_a(x^*)dx^*$$

$$= \rho U b \int_{-1}^{1} \left[\frac{2}{\pi}\sqrt{\frac{1 - x^*}{1 + x^*}} \int_{-1}^{1} \sqrt{\frac{1 + \xi^*}{1 - \xi^*}} \frac{w(\xi^*)}{x^* - \xi^*} d\xi^*\right] dx^*$$

We can take the terms that are not dependent on x^* out of the integrals and sectional lift becomes

$$l = \frac{2\rho U b}{\pi} \int_{-1}^{1} \left[\sqrt{\frac{1 + \xi^*}{1 - \xi^*}} w(\xi^*) \left(\int_{-1}^{1} \sqrt{\frac{1 - x^*}{1 + x^*}} \frac{1}{x^* - \xi^*} dx^*\right)\right] d\xi^*$$

The integral in the inner parentheses is $-\pi$. Then the final form of the sectional lift becomes

$$l = -\rho U 2b \int_{-1}^{1} \sqrt{\frac{1 + \xi^*}{1 - \xi^*}} w(\xi^*)\, d\xi^* \tag{2.27}$$

By utilizing Eq. (2.27) the sectional lift can be calculated for an airfoil with an angle of attack, α as shown in Figure 2-8.

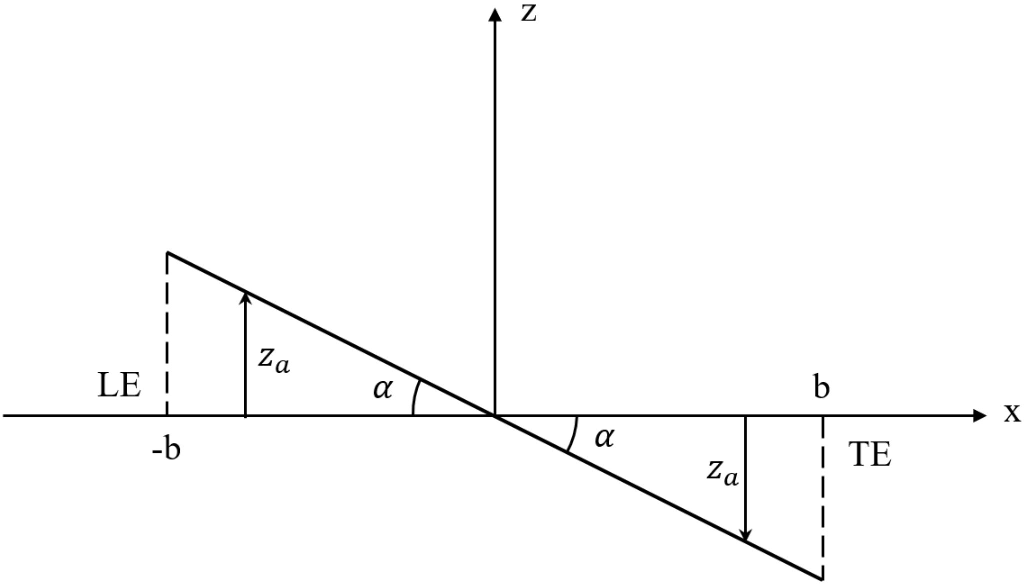

Figure 2-8 An Airfoil with Angle of Attack $\boldsymbol{\alpha}$

If we utilize Eq. (2.15) then the downwash velocity becomes for steady flow conditions:

$$w = U\frac{\partial z_a}{\partial x} = U\frac{\partial(-\alpha x)}{\partial x} = -U\alpha$$

If we insert downwash w into Eq. (2.27), then the sectional lift can be obtained as follows:

$$l = \rho U^2 2b\alpha \int_{-1}^{1} \sqrt{\frac{1+\xi^*}{1-\xi^*}}\, d\xi^* = 2\pi\alpha\rho U^2 b$$

$$l = \left(\frac{1}{2}\rho U^2\right)(2b)(2\pi\alpha) \qquad (2.28)$$

In Eq. (2.28), the expression in the first parenthesis is the dynamic pressure, the second one is the chord and the last one is the lift coefficient.

2.4. Unsteady Flow

Up to this point, basics of fixed wing aerodynamics have been investigated by using the potential flow theory and in accordance with the nature of steady flow, the aerodynamic forces and moments are assumed to be constant over time. However, for flutter estimation it is required that the effects of the dynamic motion of the aerodynamic surfaces (thin airfoil in 2D solution) are included to obtain accurate aerodynamic forces and moments.

The modelling of a thin airfoil oscillating in a uniform and incompressible flow has been at the heart of the all flutter predictions for many years [54]. The first and complete solution of the problem was proposed in 1935 by Theodorsen whose theory is dependent on the potential flow theory and the Kutta condition [21]. He has separated the solution into two: Eq. (2.15) is fulfilled with the source-sink combination (doublet) just above and below the profile as shown in Figure 2-9; bound vortex and wake vortex sheets are then added on the profile and wake region respectively, as shown in Figure 2-10. The first approach is adopted for calculating the non-circulatory components of unsteady lift and moment in plunge and pitch degrees of freedom while the second is for the circulatory ones.

Consider a thin airfoil of chord c = 2b, with elastic axis positioned at a distance “ab” from the mid-chord on which there are one torsional spring and one linear spring in a way to give pitching and plunging degrees of freedom to the dynamic system as indicated in Figure 2-11. The parameter “a” is non-dimensional coefficient such that -1 ≤ a ≤ 1 and it is based upon the elastic manner of the airfoil. The profile undergoes oscillatory harmonic motion in plunging direction such that $h = h_0 e^{i\omega t}$ (positive downwards) and in pitching direction such that $\theta = \theta_0 e^{i\omega t}$ (positive clockwise). Then the non-circulatory and circulatory terms of the unsteady lift and moment acting on the thin airfoil about the elastic axis per unit span may be written as [21], [54]

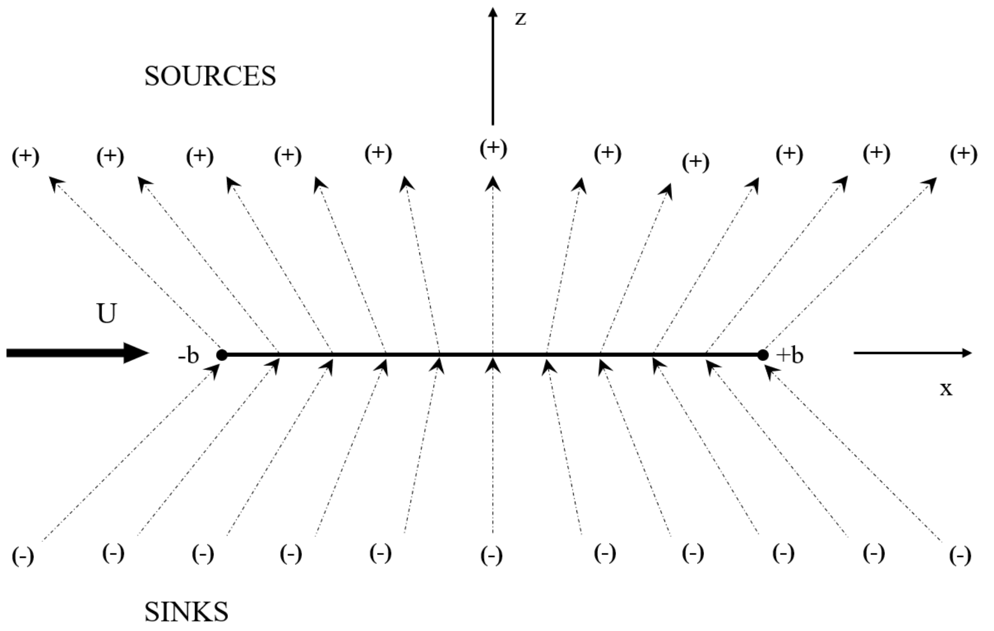
z
SOURCES
(+)
U
-b
+b
x
(-)
SINKS

Figure 2-9 Sources and Sinks on the Thin Airfoil

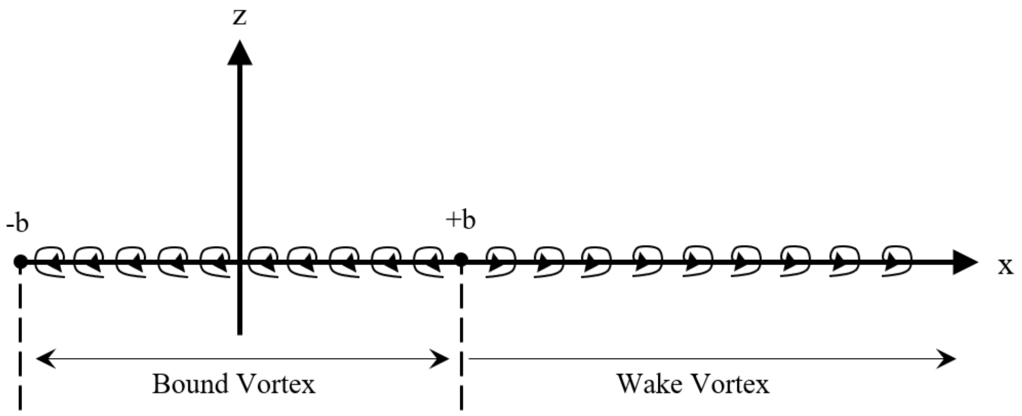
z
-b
+b
x
Bound Vortex
Wake Vortex

Figure 2-10 Bound and Wake Vortices

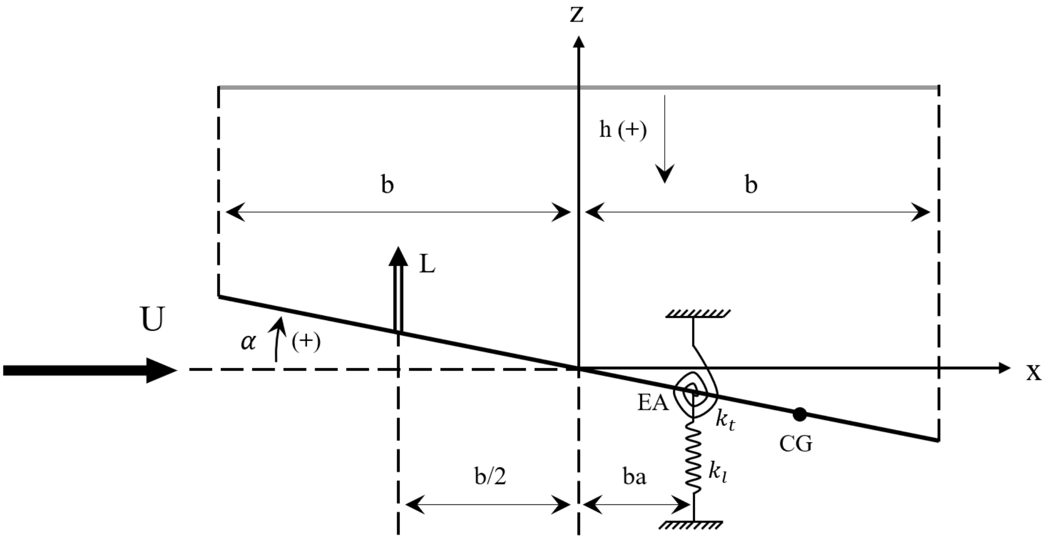

Figure 2-11 Thin Aerofoil undergoing Plunging and Pitching Motion

$$L_{NC} = \pi\rho b^2\left(\ddot{h} + U\dot{\alpha} - ba\ddot{\alpha}\right)$$

$$M_{NC} = \pi\rho b^2\left[U\dot{h} + ba\ddot{h} + U^2\alpha - b^2\left(\frac{1}{8} + a^2\right)\ddot{\alpha}\right]$$

$$L_C = 2\pi\rho U b C(k)\left[\dot{h} + U\alpha + b\left(\frac{1}{2} - a\right)\dot{\alpha}\right]$$

$$M_C = -\pi\rho b^2\left[Ub\left(\frac{1}{2} - a\right)\dot{\alpha} + U\dot{h} + U^2\alpha\right] + 2\pi\rho U b^2\left(a + \frac{1}{2}\right)C(k)\left[\dot{h} + U\alpha + b\left(\frac{1}{2} - a\right)\dot{\alpha}\right]$$

The total lift and moment can be found by adding the non-circulatory and circulatory components each other

$$L_T = \pi\rho b^2\left(\ddot{h} + U\dot{\alpha} - ba\ddot{\alpha}\right) + 2\pi\rho U b C(k)\left[\dot{h} + U\alpha + b\left(\frac{1}{2} - a\right)\dot{\alpha}\right] \tag{2.29}$$

$$M_T = \pi\rho b^2 \left[ba\ddot{h} - Ub\left(\frac{1}{2} - a\right)\dot{\alpha} - b^2\left(\frac{1}{8} + a^2\right)\ddot{\alpha}\right] + 2\pi\rho U b^2\left(a + \frac{1}{2}\right)C(k)\left[\dot{h} + U\alpha + b\left(\frac{1}{2} - a\right)\dot{\alpha}\right] \tag{2.30}$$

The $C(k)$ in Eq. (2.29) and (2.30) is the so-called Theodorsen function [21] that comprises of complex and real parts such that $C(k) = F(k) + iG(k)$ where the function parameter "k" is the reduced frequency defined as in Eq. (2.31)

$$k = \frac{\omega b}{U} \tag{2.31}$$

Here the harmonic oscillation frequency is denoted by ω, the half chord length by b and the free stream velocity by U. The reduced frequency is a measure of the unsteadiness of the incompressible flow. The main reason for acquiring the unsteady lift and moment depending on the specific reduced frequency and then performing the flutter solution in the frequency domain is that the establishment of the system of equations in the time domain is quite hard and the solution takes much more time. Therefore, the Theodorsen function is quite helpful to estimate the changes in amplitude and phase of the unsteady aerodynamic forces and moments for different frequency parameters in relatively short time.

The real and imaginary parts of the Theodorsen function are actually first and second kind of the Bessel functions as expanded in Eq.s (2.32) and (2.33)

$$F(k) = \frac{J_1(k)[J_1(k) + Y_0(k)] + Y_1(k)[Y_1(k) - J_0(k)]}{[J_1(k) + Y_0(k)]^2 + [Y_1(k) - J_0(k)]^2} \tag{2.32}$$

$$G(k) = -\frac{Y_1(k)Y_0(k) + J_1(k)J_0(k)}{[J_1(k) + Y_0(k)]^2 + [Y_1(k) - J_0(k)]^2} \tag{2.33}$$

J_0 and J_1: Bessel functions of 1st kind (order of 0 and 1)

Y_0 and Y_1: Bessel functions of 2nd kind (order of 0 and 1)

The complex plane representation of the Theodorsen function is given in Figure 2-12. Even though the calculation of Theodorsen function per Bessel functions of first and second kind is beyond the scope of this thesis, many commercial software solutions inherently include them and compute it very easily.

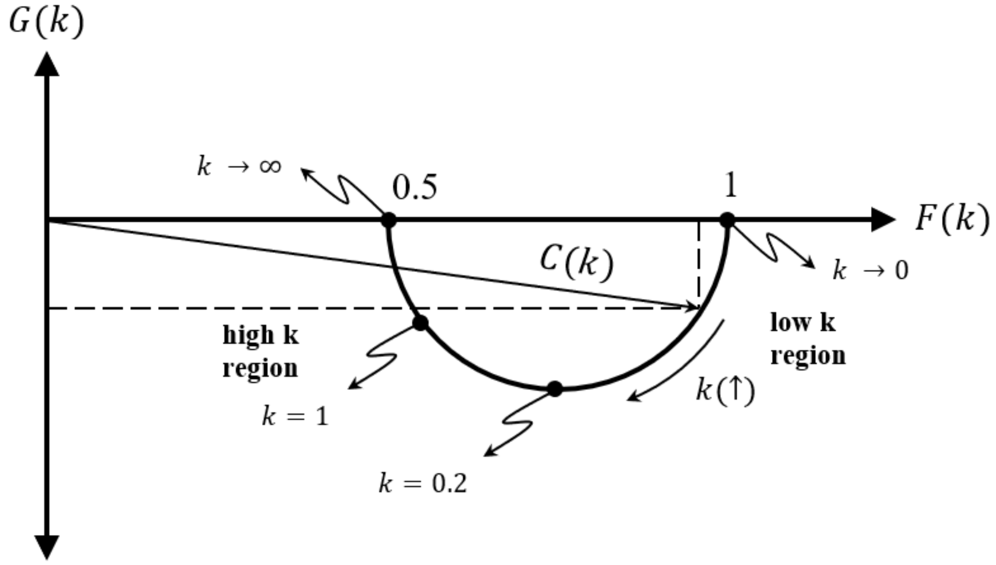

Figure 2-12 Theodorsen Function on Complex Plane

2.5. Aeroelastic Background of ZAERO©

2.5.1. ZAERO© Overview

ZAERO© is a software that incorporates the essential tools utilized for aeroelastic design and analysis [55]. ZAERO© includes five main modules that are used for the aeroelastic stability analyses;

- High Fidelity Geometry (HFG) Module: It is utilized for creating aerodynamic panel model of a full aircraft configuration.
- 3D Spline Module: It provides displacement and force transferal between the user defined structural grid points and the aerodynamic boxes generated by HFG module.

- Unified Aerodynamic Influence Coefficient Module: It yields Aerodynamic Influence Coefficient (AIC) matrices at any desired Mach number.
- Modal Data Importer: It is used for importing modal information (i.e. eigenvalues and eigenvectors of the discrete system) coming from different finite element method solvers such as MSC Nastran, ANSYS etc.
- Aeroelastic Analysis Module: It combines all data prepared by other four modules and perform wide range of aeroelastic analyses from flutter estimation to aeroservoelastic optimization and transient response analysis due to the discrete or continuous gust.

The sub-chapters of 2.5.2 and 0 are generally dependent on the ZAERO Theoretical Manual Version 9.2, 3rd Edition. The one who needs further technical details regarding aeroelastic theory embedded in ZAERO© and wonders complete capabilities of the software can refer ZAERO Theoretical Manual Version 9.2, 3rd Edition and ZAERO User's Manual Version 9.2, 3rd Edition respectively [55], [56].

2.5.2. Aeroelastic Foundation of ZAERO©

The equation of motion can be derived as in Eq. (2.34) for discrete systems

$$[M]\ddot{x}(t) + [K]x(t) = F(t, x(t)) \qquad (2.34)$$

where $[M]$ is the mass matrix, $[K]$ is the stiffness matrix, $x(t)$ is the structural deformation and $F(t, x(t))$ represents the total aerodynamic force matrix. Force matrix can be divided into two main parts; aerodynamic forces due to the structural deformation and other external forces

$$F\big(t, x(t)\big) = F_a\big(t, x(t)\big) + F_e(t, x(t))$$

Due to the feedback aerodynamic force caused by the instantaneous structural deformation, the dynamic system is assumed to be self-excited. The feedback system mentioned can be observed from Eq. (2.35) and in Figure 2-13

$$[M]\ddot{x}(t) + [K]x(t) - F_a\big(t, x(t)\big) = F_e(t, x(t)) \qquad (2.35)$$

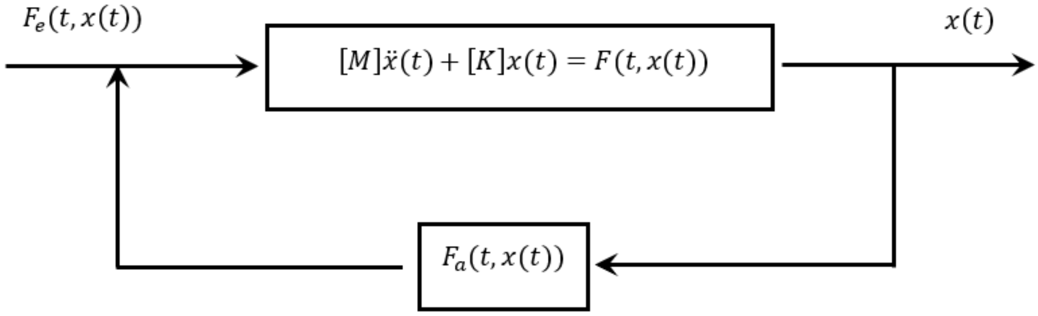

Figure 2-13 Aeroelastic Functional Diagram (Closed Loop)

The feedback aerodynamic force, $F_a\big(t,x(t)\big)$ shows generally non-linear behavior with respect to the structural deformation, $x(t)$. However, if the structural oscillation amplitudes are assumed to be small, i.e. $x(t) \ll 1$, then the aerodynamic force shows linear behavior in regard to the structural deformation. This is called the amplitude linearization method. Amplitude linearization enable us to find a transfer function between $F_a\big(t,x(t)\big)$ and $x(t)$ by means of convolution integral as in Eq. (2.36)

$$F_a\big(t,x(t)\big)=q_\infty\int_0^t H\left(\frac{U}{b}(t-\tau)\right)x(\tau)d\tau \tag{2.36}$$

Here function of H represents aforementioned aerodynamic transfer function, q_∞ is the dynamic pressure, b is the half chord length and U is the free stream velocity. The Laplace domain counterpart of Eq. (2.36) is then acquired as in Eq. (2.37).

$$F_a\big(s,x(s)\big)=q_\infty\overline{H}\left(\frac{sb}{U}\right)x(s) \tag{2.37}$$

$\overline{H}$ is the Laplace counterpart of the aerodynamic transfer function. If Eq. (2.37) is written in matrix form, $\overline{H}$ is called the Aerodynamic Influence Coefficient (AIC) matrix as in Eq. (2.38)

$$\{F_a(s)\}=q_\infty\left[AIC\left(\frac{sb}{U}\right)\right]\{x(s)\} \tag{2.38}$$

Assuming there is no external force acting on the lifting surface apart from the feedback aerodynamic force $F_a\big(t,x(t)\big)$, Eq. (2.35) can normally be solved by use of a time-marching method in time domain with the initial conditions $x(0)$ and $\dot{x}(0)$ being specified at $t = 0$. However, this computational procedure takes too much time due to the inclusion of the non-linear unsteady aerodynamic solution method known as the Computational Fluid Dynamics (CFD). In lieu of that, the general tendency of the aerospace industry is in the direction of recasting Eq. (2.35) into a set of linear systems and solve the complex eigenvalue problem in the Laplace domain.

With Eq. (2.38) at hand, Eq. (2.35) can be easily converted into the Laplace domain by assuming there is no external forces

$$\left[s^2\overline{M} + \overline{K} - q_\infty AIC\left(\frac{sb}{U}\right)\right]\{x(s)\} = 0 \tag{2.39}$$

Eq. (2.39) is an eigenvalue problem in terms of s and the eigensolution of the problem gives us the stability boundary of the closed loop system plotted in Figure 2-13.

As it is mentioned in Section 2.5.1, ZAERO© imports the modal solution of the dynamic structural system from an external structural solver. Since the finite element models of the aircrafts normally contain many degrees of freedom, the size of the mass and stiffness matrices in Eq. (2.39) are usually very large. To resolve this problem, the modal reduction approach can be introduced.

$$\{x(s)\} = [\phi]\{q(s)\} \tag{2.40}$$

Here $[\phi]$ is the modal matrix including lower order of natural modes which usually trigger the flutter, $\{q(s)\}$ is the generalized coordinates according to which the eigenvectors are determined.

Substituting Eq. (2.40) into Eq. (2.39) and pre-multiplying all terms with $[\phi]^T$ yields the classical flutter equation in the Laplace-domain

$$\left[s^2 M_r + K_r - q_\infty Q\left(\frac{sb}{U}\right)\right]\{q(s)\} = 0 \tag{2.41}$$

where

$M_r = [\phi]^T\overline{M}[\phi]$ is the generalized (or reduced) mass matrix

$K_r = [\phi]^T \overline{K} [\phi]$ is the generalized (or reduced) stiffness matrix

$Q\left(\frac{sb}{U}\right) = [\phi]^T AIC \left(\frac{sb}{U}\right)[\phi]$ is the generalized (or reduced) aerodynamic force matrix due to structural deformation

The size of matrices in Eq. (2.41) is lower than the ones given in Eq. (2.39). It is more effective to solve such an eigenvalue problem compared to Eq. (2.39).

The above derivations from Eq. (2.35) to the classical flutter equation in the Laplace-domain are made up of only matrix manipulations with known matrices apart from the AIC matrix. To be able to solve Eq. (2.41) for flutter estimation AIC matrix has to be derived in the frequency domain. In fact, the major capability of ZAERO© is to generate such AIC matrices for different types of aircraft configurations utilizing the embedded aerodynamic solvers based on the simple harmonic motion assumption.

There are five unsteady aerodynamic solvers which are incorporated in ZAERO©; ZONA6, ZONA7, ZTRAN, ZSAP and ZONA7U computing the AIC matrices in subsonic, supersonic, transonic, sonic and hypersonic flow regimes, respectively. ZONA6 subsonic aerodynamic method is utilized in the flutter analyses performed within the scope of this thesis

ZONA6 is adopted to use user defined panel models as shown in Figure 2-14 for solving the unsteady potential integral equation in the context of simple harmonic motion which is based on the reduced frequency (see Eq. (2.31)).

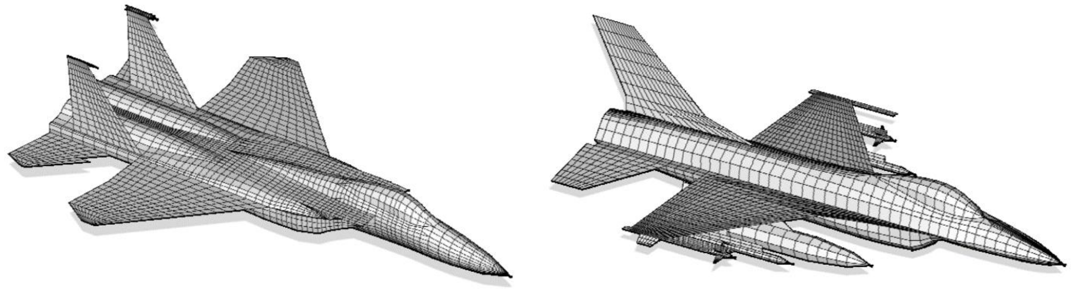

F-15 Fighter Aircraft **F-16 Fighter Aircraft**

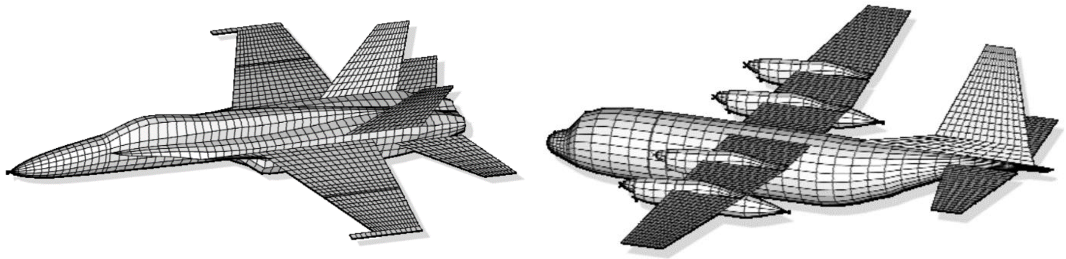

F-18 Fighter Aircraft **C-130 Transport Aircraft**

Figure 2-14 Aerodynamic Panel Models in ZAERO©

Each aerodynamic panel which is named specifically as aerodynamic box has control point on which the boundary conditions are imposed. The integral equations are solved in each aerodynamic box consecutively and the assembly of these elementary integrals constitutes a matrix whose coefficients associates the structural deformation and resulting aerodynamic forces. This matrix is the so-called Aerodynamic Influence Coefficient (AIC) matrix that has a great importance for all aeroelastic analyses conducted in the frequency domain.

The relation between the structural deformation and the resultant aerodynamic force is given in Eq. (2.42) through the AIC matrix

$$\{F_k\} = q_\infty [AIC(ik)]\{h_k\} \tag{2.42}$$

where $\{h_k\}$ is the structural deformation vector defined at the aerodynamic boxes, $\{F_k\}$ is the aerodynamic force vector at the aerodynamic boxes. It is important to note that the AIC matrices in Eq.s (2.38) and (2.42) are not the same. In fact, both are the transfer functions between the structural deformation and aerodynamic forces; however, the first one is computed based on the structural grid points in the Laplace domain and the second one is on the aerodynamic boxes in the reduced frequency domain.

Since the AIC matrix is calculated per aerodynamic panel model which is substantially different from the finite element model that is externally provided, a problem emerges regarding the force and displacement transferal between the aerodynamic boxes and the structural grid points. This issue is resolved by the spline matrix generated for associating or interpolating the displacements coming from the structural model to those at aerodynamic panels. There are four different spline methods incorporated in ZAERO©; flagged by the user and then it creates the spline matrix $[G]$ such that

$$\{h_k\} = [G]\{x\} \tag{2.43}$$

where $\{x\}$ is the displacement vector at the structural grid point. Once this spline matrix is calculated, it is also utilized for the force transferal from the aerodynamic control points to the structural grid points such that

$$\{F_a\} = [G]^T\{F_k\} \tag{2.44}$$

If Eq. (2.43) is inserted into Eq. (2.42) and the resulting expression is plugged into Eq. (2.44), Eq. (2.45) is acquired as follows

$$\{F_a\} = q_\infty[G]^T[AIC(ik)][G]\{x\} \tag{2.45}$$

If one applies the modal reduction approach to the splined form of AIC matrix, it yields

$$Q(ik) = [\phi]^T[G]^T[AIC(ik)][G][\phi] \tag{2.46}$$

As it is mentioned previously, ZAERO© solves the flutter in the frequency domain with the assumption of simple harmonic motion. Therefore, Eq. (2.41) has to be converted from the Laplace domain (transient motion) to the reduced frequency domain (simple harmonic motion) by replacing $Q\left(\frac{sb}{U}\right)$ with $Q(ik)$ and s by $i\omega$. This gives

$$[-\omega^2 M_r + K_r - q_\infty Q(ik)]\{q\} = 0 \tag{2.47}$$

2.5.3. Flutter Solution Techniques

Recall Eq. (2.41) which is the classical flutter equation in the Laplace domain

$$\left[s^2 M_r + K_r - q_\infty Q\left(\frac{sb}{U}\right)\right]\{q(s)\} = 0$$

To convert this equation to an eigenproblem, one can introduce a non-dimensional Laplace parameter p such that

$$p = \frac{sb}{U} = g + ik = \gamma k + ik$$

Then Eq. (2.41) becomes

$$\left[\left(\frac{U}{b}\right)^2 M_r p^2 + K_r - \frac{1}{2}\rho U^2 Q(p)\right]\{q(s)\} = 0 \qquad (2.48)$$

Eq. (2.48) is the p-method equation which is capable of providing the true damping behavior of the aeroelastic system. However, since many aeroelastic problem solvers such as ZAERO© utilizes unsteady aerodynamics expressed in the reduced frequency domain under the assumption of simple harmonic motion, such three methods are introduced in this section.

2.5.3.1. K-Method

As a stability measure if one adds an artificial structural damping parameter to Eq. (2.47), the so-called K-method flutter equation can be obtained as in Eq. (2.49)

$$[-\omega^2 M_r + (1 + ig_s)K_r - q_\infty Q(ik)]\{q\} = 0 \qquad (2.49)$$

where g_s is the virtual structural damping. K-method is consistent with the simple harmonic motion assumption and it is sufficient to predict the flutter onset speed at zero damping.

To transform Eq. (2.49) to pure complex eigenvalue problem, dynamic pressure can be manipulated as follows

$$q_\infty = \frac{1}{2}\rho U^2 = \frac{1}{2}\rho\left(\frac{\omega b}{k}\right)^2$$

Then the K-method eigenproblem is obtained as in Eq. (2.50) by inserting above relation into Eq. (2.49) and dividing the resultant equation by $-\omega^2$

$$\left[M_r + \frac{\rho}{2}\left(\frac{b}{k}\right)^2 Q(ik) - \lambda K_r\right]\{q\} = 0 \qquad (2.50)$$

where $\lambda = \frac{(1+ig_s)}{\omega^2}$. For a given reduced frequency, λ can be solved by the eigenvalue analysis. Since the solution rationale of K-method is depending on straightforward complex eigenvalue analysis, it is efficient and robust. However, the main imperfection of the method is that added artificial structurally damping does not really exist and other than $g_s = 0$, frequency and damping characteristics do not accurately represent the system behavior. In the industry, a reliable damping estimation is crucial to acquire real aeroelastic properties at critical flight regimes since this information leads the engineers to perform wind tunnel or flight flutter tests in the design phase of the aircraft if necessary.

2.5.3.2. P-K Method

Due to the drawbacks of K-method mentioned in the Section 2.5.3.1, Irwin and Guyett have proposed firstly the P-K method as a primary tool for finding flutter boundary in 1965 [57]. Similar to the K-method, P-K method substitutes the generalized aerodynamic forces matrix $Q\left(\frac{sb}{U}\right)$ with $Q(ik)$ and it defines also a non-dimensional parameter p which is the same as that in the p-method

$$p = \frac{sb}{U} = g + ik = \gamma k + ik$$

where γ is the transient decay rate coefficient that is desired for estimating the accurate damping characteristics of the system. Then Eq. (2.51) becomes

$$\left[\left(\frac{U}{b}\right)^2 M_r p^2 + K_r - \frac{1}{2}\rho U^2 Q(ik)\right]\{q\} = 0 \tag{2.51}$$

Eq. (2.51) is the Hassig's P-K method equation which is a mathematically inconsistent formulation since the eigenvalue of p is expressed as damped sinusoidal motion due to the γ while the aerodynamic influence coefficient matrix $Q(ik)$ in reduced frequency domain is acquired based on the assumption of undamped simple harmonic motion [58]. However, it still gives accurate flutter results.

Even though the predicted flutter onset speed and flutter frequency results obtained by P-K method agree well with these of the K-method, the general opinion is that more realistic damping and frequency curves are achieved compared to those of the K-method.

2.5.3.3. g-Method

Using a damping perturbation method, Chen has proposed to add a first order damping term in the flutter equation [46]. It leads to a new flutter solution technique, i.e. g-method working in frequency domain. It is the method, by the way, primarily used in ZAERO© for estimating the flutter.

Assume that there exists an analytical function such that $Q(p) = Q(g + ik)$ in the domain of $g \geq 0$ and $g < 0$. Then $Q(p)$ can be expanded along the imaginary axis (i.e. $g = 0$) for small g values using the damping perturbation method

$$Q(p) \approx Q(ik) + g\left.\frac{\partial Q(p)}{\partial g}\right|_{g=0}$$

The term of $\left.\frac{\partial Q(p)}{\partial g}\right|_{g=0}$ in above equation is in the Laplace domain and it has to be converted to k-domain. To do this, again the analyticity of the $Q(p)$ is used to satisfy the Cauchy-Riemann equations such that

$$\frac{\partial(Re(Q(p)))}{\partial g} = \frac{\partial(Im(Q(p)))}{\partial k} \qquad \frac{\partial(Im(Q(p)))}{\partial g} = -\frac{\partial(Re(Q(p)))}{\partial k}$$

These equalities yield the following general condition

$$\frac{\partial Q(p)}{\partial g} = \frac{\partial Q(p)}{\partial (ik)}$$

Then the term that we would like to convert into the k-domain can be replaced by

$$\left.\frac{\partial Q(p)}{\partial g}\right|_{g=0} = \left.\frac{\partial Q(p)}{\partial (ik)}\right|_{g=0} = \frac{dQ(ik)}{d(ik)} = Q'(ik)$$

Since ZAERO© computes the $Q(ik)$ per provided reduced frequency and Mach number pairs on the aerodynamic panel model, the derivative of the all matrix elements can be numerically extracted by a central differencing scheme apart from the zero reduced frequency on which a forward differencing scheme has to be employed.

If the derivative term is plugged into the expanded form of the $Q(p)$ above, Eq. (2.52) can be obtained for small g values

$$Q(p) \approx Q(ik) + gQ'(ik) \tag{2.52}$$

If Eq. (2.52) is substituted into Eq. (2.48), Eq. (2.53) is acquired as

$$\left[\left(\frac{U}{b}\right)^2 M_r p^2 + K_r - \frac{1}{2}\rho U^2 Q'(ik) g - \frac{1}{2}\rho U^2 Q(ik)\right]\{q\} = 0 \tag{2.53}$$

In case of the zero g value, the g-method and p-k method equations becomes the same. It means they yield same flutter boundary for zero damping.

CHAPTER 3

WING-LIKE STRUCTURE AND DESIGN DETAILS

3.1. General Introduction

In the scope of this thesis, a wing-like structure having three payload stations is studied from the standpoint of flutter characteristics. As it is mentioned in the Introduction Chapter, the structure is subjected to the flutter certification flow starting from the determination of its dynamic behavior to the wind tunnel flutter test. In this chapter, the design details of the wing-like structure are given together with its crucial properties to achieve the aforementioned certification study.

Before starting the design of the wing-like structure, the requirements of the intended scope of the thesis was reviewed from the point of feasibility. Analysis and test resources were investigated and several conceptual analyses were performed. By the year of 2018 there was only one large-scale wind tunnel facility working in low subsonic regime in Turkey. It is Ankara Wind Tunnel (ART) operated by TUBITAK SAGE Defense Industries Research and Development Institute. Since the wind tunnel is capable of conducting the tests with a maximum speed of 85 m/s, the requirement of designing a wing-like structure experiencing the flutter at the speed lower than 85 m/s has arisen. Over this necessity, the essential design parameters that are directly related to the flutter characteristics have been decided to be optimized to achieve the minimum flutter onset speed. In his experimental study, W. G. Molyneux examined the effects of the sweep angle, taper ratio and position of the elastic axis on the flutter and ended up with a directive summary table [41]. In the table, the flutter onset speeds of a wing measured by wind tunnel experiments are given according to four different taper ratios and sweepback angles, and three different positions of the elastic axis. When the results are examined, it is observed that the taper ratio of 0.75 and the elastic axis at half chord of the wing yield the minimum flutter speed. For sweepback angle, in general, there is a tendency that the flutter speed firstly decreases as the angle of sweep increases, reaches a minimum value around 10° and then starts to increase rapidly as the sweepback rises. In the light of this information, several flutter analyses were performed with different wing geometries created by changing these design parameters. In parallel with his wind tunnel experimental study, it was also observed that the taper ratio of 0.75 and the elastic axis at the mid chord produce the minimum value of the flutter speed. The flutter speed trend with respect to the sweepback angle, on the other hand, reaches its minimum at about 15° for the wing-like structure. Utilizing these preliminary flutter analysis results, final design of the wing-like structure was frozen as the details of it are given in sub-section of 3.2.

3.2. General Dimensions and Assembly of the Subparts

The general dimensions of the wing-like structure are given in Figure 3-1. It is manufactured from sheet aluminum metal with 3 mm thickness. The taper ratio of the wing is 0.75 and it has a back-sweep angle of 15°. The elastic axis of the empty wing is directly the mid-chord axis due to the constant profile thickness.

At this point, it is useful to emphasize that having forward sweep angle causes that the divergence occurs before the flutter. Therefore, a positive back-sweep angle was set to achieve the flutter prior to the divergence.

There are exactly same three payloads installed on the wing with the help of the different pylons through the fastener holes shown on the Figure 3-1. One payload consists of three sub components; the cap, the main body and the additional weight. The main body is hollow cylinder whose wall thickness is 5 mm. The cap and the additional weight are designed in a way to be close fit in the main body. The general dimensions and assembly of these three parts are given in Figure 3-2. The reason of having an additional weight at the back of the main payload is to reduce the torsional mode frequency of the wing and drop the flutter onset speed implicitly.

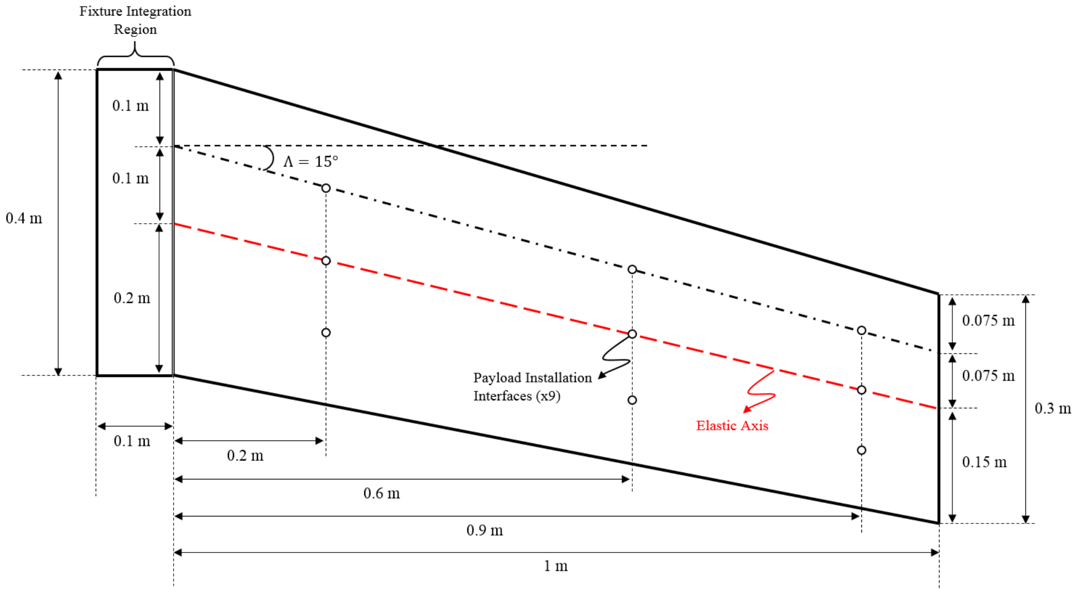
Fixture Integration Region
0.1 m
0.1 m
0.4 m
0.2 m
Λ = 15°
0.075 m
0.075 m
0.3 m
0.15 m
Payload Installation Interfaces (x9)
Elastic Axis
0.1 m
0.2 m
0.6 m
0.9 m
1 m

Figure 3-1 General Dimensions of the Wing-Like Structure

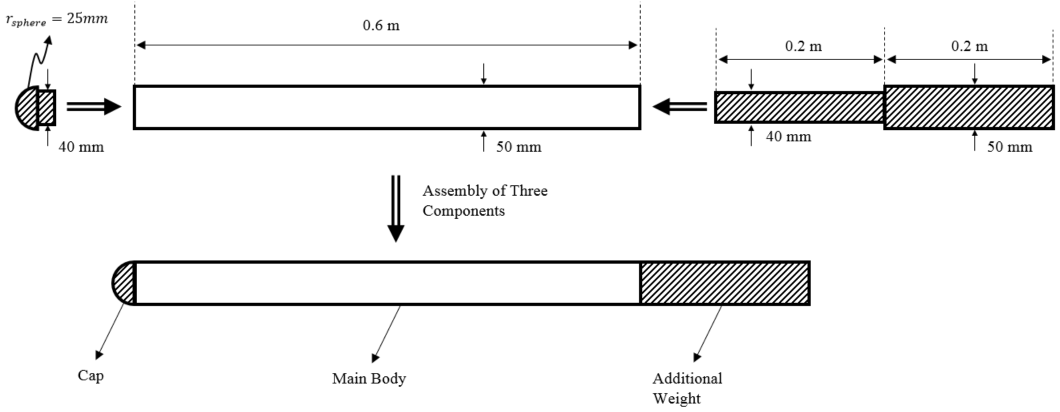
$r_{sphere} = 25mm$
40 mm
0.6 m
50 mm
0.2 m
0.2 m
40 mm
50 mm
Assembly of Three Components
Cap
Main Body
Additional Weight

Figure 3-2 Payload Design Details

Unlike the payloads there are three pylons with different dimensions due to the decreasing chord length in the spanwise direction of the wing. They have the same rectangular cross section of 10 x 20 mm. Their lengths are 230, 210, and 195 mm from root to tip, respectively. The payload, pylon and wing are assembled with three screws torqued into the threads on the payload. The details are given in Figure 3-3.

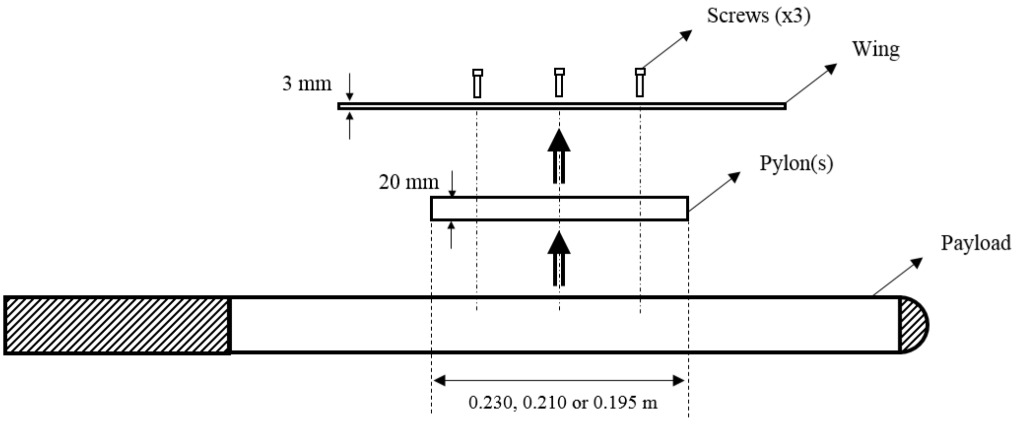
Screws (x3)
Wing
3 mm
Pylon(s)
20 mm
Payload
0.230, 0.210 or 0.195 m

Figure 3-3 Assembly of the Payload, Pylon and Wing-Like Structure

The wing-like structure is constrained to the ground with the help of a two-piece with 14 connection points. Two fixture parts and the wing are integrated to each other through the 7 fasteners. The fixture was designed in a way to be sufficiently rigid not to influence the dynamic behavior of the wing-like structure so much. The assembly and design details are given in Figure 3-4.

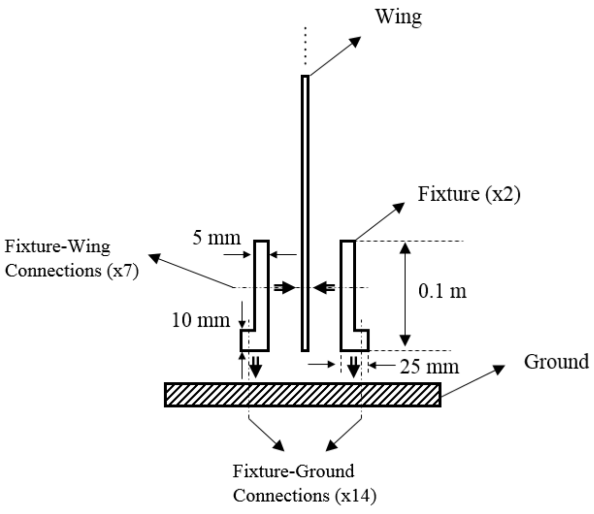
Wing
Fixture (x2)
Fixture-Wing Connections (x7)
5 mm
0.1 m
10 mm
25 mm
Ground
Fixture-Ground Connections (x14)

Figure 3-4 Fixture Design Details

3.3. Materials

The materials and properties of the parts constituting the assembly of the wing-like structure are given in Table 3-1. All the parts apart from the cap of the payloads were manufactured from Aluminum 2024 T3. The cap was processed from ABS (Acrylonitrile Butadiene Styrene) filaments in a commercial 3D printer to decrease the manufacturing effort and cost. The material properties of Al 2024 T3 are taken from Metallic Materials Properties Development and Standardization (MMDPS-08) [59]. The ABS filament properties are not needed since the caps are represented as point mass in finite element model and their measured masses are directly utilized in the models.

Table 3-1 Materials

Part Name	**Material**	**Elastic Modulus [MPa]**	**Density [kg/m^3]**	**Poisson Ratio**
Wing-like Structure	Al 2024 T3	73500	2780	0.33
Pylon				
Main Body of Payload				
Additional Weight				
Fixture				
Cap of the Payload	ABS Filament	-	-	

3.4. Definitions of the Configurations

There are totally 8 different combinations that three payloads can be integrated on the wing-like structure. The definitions of these configurations are given in Figure 3-5.

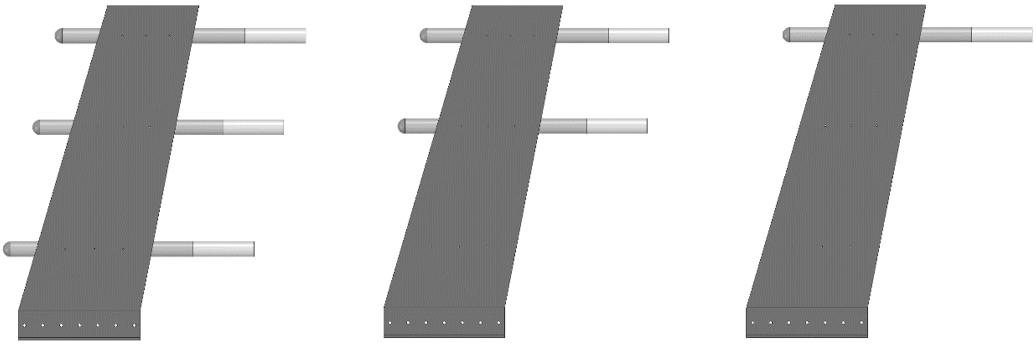

Configuration-1 **Configuration-2** **Configuration-3**

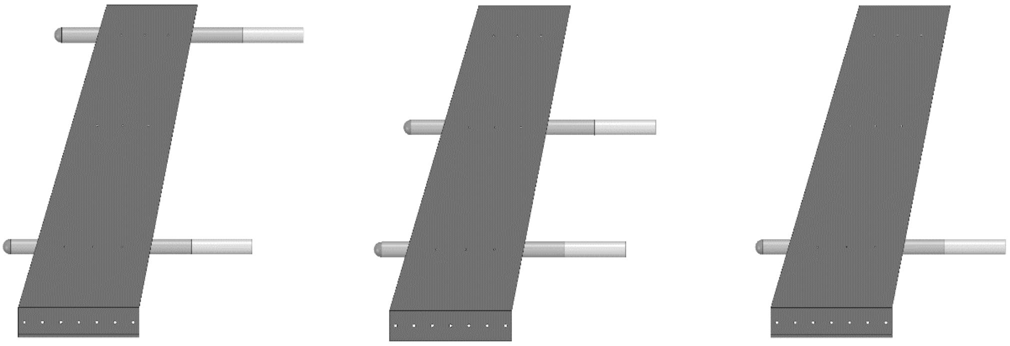

Configuration-4 **Configuration-5** **Configuration-6**

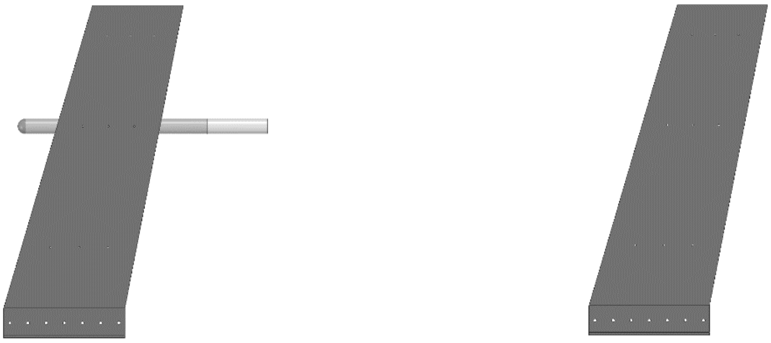

Configuration-7 **Configuration-8**

Figure 3-5 Definitions of Configurations

CHAPTER 4

DYNAMIC MODEL GENERATION

4.1. General Introduction

In this chapter, all efforts required for the dynamic model generation are presented. Firstly, the section of 4.2 gives the details of finite element modal analysis of all configurations. Secondly, ground vibration tests of each configurations are outlined in the section 4.3. Lastly, the modal updating studies are elaborated with the section 4.4.

4.2. Finite Element Modal Analysis

In this section, the finite element modal analysis results of each configuration are given. All the analyses were carried out in MSC Nastran© and *.f06 output files were extracted to be used in flutter analyses with ZONA ZAERO©. Since the flutter is generally related to the bending and/or torsional modes of the structure, only the first three modes were calculated.

4.2.1. Finite Element Modelling

Finite element models of all configurations were prepared in Altair Hypermesh© and input files being compatible with MSC Nastran© were acquired. Since the finite element modal analysis is a solution of linear eigenvalue problem, the definition of non-linear elements was abstained in the finite element model. For the sake of high solution accuracy, quad and hex elements were chosen per the type of the part. As it is mentioned before, the cap of the payloads was modelled as point mass and connected to the payload with RBE3 elements. Bolted connections were performed with RBE2 elements. The Table 4-1 gives the details of finite element modelling. As an example, the FE model of configuration-1 is given in Figure 4-1.

Table 4-1 Element Types and Sizes

Part Name	Element Type	Element Size [mm]
Wing-like Structure	2D QUAD4	20
Pylon		
Main Body of Payload		
Fixture		
Additional Weight	3D Solid HEX8	20
Cap of the Payload	0D CONM2	-

Table 4-2 Finite Element Model Information

# of Grid Points	3682
# of Elements	3149
# of Rigid Elements	6
# of Rigid Element Constraints	4194
# of Degrees of Freedom	17724
# of Non-zero Stiffness Terms	549150

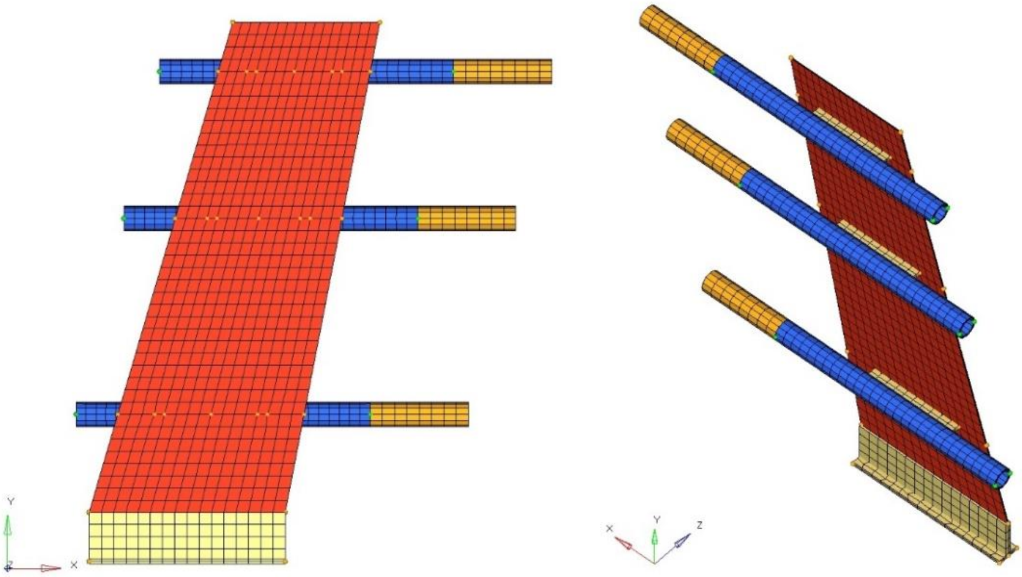

Figure 4-1 Finite Element Model of Configuration-1

The finite element models belonging to other configurations are given in Appendix A. In order to show the mesh convergence, three finite element models having different mesh densities are compared each other and the results are given in Appendix B.

Since the wing-like structure is fastened to the ground via the two-piece fixture, the boundary conditions in the FE model were defined at these locations in the FEM. To utilize them in modal updating works, 14 CBUSH and corresponding PBUSH cards were created to represent the ground connections. All the stiffness values in 6 axes (3 translational, 3 rotational) were set to 10^6 N/mm in PBUSH cards and ground side of CBUSH elements were fixed in 6 axes as it is seen in the Figure 4-2.

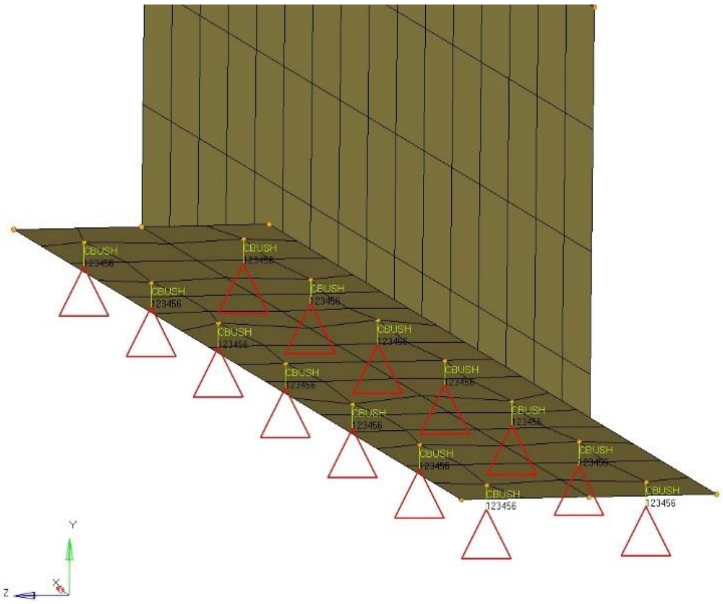

Figure 4-2 Fixed Boundary Conditions and CBUSH Definitions

4.2.2. Numerical Natural Frequencies and Mode Shapes of the Wing

For each configuration, all numerical natural frequencies are given in Table 4-3. The first three mode shapes of configuration-1 are given in Figure 4-3, Figure 4-4 and Figure 4-5, respectively. For other configurations, the associated mode shapes are outlined in Appendix D.

Table 4-3 Numerical Natural Frequencies

Conf. No	Mode 1 [Hz]	Mode 2 [Hz]	Mode 3 [Hz]
1	1.07	4.05	6.33
2	1.04	3.78	6.56
3	1.15	4.19	13.06
4	1.18	4.36	9.27
5	1.79	5.49	10.27
6	2.65	9.70	14.25
7	1.74	5.11	12.47
8	2.65	14.99	17.33

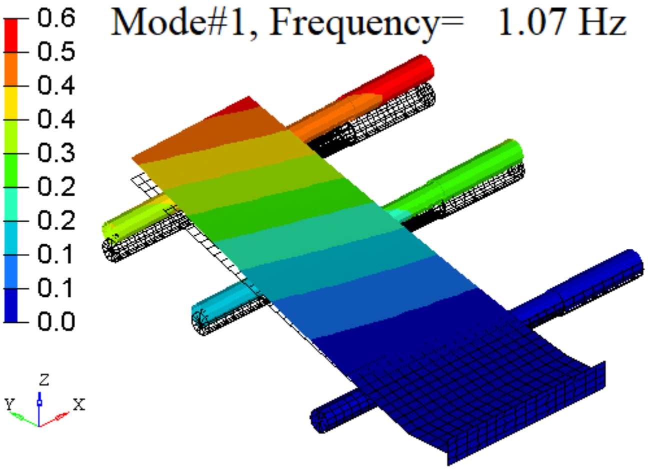
0.6
0.5
0.4
0.4
0.3
0.2
0.2
0.1
0.1
0.0
Mode#1, Frequency= 1.07 Hz
Z
Y
X

Figure 4-3 Numerical 1st Bending Mode Shape of Configuration-1

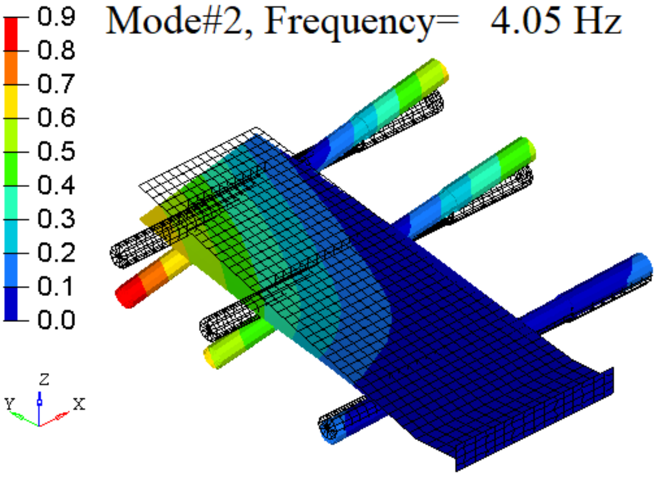
0.9
0.8
0.7
0.6
0.5
0.4
0.3
0.2
0.1
0.0
Mode#2, Frequency= 4.05 Hz
Z
Y
X

Figure 4-4 Numerical Torsion Mode Shape of Configuration-1

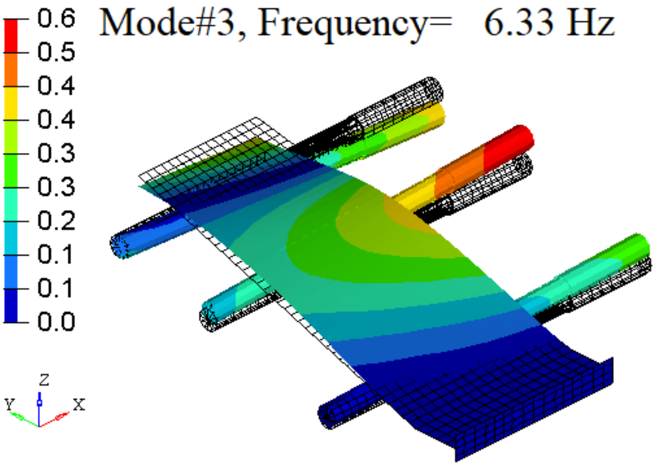

Figure 4-5 Numerical 2nd Bending Mode Shape of Configuration-1

In order to correlate the numerical analysis results, ground vibration tests were performed for each configuration. As it is explained in Section 4.3.1, there were totally 8 accelerometers and 1 impedance head instrumented on the wing-like structure. Since their masses are relatively small compared to the total mass of the wing, they do not affect the dynamic behavior of the wing. In order to demonstrate this, all the transducers were modeled as concentrated masses, i.e. CONM2, and finite element modal analysis was re-performed. The results are given in Appendix C.

4.3. Ground Vibration Test

In this section the ground vibration tests of each configuration are discussed. The test data were collected with Simcenter Scadas© data acquisition system and raw FRFs were processed using Polymax© algorithm embedded in Simcenter Testlab© to extract the test mode frequencies, shapes and modal damping. Only first three test modes were calculated in compatible with the finite element modal analysis results.

4.3.1. Test Setup

Since the first three modes are intended to be acquired, the instrumentation of accelerometers was arranged in a way to extract the modes of the first bending, the torsion and the second bending per the finite element modal analysis results. There are totally 10 accelerometers and 1 impedance head utilized in the test setup. The first 6 accelerometers are placed in line with the three payloads two by two. The seventh and the eighth ones are in the root of the wing-like structure and other two are on the ground to see how it is excited and whether it moves relative to the wing. Any accelerometer was not instrumented on either pylons or payloads since the flutter is directly related to the global modes of the wing and there is no possibility to have an interaction between the local modes of the payloads and the wing global modes due to the stiff pylons.

The impedance head, which includes a load cell and an accelerometer, was bonded to the wing tip where it is excited with an electromagnetic shaker. While exciting the system, the shaker is attached to the impedance head through a stinger. Stingers, also called as quills, are generally designed to be threaded rod having high axial stiffness and low bending stiffness. The force transducer utilized between the stinger and the structure decouples the system in axial direction. Its bending stiffness, on the other hand, may influence the higher modes of the structure which have more curvature compared to the lower ones [60]. In order to excite the structure properly in low frequency band, i.e. 1-10 Hz, and achieve the good coherences between the input and output signals, the wing was decided to be excited at the tip in compatible with the ground vibration tests executed in aerospace industry [61], [62].

The GVT stick model was constituted by inserting the location of the transducers to the Simcenter Testlab©. The instrumentation details and the stick model are shown on Figure 4-6.

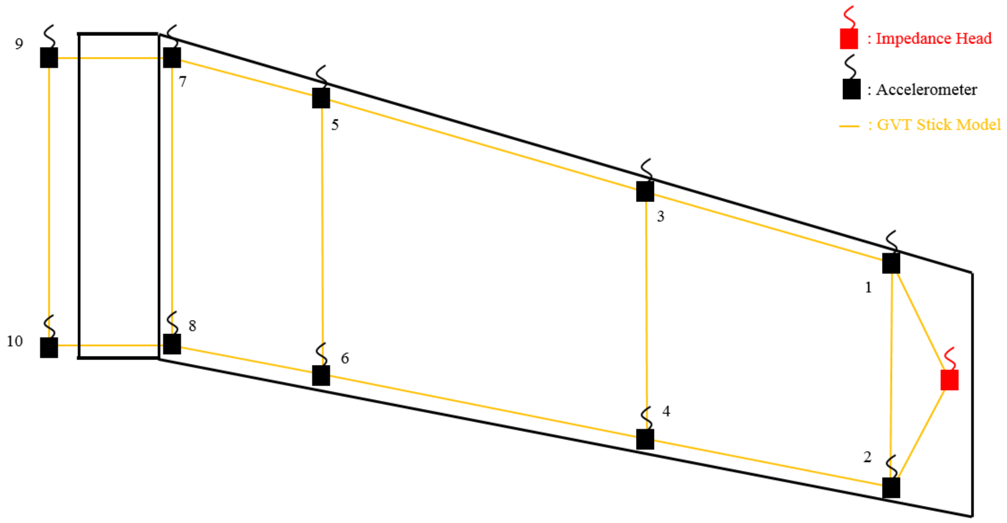

Figure 4-6 GVT Setup and Stick Model

Since the modal updating is dependent on the modal test results and it affects the calculated flutter onset speeds implicitly, the modal test was performed by using the wind tunnel flutter test fixture which is built from wood to satisfy the same boundary condition. The test setup prepared for the configuration-1 is given on Figure 4-7.

In accordance with the finite element modal analysis results, the wing-like structure was excited in a related frequency bandwidth for each configuration. The number of spectral lines, the sampling frequencies and the applied forces were tuned to catch the best FRF peaks belonging to the modes of the structure. The non-linear effects were checked by decreasing and increasing the level of excitation force and whether the peaks of the FRF curves shift to the right or left was observed. In each test, the structure was excited 20 times and collected FRFs were averaged before the analysis of the test data. The modal damping values were calculated by using 3 dB method in Simcenter Testlab©.

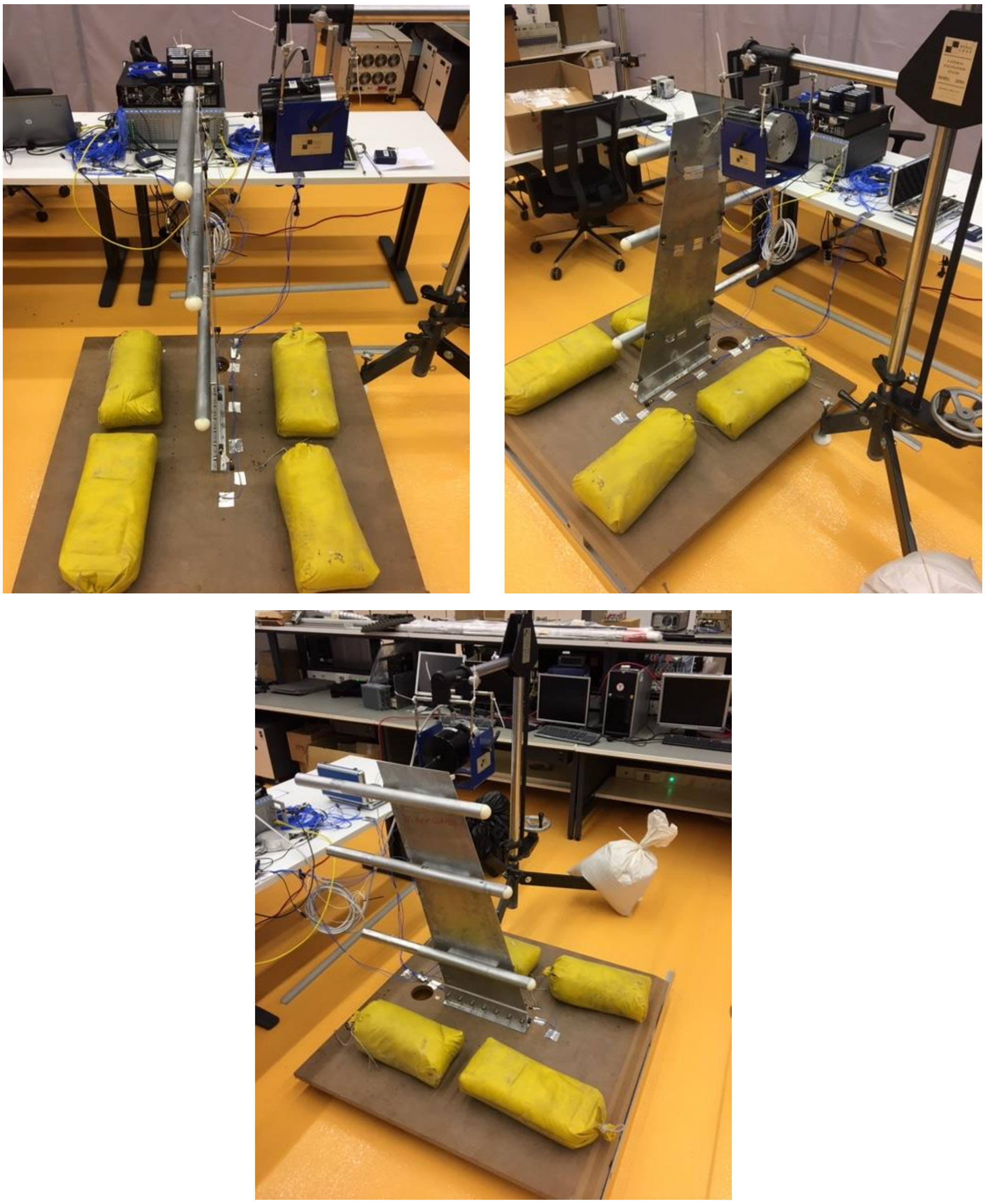

Figure 4-7 Configuration-1 GVT Setup

4.3.2. Ground Vibration Test Results

For each configuration, all test mode frequencies with modal damping ratios are given in Table 4-4 Ground Vibration. The first three mode shapes of configuration-1 are given in Figure 4-8, Figure 4-9 and Figure 4-10, respectively. For other configurations, the mode shapes are outlined in Appendix E.

Table 4-4 Ground Vibration Test Mode Frequencies and Modal Damping

Conf. No	Mode 1 [Hz] / Damping (%)	Mode 2 [Hz] / Damping (%)	Mode 3 [Hz] / Damping (%)
1	1.01 / 1.46	4.13 / 0.82	5.86 / 0.83
2	1.00 / 2.46	3.95 / 0.49	6.21 / 0.90
3	1.22 / 1.25	4.42 / 0.50	12.22 / 0.39
4	1.22 / 1.36	4.52 / 1.74	8.27 / 0.27
5	1.70 / 2.09	5.46 / 0.65	9.81 / 0.24
6	2.87 / 2.20	8.85 / 0.81	13.98 / 0.56
7	1.78 / 1.68	5.34 / 0.42	12.45 / 1.30
8	2.95 / 1.18	15.21 / 0.58	18.56 / 0.60

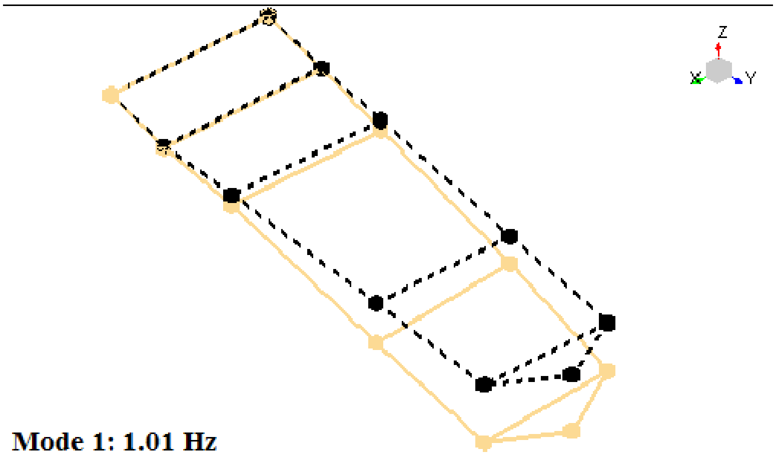

Figure 4-8 Test 1st Bending Mode Shape of Configuration-1

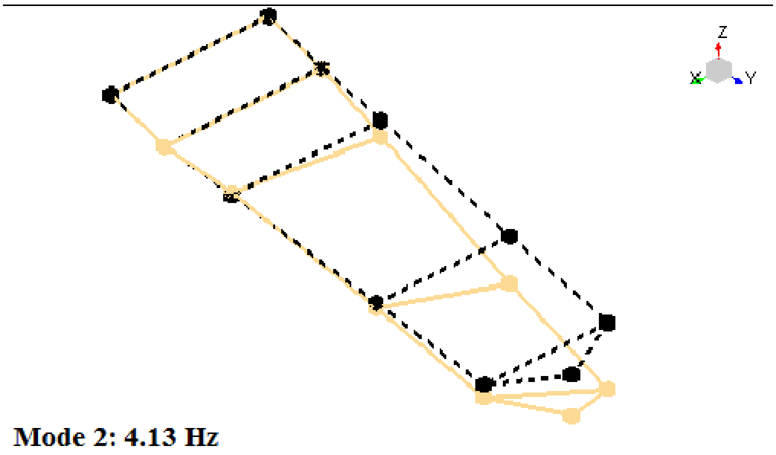

Figure 4-9 Test Torsion Mode Shape of Configuration-1

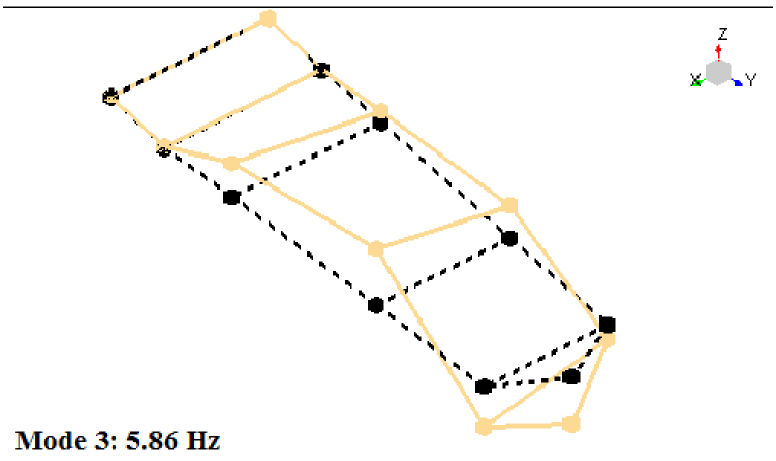

Figure 4-10 Test 2nd Bending Mode Shape of Configuration-1

4.4. Modal Updating

In this section the modal updating studies were given. The ground vibration test and finite element modal analysis data were read by the modal updating tool FEMTools©, the parameters and responses were identified in it and the parameters were iterated per the dictated convergence criteria to achieve the test mode frequencies and shapes with the FE model.

4.4.1. Correlation of Finite Element Analysis and Ground Vibration Test Results

Before starting the modal updating, it was designated that which configuration needs to be updated by conducting correlation analysis between the experimental and numerical modal analysis results. The Table 4-5 gives the comparison of the finite element modal analysis and ground vibration test mode frequencies for eight configurations.

Table 4-5 Comparison of the Finite Element Modal Analysis and Ground Vibration Test Mode Frequencies

	MODE 1			**MODE 2**			**MODE 3**		
	FEM [Hz]	**GVT [Hz]**	**Diff. (%)**	**FEM [Hz]**	**GVT [Hz]**	**Diff. (%)**	**FEM [Hz]**	**GVT [Hz]**	**Diff. (%)**
1	1.07	1.01	6.4	4.05	4.13	1.8	6.33	5.86	8.1
2	1.04	1.00	4.4	3.78	3.95	4.4	6.56	6.21	5.6
3	1.15	1.22	5.5	4.19	4.42	5.2	13.06	12.22	6.8
4	1.18	1.22	3.1	4.36	4.52	3.5	9.27	8.27	12.1
5	1.79	1.70	5.5	5.49	5.46	0.5	10.27	9.81	4.7
6	2.65	2.87	7.7	9.70	8.85	9.6	14.25	13.98	2.0
7	1.74	1.78	2.4	5.11	5.34	4.3	12.47	12.45	0.2
8	2.65	2.95	10.1	14.99	15.21	1.4	17.33	18.56	6.6

The comparison of the mode shapes, on the other hand, is made by calculating the Modal Assurance Criteria (MAC) between the numerical and test results in FEMtools© by using the below equation

$$MAC_{rs} = \left(\frac{[\{\varphi\}_r^T \{\varphi\}_s]^2}{[\{\varphi\}_r^T \{\varphi\}_r][\{\varphi\}_s^T \{\varphi\}_s]} \right) \times 100$$

where,

$\{\varphi\}_r$: numerical modal vector
$\{\varphi\}_r^T$: transpose of $\{\varphi\}_r$
$\{\varphi\}_s$: test modal vector
$\{\varphi\}_s^T$: transpose of $\{\varphi\}_s$

100% of MAC represents the perfect correlation whereas 0% means no correlation. For practical purposes, minimum 80% of MAC value has to be satisfied [63], [64].

MAC values are tabulated in Table 4-6. As it is observed in the comparisons tables, the ground vibration test and finite element modal analysis results are highly correlated. Especially the MAC values reveal that the numerical and experimental mode shapes are almost the same. The differences between the mode frequencies are mostly under the 10 %.

Table 4-6 Modal Assurance Criteria between Finite Element Modal Analysis and Ground Vibration Test Mode Shapes

	Mode 1 (%)	**Mode 2 (%)**	**Mode 3 (%)**
1	97.3	99.1	98.4
2	97.2	99.2	97.9
3	97.6	99.0	99.0
4	97.9	97.7	99.3
5	99.0	99.2	98.5
6	99.4	96.9	95.7
7	98.8	98.4	99.3
8	99.5	92.8	97.7

According to several flutter analysis, the mode that triggers the flutter is the torsional mode of the structure. Therefore, high difference in torsional mode frequencies of the finite element modal analysis and the ground vibration test may cause incorrect estimation of the flutter onset speed. In this regard, the difference in torsional mode frequencies of configuration-6, which is 9.6 %, draws attention. When the flutter analysis and test results of configuration-6 given in Chapter 5.2.4.1 and Chapter 5.3.2, respectively, are compared, it is concluded that the analysis cannot find the conservative flutter speed and the possible reason is the difference in the numerical and the experimental torsional mode frequencies.

Since the torsional mode frequency differences for other configurations are lower and their flutter analysis results are on conservative side and compatible with the flutter test results, only the FE model of the configuration-6 is decided to be modal updated in order to resolve the mismatch.

4.4.2. Modal Updating Parameters and Responses

To update the model firstly the parameters to be updated and responses to be tuned have to be determined. In the stage of preparation of the FE model, 14 CBUSH elements were already created with assumed stiffness values as it is mentioned in

Chapter 4.2.1. These stiffness values in 6 axes for 14 spring elements were selected as being 84 parameters in modal updating. As responses, the mode frequencies and shapes were chosen.

The elastic modulus and the density of the aluminum were also tried as parameter in updating since there are always uncertainties in manufacturing process and the material properties utilized may not match the real aluminum alloy used in present study. However, they were not sufficient to update the model due to the limited interval defined. Therefore, ultimately only CBUSH stiffnesses were set as parameter in the modal updating.

4.4.3. Modal Updating Results

After modal updating, the torsional mode frequency converges to the test result by 0.1% difference and MAC values rise little bit. The results are shown on Table 4-7.

Table 4-7 Configuration-6 Modal Updating Results

	Mode 1	**Mode 2**	**Mode 3**
Frequency [Hz]	2.65	8.86	14.18
MAC (%)	99.4	97.0	96.0

CHAPTER 5

FLUTTER SUBSTANTIATION

5.1. General Introduction

This chapter is dedicated to give all the details of the studies executed for the flutter substantiation of the wing-like structure with different payload configurations. In the section of 5.2, the flutter analysis results are presented acquired with both the updated and the non-updated FE models. The section 5.3 introduces the wind tunnel flutter tests conducted to validate the numerical flutter simulations.

5.2. Flutter Analysis

In this section flutter analysis results of each configuration were given. The aerodynamic models belonging to 8 different configurations were prepared in ZAERO©. The modal data extracted from MSC Nastran© as *.f06 files including mode frequencies and corresponding mode shapes were provided to ZAERO© in order to perform frequency domain flutter analysis by splining it with the aerodynamic panel model.

5.2.1. Aerodynamic Model

Aerodynamic models of all configurations were created with CAERO7 and BODY7 bulk data cards which are utilized to define aerodynamic, i.e. lifting, wing and body macro elements in ZAERO© respectively. Per the type of the components, which bulk data card is used to build its aerodynamic panel model and the number of panels belonging to each component are given on Table 5-1. As an example, the aerodynamic model of the configuration-1 is shown in Figure 5-1.

Table 5-1 Aerodynamic Model Information

Type of Component	Bulk Data Card	Number of Panels
Wing	CAERO7	200
Pylon		20
Wood Fixture		900
Wing Fixture		20
Payload	BODY7	450

5.2.2. Spline of the Aerodynamic and Structural Models

ZAERO© establishes the displacement and force transferal between both finite element model and aerodynamic model by the spline module. It creates a spline matrix as a transfer function working between two models during the flutter analysis. Per the type of component, there are different spline bulk data cards that can be used. For the components which are not elastically modelled in the FEM, for instance, SPLINE0 card, which imposes zero displacement to the aerodynamic boxes, is used. Table 5-2 gives the details of the spline modelling for the wing-like structure.

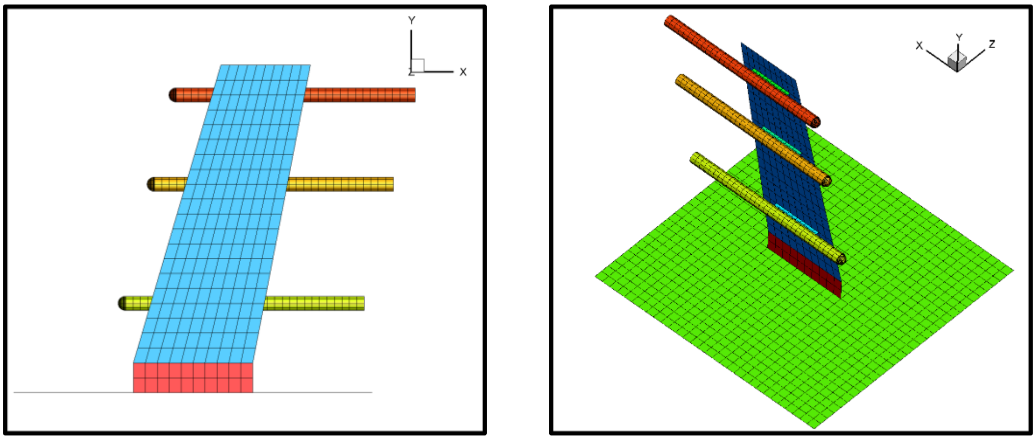

Figure 5-1 Aerodynamic Model of Configuration-1

Table 5-2 Spline Modelling Details

Type of Component	Bulk Data Card
Wing	SPLINE1
Pylon	
Wing Fixture	
Wood Fixture	SPLINE0
Payload	SPLINE3

Due to the misspecified parameters in spline cards, the spline module sometimes does not work properly, which may influence the flutter results implicitly. It can be checked via the PLTMDOE bulk data card which is utilized for drawing the interpolated structural modes on the aerodynamic model. If the mode shapes seem to be correct, then it means that the spline module functions properly. As an example, the first three mode shapes of the configuration-1 in its aerodynamic model are given on Figure 5-2, Figure 5-3 and Figure 5-4, respectively.

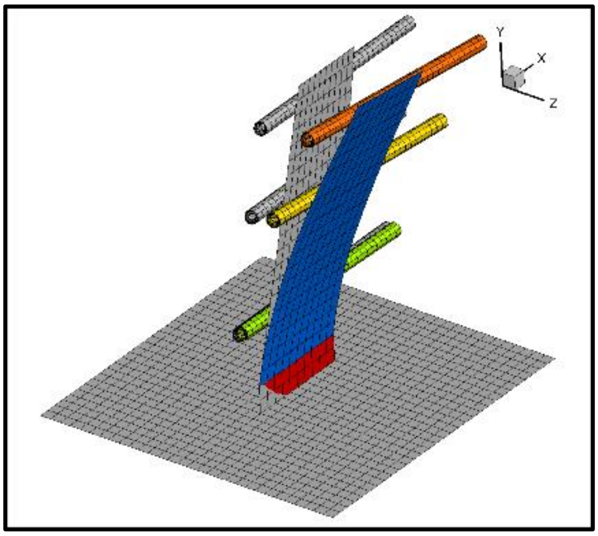

Figure 5-2 Interpolated 1st Bending Mode Shapes on Aerodynamic Panel Model

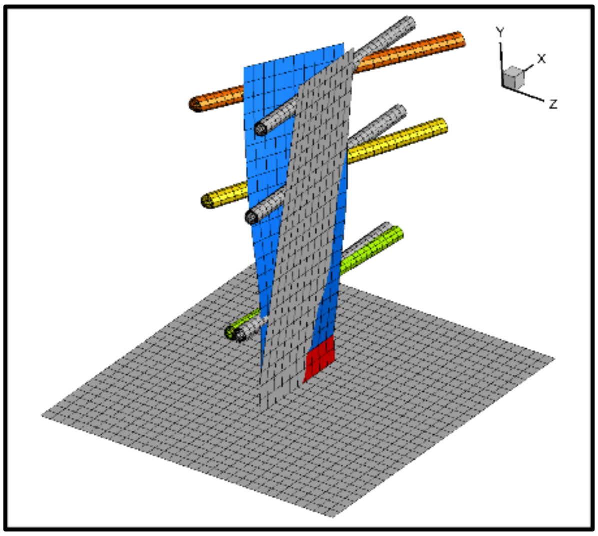

Figure 5-3 Interpolated Torsion Mode Shapes on Aerodynamic Panel Model

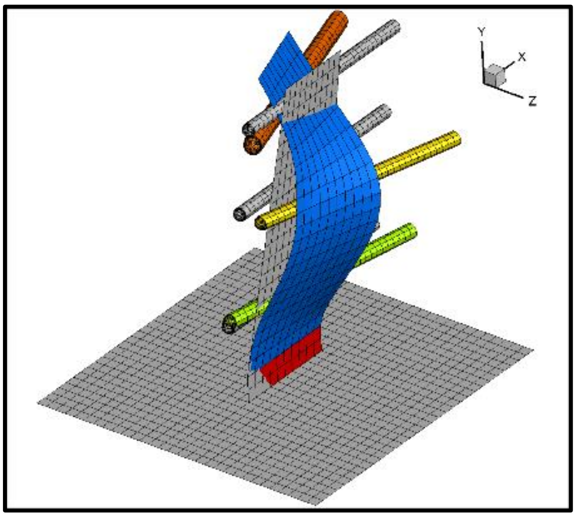

Figure 5-4 Interpolated 2nd Bending Mode Shapes on Aerodynamic Panel Model

5.2.3. Flutter Analysis Parameters and Solution Method

In the ZAERO© input file, there are essentially three bulk data cards related to the flutter solution. First one is the MKAEROZ card in which the Mach number and reduced frequencies are specified. The card creates all the M-k pairs with which the AIC matrix is realized. It is important to note that the Mach number specified in this card is only utilized for computing the compressibility effects in the flutter equation of motion. For all configurations, the Mach number is iterated by hand per the resulting flutter onset speeds. Reduced frequencies, on the other hand, are selected between 0.00 and 0.26 at the intervals of 0.02.

The second one is the FIXMDEN card in which the air density and velocities to be swept during the solution are determined. Since there are several velocities as opposed to one Mach number in the solution, the solution method is called as non-matched point flutter analysis. There is FIXHATM card that can be used for the matched point flutter analysis with varying Mach numbers. However, it is computationally costly since it creates AIC matrices for each Mach number. For all configurations, the velocities are adjusted according to the initial flutter analysis results. The air density is calculated as 1.06416 kg/m^3 based on the Ankara Wind Tunnel air pressure and temperature.

The last one is the FLUTTER card that triggers the solution using the parameters specified in the previous cards. The number of structural modes to be comprised in the flutter solution and the structural damping along the frequency of interest are identified here. For all configurations, the first three modes are included in the solution and zero structural damping is assumed for the purpose of obtaining conservative results. Nevertheless, ZAERO$^{©}$ gives the results as a function of assumed structural damping starting from 0 % to 4 % at the intervals of 0.5.

5.2.4. Flutter Analysis Results

Flutter analysis results with both non-updated and updated models are given in the sub chapters of 5.2.4.1 and 5.2.4.2, respectively.

5.2.4.1. Non-updated Model

For each configuration, the flutter onset speeds and the frequencies estimated by ZAERO$^{©}$ are given on Table 5-3. The results are tabulated according to two different structural damping values for each configuration; first is zero for staying on conservative side and second is the torsional mode structural damping extracted from the GVT data (see Table 4-4 Ground Vibration). Since the torsional mode of the structure generally triggers the flutter, the results are also reported at the structural damping of this particular mode acquired from the modal test. However, it is crucial to emphasize that the correct estimation of the structural damping is very difficult even if it comes from an experimental work. Therefore, the flutter results given per positive structural damping are intended for informative purposes only. As the structural damping has a positive value, while the flutter speed has a tendency to increase, the flutter frequency inclines to decrease.

Table 5-3 Flutter Analysis Results with Non-updated Model, Onset Speeds and Frequencies

	Zero Structural Damping		**Torsional Mode Structural Damping**	
	Flutter Speed [m/s]	**Flutter Frequency [Hz]**	**Flutter Speed [m/s]**	**Flutter Frequency [Hz]**
1	38.5	2.7	39.1	2.6
2	35.2	2.5	35.4	2.4
3	35.5	2.7	35.8	2.7
4	37.8	2.9	38.8	2.8
5	34.2	4.4	35.2	4.2
6	51.1	9.2	53.9	8.9
7	31.2	4.0	32.0	3.9
8	55.6	9.5	55.9	9.4

The V-g and V-f diagrams belonging to the configuration-1 are also given in Figure 5-5 and Figure 5-6, respectively. For other configurations, the diagrams are introduced in Appendix F.

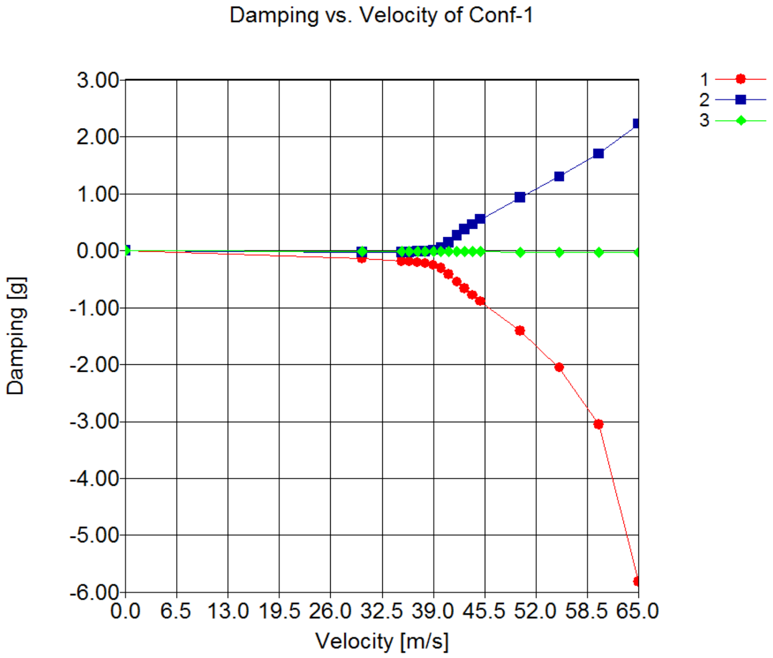

Figure 5-5 Flutter Analysis with Non-updated Model, V-g Diagram of Configuration-1

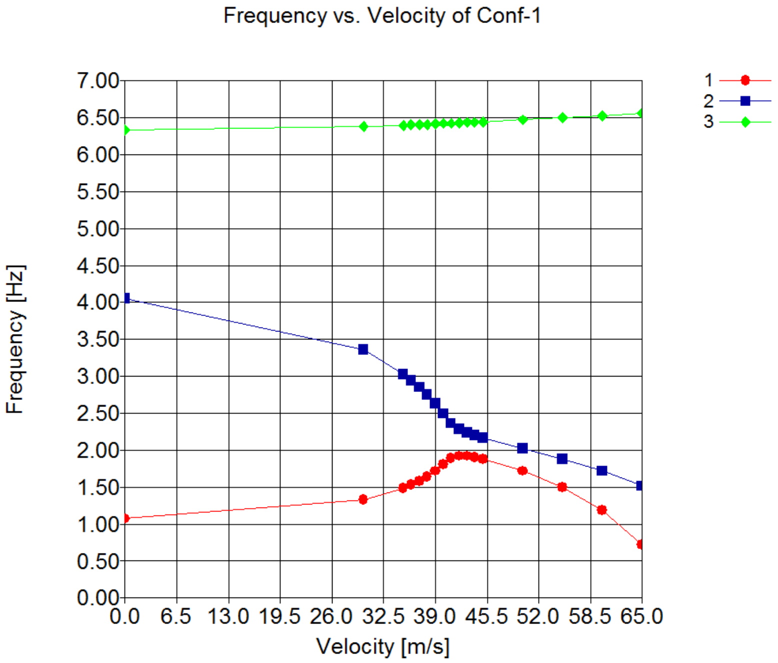

Figure 5-6 Flutter Analysis with Non-updated Model, V-f Diagram of Configuration-1

5.2.4.2. Updated Model

By using the modal output coming from the finite element modal analysis performed with the updated FE model of configuration-6, the flutter analysis is re-conducted. The flutter onset speeds and frequencies per zero and the torsional mode structural damping values are tabulated on Table 5-4. The V-g and V-f diagrams are given in Figure 5-7 and Figure 5-8, respectively.

Table 5-4 Flutter Analysis Results with Updated Model, Onset Speeds and Frequencies of Configuration-6

Zero Structural Damping		**Torsional Mode Structural Damping**	
Flutter Speed [m/s]	**Flutter Frequency [Hz]**	**Flutter Speed [m/s]**	**Flutter Frequency [Hz]**
47.5	8.4	50.5	8.2

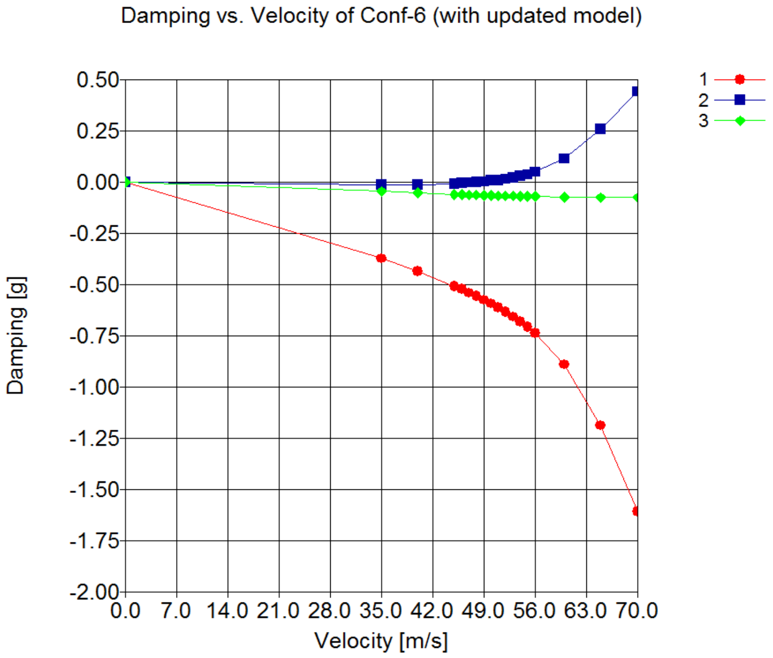

Figure 5-7 Flutter Analysis with Updated Model, V-g Diagram of Configuration-6

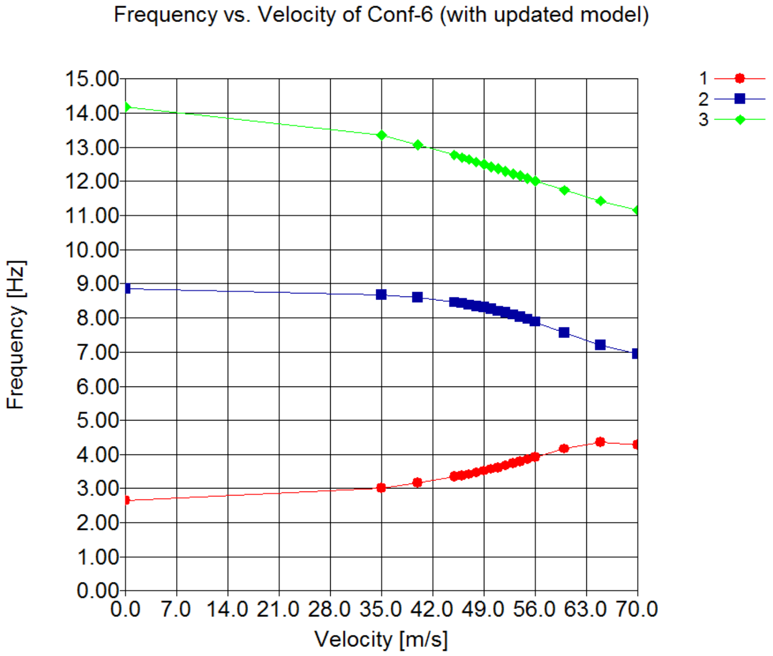

Figure 5-8 Flutter Analysis with Updated Model, V-f Diagram of Configuration-6

5.3. Wind Tunnel Flutter Test

In this section, the wind tunnel flutter tests results are summarized. Tests were carried out at the Ankara Wind Tunnel that is operated at low subsonic aerodynamic regime. The section width and height of the test room are 3.05 m and 2.44 m, respectively. Based on the tunnel characterization measurements, the turbulence intensity and non-uniformity of flow along the wind tunnel section are reported to be lower than 1 % and 1 m/s, respectively. During the tests, the strain gage data were collected with Dewesoft R4$^{©}$ data acquisition system with 5 kHz sampling frequency and then the data were processed with HBM nCode Glyphworks$^{©}$ to extract the test flutter frequencies.

5.3.1. Test Setup

The wing-like structure was integrated to the wind tunnel ground with a wooden fixture. The wooden fixture consists of one plate, two timbers and 8 metal brackets. While four of them were utilized to link the plate and two timbers, the other four fixed the assembly to the wind tunnel ground. The purpose of timbers is to lift the wooden plate and prevent the test specimen from the boundary layer generated until the flow comes to the wing-like structure.

There was one rosette type strain gage instrumented at the mid root of the wing like structure to gather 3 channels strain data while it is fluttering. The location of the strain gage was determined by observing the torsional mode shapes of the configurations, i.e. the flutter triggering mode of the structure, and considering the maximum stress location on the wing during the flutter. From time series of this data, the increase in strain amplitudes near to flutter onset speed can be observed. Furthermore, the FFT of the time series gives the flutter frequency. The general view of the configuration-1 assembly with the instrumentation details of the strain gage is shown on Figure 5-9.

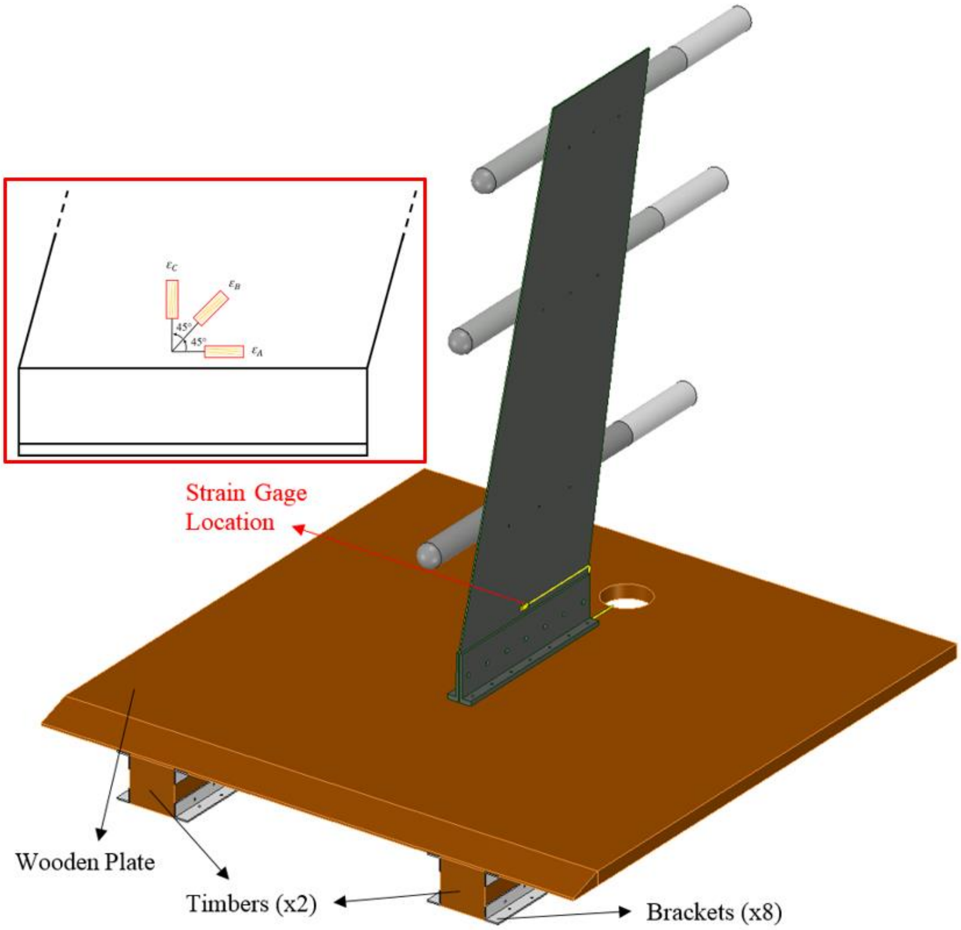

Figure 5-9 Wind Tunnel Flutter Test Model of Configuration-1

The test specimen was placed into the test room such that the wing surface is in equal distance to the right and left walls of the wind tunnel. In compatible with the modal tests and flutter analyses, there was no angle of attack and/or side slip angle adjusted in the wind tunnel model. In order not to affect the uniformity of the flow, the cable routing of the strain gage was adjusted such that it leaves the wooden plate behind the wing like structure. All surface discontinuities such as head of screws etc. were smoothened with aluminum tapes. The test setup of configuration-1 in the wind tunnel is shown in Figure 5-10.

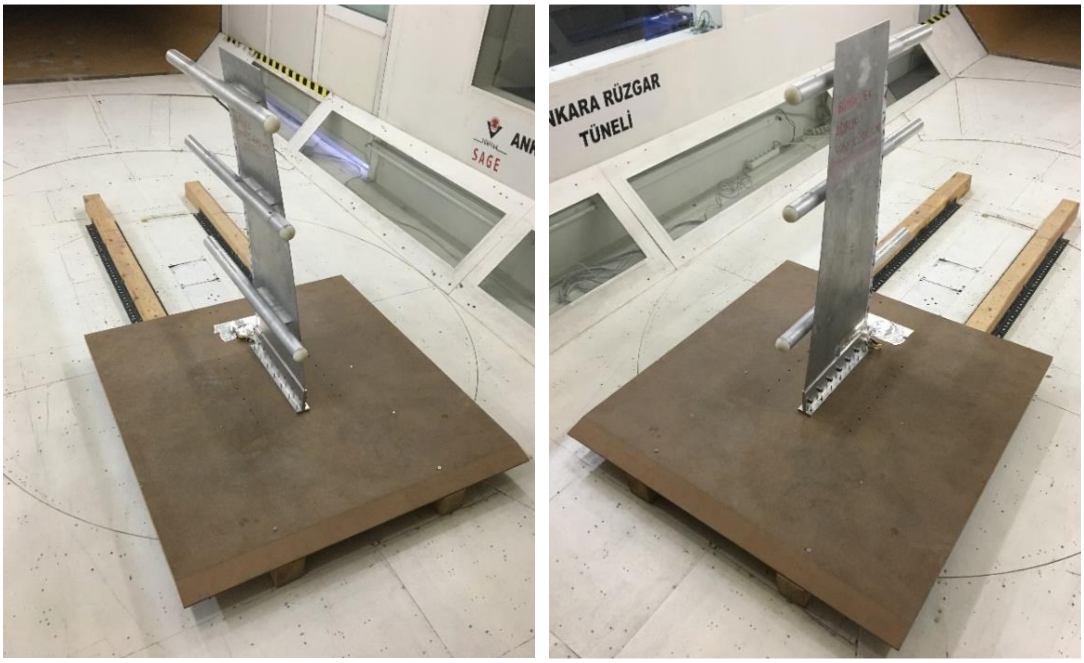

Figure 5-10 Wind Tunnel Test Setup of Configuration-1

5.3.2. Wind Tunnel Flutter Test Results

For each configuration, the wind tunnel flutter onset speeds as an interval and the flutter frequencies are summarized on Table 5-5. The flutter onset speeds were determined by observing the associated strain time history together with the wind tunnel velocity that was increased discretely, namely at intervals of 0.5 or 1 m/s. The interval in which the strain amplitudes start to rise is given as flutter speed interval. The first channel of the strain gage, i.e. ϵ_A in Figure 5-9, was used for the analysis since it gives more designative signal due to the torsional motion of the wing during the flutter. For configuration-1, the strain time history during the flutter together with the tunnel velocity and its FFT result are given in Figure 5-11 and Figure 5-12, respectively. For other configurations, the time histories and FFT results are outlined in Appendix G. It is noted that the frequency resolution used for FFT of the time data for all configurations are in the order of 10^{-3} Hz.

Table 5-5 Wind Tunnel Flutter Test Results

	Flutter Speed Interval [m/s]	Flutter Frequency [Hz]
1	(40.0, 41.0)	2.4
2	(38.0, 39.0)	2.4
3	(39.0, 40.0)	2.7
4	(40.0, 41.0)	2.8
5	(37.0, 37.5)	4.3
6	(50.5, 51.0)	8.3
7	(34.0, 35.0)	4.0
8	(60.0, 60.5)	9.5

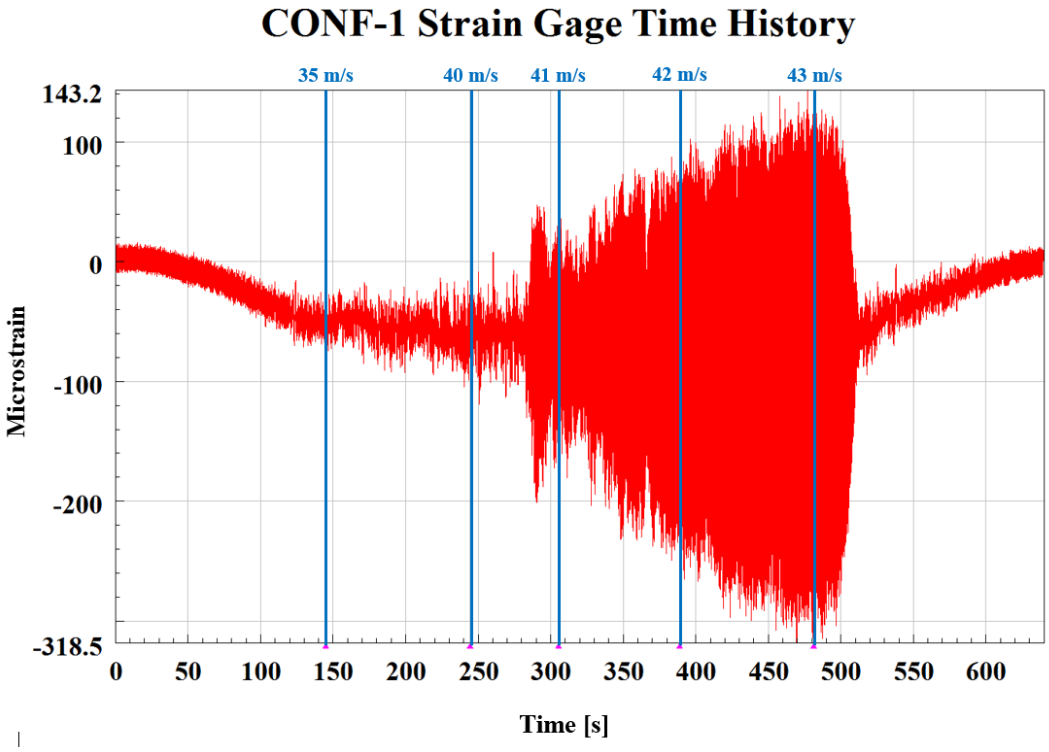

Figure 5-11 Strain Gage Time History of Configuration-1 During Flutter

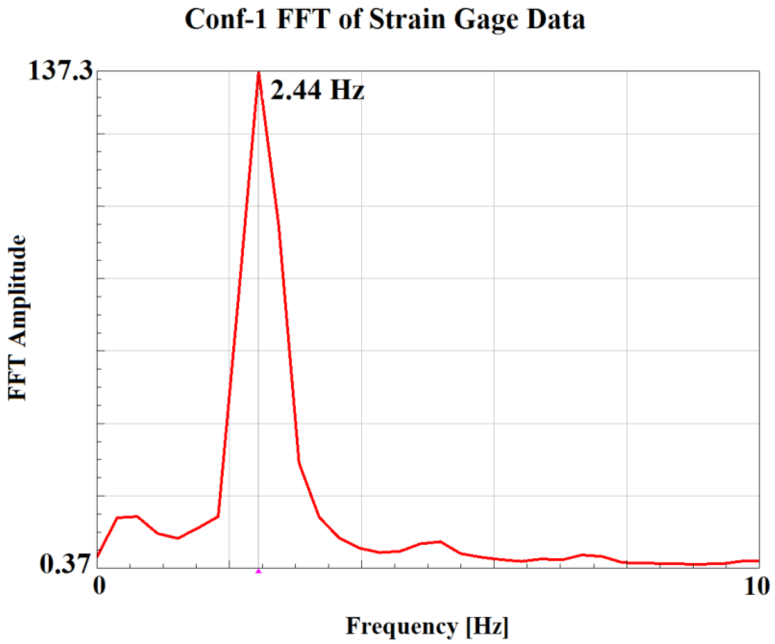

Figure 5-12 Test Flutter Frequency of Configuration-1 Acquired from FFT of Strain Gage Data

CHAPTER 6

DISCUSSION AND INFERENCES

6.1. General Introduction

This chapter is devoted to the comparisons and inferences of flutter analysis and test results. The effects of the payload configurations on the flutter characteristic of the structure are also discussed together with the rise in wing torsional rigidity provided by lengthy pylons.

6.2. Comparison of Flutter Analysis and Test Results

Table 6-1 displays the comparison of the flutter analysis and the wind tunnel test results. Analysis flutter results are given per zero structural damping to stay in conservative side. The one who may want to review the results at torsional mode structural damping can refer to Table 5-3.

Table 6-1 Comparison of the Flutter Analysis and the Wind Tunnel Test Results

	ZAERO$^{\copyright}$ Zero Structural Damping		**Wind Tunnel Test**		**Speed Difference (%)**	**Frequency Difference (%)**
	Flutter Speed [m/s]	**Flutter Frequency [Hz]**	**Flutter Speed Interval [m/s]**	**Flutter Frequency [Hz]**		
1	38.5	2.7	(40.0, 41.0)	2.4	(3.8, 6.1)	12.5
2	35.2	2.5	(38.0, 39.0)	2.4	(7.4, 9.7)	4.2
3	35.5	2.7	(39.0, 40.0)	2.7	(9.0, 11.3)	0.0
4	37.8	2.9	(40.0, 41.0)	2.8	(5.5, 7.8)	3.6
5	34.2	4.4	(37.0, 37.5)	4.3	(7.6, 8.8)	2.3
6	51.1	9.2	(50.5, 51.0)	8.3	(1.2, 0.2)	10.8
6^U	47.5	8.4			(5.9, 6.9)	1.2
7	31.2	4.0	(34.0, 35.0)	4.0	(8.2, 10.9)	0.0
8	55.6	9.5	(60.0, 60.5)	9.5	(7.3, 8.1)	0.0

6^U: Flutter analysis results with updated FE model of configuration-6

As it is observed from the table, the analysis results are in a good agreement with the wind tunnel flutter tests. The maximum difference in the flutter speed is 11.3% while it is 12.5% for the flutter frequency despite the zero structural damping assumption. For all configurations, the analysis stays in the conservative side thanks to the lower flutter speed estimation apart from the non-updated configuration-6 results. The analysis for this configuration estimates the flutter speed and frequency 0.2% and 10.8% higher, respectively compared to the test results. Even if the analysis flutter speed seems to be matched with the test result, since there must be a certain level of structural damping, the actual difference becomes higher. As it is seen in Table 5-3, the flutter speed according to the torsional mode structural damping, for instance, is 53.9 m/s that is 5.7% higher than the test flutter speed. Furthermore, the relatively high difference in the analysis and the test flutter frequency for this configuration also proves that the analysis results are unreliable. In short, the unconservative flutter estimation is not acceptable and needs to be updated. In view of the fact that the structural mode triggering the flutter is torsional mode of the structure, the difference between the numerical and the experimental torsional mode frequencies for configuration-6 may be the reason of incompatible flutter results. This required the modal updating of the FE model belonging to configuration-6 and its results are given in Chapter 4.4.3. The flutter analysis was re-performed using the modal outputs coming from the finite element modal analysis conducted with the updated FE model and it yielded highly correlated results. According to the zero structural damping assumption, the differences become 6.9% and 1.2% for the flutter onset speed and the frequency, respectively and most importantly a conservative flutter speed can be achieved.

6.3. The Effects of the Payload Configurations on the Flutter Results

In an aircraft modification project where aeroelastic certification requirements are applied, effective installation of the payloads under the lifting surface is always an issue of concern. In case of existence of two or more payloads being integrated on the wing, all the integration combinations have to be assessed from the point of flutter clearance. If there is one or more problematic payload configuration that cannot be handled, then possible design updates such that relocation of the payloads must be considered to solve the problem.

Depending on the dynamic behavior of the wing, aerodynamic design of the payloads and the type of the coupling of two, various trends can be observed among the configurations. For the cases where the wing is considerably bigger and structurally stiffer compared to the interface design of the payload(s), it is anticipated that as mass terms increase especially towards the wing tip, the flutter onset speed decreases as a result of the drop in the main structural mode frequencies of the wing. However, relatively slender and structurally too elastic wings are prone to behave sensitive against the installation of the payloads due to their comparable mass and stiffness.

The current study investigates the influences of 8 different payload configurations on the flutter characteristic of the wing-like structure. In respect of its dynamic behavior extracted by both analyses and tests, the wing like structure falls into the second class mentioned above. Since it is designed as thin-walled aluminum, it is in a tendency to show unpredictable flutter characteristics with different payload configurations.

By taking the eighth configuration as a reference, other loaded configurations are interpreted. The first eye catching result is that the flutter onset speeds for the first four configurations are very close to each other although the mass distribution are highly different. While the flutter onset speeds for first three configurations are expected to be lower due to the high mass junctions towards the wing tip, the fifth and the seventh configurations yield the earlier flutter initiation. Furthermore, it is observed that the payload closest to the wing root do not have a great influence on the flutter speed. The payload at the middle, on the other hand, seems to be the most predominant on the flutter characteristics since the configuration comprising only this payload, i.e. configuration-7, experiences the flutter at the lowest speed among others.

The possible reason of this unpredictable trend may be the pylon structures which are too long and implicitly too stiff. The section 6.4 goes into the details of the pylon effect on the flutter results and gives some supportive studies justifying asserted discourse.

6.4. The Effects of the Rigid Pylons on the Flutter Results

As aforementioned, the flutter results are highly dependent on the dynamic behavior of the structure. For all payload configurations of the wing-like structure, the torsional mode triggers the flutter and it is more reasonable to focus on the factors that may influence this mode while commenting on the flutter results. The lengthy pylon(s), for instance, is the primary factor increasing the torsional mode frequency in respect of its shape. If the stiffness added by pylons overrides the effect of mass increase due to the payload, the torsional mode frequency may go up and flutter occurs at higher speeds.

In order to reveal the pylon effect more tangibly, some further analyses and tests were performed. Their results are given in sub-sections of 6.4.1 and 6.4.2.

6.4.1. Flutter Analysis of Configuration-1 with Narrower Pylons

In order to observe whether long pylons increase the torsional frequency and the flutter onset speed, a virtual configuration was created as if three pylons are shorter, i.e. 0.0475 m, 0.0426 m and 0.0386 m, in the configuration-1 and both modal and flutter analyses were re-conducted. The modal and flutter analysis results and their comparisons with the original configuration-1 are given in Table 6-2 and Table 6-3, respectively. As it is seen from the results, both the torsional mode frequency and the flutter onset speed decrease by 12.8 % and 19.5 % respectively. These results confirm the incontrovertible effect of the stiff pylons on the flutter results.

Table 6-2 Comparison of Finite Element Modal Analysis Results of the Configuration-1 with Shorter Pylons and the Original Configuration-1

Conf. No	**Mode 1 [Hz]**	**Mode 2 [Hz]**	**Mode 3 [Hz]**
1	1.07	4.05	6.33
1^{Virtual}	1.04	3.53	5.49
Difference (%)	2.8 ↓	12.8 ↓	13.3↓

Table 6-3 Comparison of Zero Damping Flutter Analysis Results of the Configuration-1 with Narrower Pylons and the Original Configuration-1

Conf. No	**Flutter Speed [m/s]**	**Flutter Frequency [Hz]**
1	38.5	2.7
1^{Virtual}	31.0	2.6
Difference (%)	19.5 ↓	3.7↓

6.4.2. Wind Tunnel Flutter Test Results of Configuration-7 with Upper and Lower Pylons

An additional wind tunnel flutter test was also performed to verify the rigid pylon effect. After the test conducted for the original configuration-7 which experiences the flutter at the lowest speed, the upper and the lower pylons were installed on the wing without their payloads and the test was repeated. The test results and its comparison with the original configuration is given in Table 6-4. The increase in the flutter onset speed after the insertion of lower and upper pylons also validates the argument of rigid pylon effect.

Table 6-4 Comparison of Wind Tunnel Flutter Test Results of the Configuration-7 with Upper and Lower Pylons and the Original Configuration-7

Conf. No	**Flutter Speed [m/s]**	**Flutter Frequency [Hz]**
7	(34.0, 35.0)	4.0
7^{Virtual}	(37.0, 37.5)	4.3
Difference (%)	(7.1, 8.8) ↑	7.5 ↑

CHAPTER 7

CONCLUSION

7.1. General Conclusion

The first aim of this thesis is to observe the degree of accuracy of numerical flutter simulations by comparing them with tests. The second one is to follow the aeroelastic certification process dictated by independent aviation authorities for a real project and experience the possible problems.

To realize these two goals, a wing-like structure was designed in a way to experience flutter at low subsonic regime by iterating the parameters of taper ratio, location of the elastic axis and the forward sweep angle in frequency domain flutter analyses. To observe the effect of payloads on the flutter behavior of the wing, three stations were determined to install them on the structure. With the existence of three payload stations, totally 8 configurations were created.

For all configurations, finite element modal analyses were performed to extract the natural frequencies and the mode shapes of the wing-like structure to be utilized in the frequency domain flutter simulations. These modal outputs were correlated with the results of ground vibration tests. The finite element model of the configuration-6 was updated with its GVT results due to the difference in the torsional mode frequencies between the finite element modal analysis and the ground vibration test. The flutter analyses were conducted in order to find flutter onset speeds and frequencies. Eventually, all flutter simulation outputs were verified with the wind tunnel flutter tests.

The finite element modal analysis results were in a good agreement with the modal test results apart from the configuration-6. The difference in the experimental and the numerical torsional mode frequencies was obtained as 9.6 % for this configuration and it was evaluated as risky for the flutter simulation. To solve the problem, the finite element model of the configuration-6 was updated by iterating the boundary condition stiffness values in a way to converge the test results. Eventually the torsional mode frequency was obtained by 0.1 % difference.

The flutter analysis results also conformed to the tests except the non-updated configuration-6. In parallel with the reasonable doubts, the flutter analysis performed with non-updated finite element model yielded unconservative flutter onset speed. On the contrary, with the updated model the problem was circumvented, and a conservative flutter onset speed could be acquired.

Different combinations of payload installations did not show a predictable tendency in aeroelastic manner. The reason was the lengthy pylons that solidifies the wing-like structure, increases the torsional frequency and influences the flutter results.

Referring to the experience gained in this study, it is concluded that experiments are vital and inevitable activities in an aeroelastic certification. Even if there is a very simple structure whose flutter model can be easily achieved, the unexpected results can only be obviated by tests.

7.2. Recommendations for Future Works

Within the scope of this thesis, the aeroelastic certification process was simulated including the finite element modal analyses, ground vibration tests, modal updating activities, flutter analyses and wind tunnel flutter tests. Utilizing a simple wing-like structure, these studies were completed in a short period of time. However, in projects with a real aircraft, it takes long time only to create an equivalent finite element model that is easy to run, extracts comparable modal results and is updatable if necessary. Even if it is prepared, performing aircraft level ground vibration test and updating the model per the modal test results may be a difficult process.

To expedite the procedure, there are two options which can be endeavored in ZAERO$^{©}$. The first one is to utilize the GVT results as *.unv file directly in the frequency domain flutter analysis. This can eliminate the necessity of finite element model preparation, performing finite element modal analysis and modal updating activities. This option is very helpful especially for the cases lack of the model data of the aircraft. The second one is the new capability that has been added to ZAERO© recently. It is the bulk data card of GVT2FEM which allows the use of ground vibration test data for aeroelastic analyses. The difference of this card from the previous option is that it requires the finite element model since it maps the mode shapes measured by GVT on the FEM grids directly. Although this option is not efficient in comparison with the first one, it can still eliminate the modal updating step of the process.

Apart from the different methodologies that can be tried with the same wing-like structure, an expressive improvement will be to design more complicated wing which has an appropriate airfoil section, real structural elements such as ribs and stringers and control surfaces. The more structural elements and internal connections mean the more compelling dynamic model generation and different troubles that have to be handled. Since this type of a lifting surface is hard to experience flutter at the low subsonic regime due to its high rigidity, the problem becomes difficult also in terms of the aerodynamic calculations with the inclusion of compressibility effects. Furthermore, the effects of control surfaces on the flutter characteristics can be investigated focusing on the various parameters such as center of gravity, moments and products of inertia of the control surfaces.

REFERENCES

[1] "Leonardo Da Vinc's Dream of Flying." [Online]. Available: https://www.leonardodavinci.net/flyingmachine.jsp. [Accessed: 14-May-2019].

[2] "Joseph-Michel and Jacques-Étienne Montgolfier," 2018. [Online]. Available: https://www.britannica.com/biography/Montgolfier-brothers. [Accessed: 14-May-2019].

[3] "Airship," 2018. [Online]. Available: https://www.britannica.com/technology/airship. [Accessed: 14-May-2019].

[4] T. C. Parramore, "Airplane, First Flight og," *Encyclopedia of North Carolina*. University of North Carolina Press, 2006.

[5] D. Hodges, G. Pierce, and M. Cutchins, *Introduction to Structural Dynamics and Aeroelasticity*, vol. 56, no. 3. 2003.

[6] I. E. Garrick and W. H. Reed III, "Historical Development of Aircraft Flutter," *J. Aircr.*, vol. 18, no. 11, pp. 897–912, 1981.

[7] M. W. McFarland, *The Papers of Wilbur and Orville Wright*. New York: McGraw-Hill, 1953.

[8] G. T. R. Hill, "Advances in Aircraft Structural Design," *Anglo-American Aeronaut. Conf.*, 1951.

[9] F. W. Lanchester, "Torsional Vibrations of the Tail of an Aeroplane," *ARC R&M*, vol. Part 1, 1916.

[10] L. Bairstow and A. Fage, "Oscillations of the Tail Plane and Body of an Aeroplane," *ARC R&M*, vol. Part 2, 1916.

[11] "Handley Page Type O Twin-Engine Heavy Bomber Biplane Aircraft." [Online]. Available: https://www.militaryfactory.com/aircraft/detail.asp?aircraft_id=454. [Accessed: 14-May-2019].

[12] "Albatros D-III Biplane Fighter." [Online]. Available: http://www.aviastar.org/air/germany/albatros_d-3.php. [Accessed: 14-May-2019].

[13] "The Evolution of Modern Aircraft, Part I Chapter II." [Online]. Available: https://history.nasa.gov/SP-468/ch2-2.htm. [Accessed: 15-May-2019].

[14] A. G. von Baumhauer and C. Koning, "On the Stability of Oscillations of an

Airplane Wing," *Int. Air Congr. London*, 1923.

[15] W. Birnbaum, "Das Ebene Problem des Schlagenden Flügels (The Plane Problem of the Oscillating Wing)," *ZAMM*, vol. 4, pp. 277–292, 1924.

[16] A. F. Zahm and R. M. Bear, "A Study of Wing Flutter," *NACA Rept. 285*, 1926.

[17] M. Rauscher, "Uber die Schwingungen freitragen der Flügel (On the Flutter of a Wing)," *Luftfahrtforschung*, vol. 4, pp. 94–106, 1929.

[18] "Report on Puss Moth Accidents," 1936.

[19] H. R. Cox and A. G. Pugsley, "Theory of Loss of Lateral Control Due to Wing Twisting," *R&M 1506*, 1932.

[20] W. J. Duncan and G. A. McMillan, "Reversal of Aileron Control Due to Wing Twist," *R&M 1499*, 1932.

[21] T. Theodorsen, "General Theory of Aerodynamic Instability and the Mechanism of Flutter," *NACA Rept. 496*, 1935.

[22] T. Theodorsen and I. E. Garrick, "Mechanism of Flutter - A Theoretical and Experimental Investigation of the Flutter Problem," *NACA TR-685*, 1940.

[23] B. von Schlippe, "Zur Frage der selbsterregten Flügelschwingungen," *Luftfahrtforschung*, vol. 13, 1936.

[24] R. A. Frazer, W. J. Duncan, and A. R. Collar, *Elementary Matrices*. Cambridge: Cambridge University Press, 1938.

[25] S. J. Loring, "Outline of General Approach to the Flutter Problem," *Soc. Autom. Eng. J.*, pp. 345–356, 1941.

[26] L. Prandtl, "Wing Theory in a Compressible Medium," *Luftfahrtforschung*, vol. 13, pp. 313–319, 1936.

[27] B. Smilg and L. S. Wasserman, "Application of Three Dimensional Flutter Theory to Aircraft Structures," *Air Corps Tech. Rept. 4798*, 1942.

[28] H. Hall, "A Record of Information on Oscillatory Aerodynamic Derivative Measurements," *R&M 3232*, 1962.

[29] J. B. Bratt, K. C. Wight, and V. J. Tilly, "The Application of the 'Wattmeter' Harmonic Analyser to the Measurement of Aerodynamic Damping for Pitching Oscillations," *R&M 2063*, 1942.

[30] L. S. Wasserman and W. S. Mykytow, "Model Construction," *AGARD Man. Aeroelasticity*, vol. 4, 1961.

[31] A. L. Erickson and J. D. Stephenson, "Transonic Flutter of Control Surfaces," *NACA RM No. F30*, 1947.

[32] G. Temple and H. A. Jahn, “Flutter at Supersonic Speeds,” *R&M 2140,* 1945.

[33] S. von Borbely, “Aerodynamic Forces on a Harmonically Oscillating Wing at Supersonic Speed,” *Zeitschrift für Angew. Math. und Mech.*, vol. 22, pp. 190–205, 1942.

[34] I. E. Garrick and S. I. Rubinow, “Flutter and Oscillating Air Force Calculations for an Airfoil in a Two Dimensional Supersonic Flow,” *NACA Rept. 846,* 1946.

[35] “A Survey and Evaluation of Flutter Research and Engineering,” 1956.

[36] U.S. Department of Trasnport Federal Aviation Administration, “Overview — Title 14 of the Code of Federal Regulations (14 CFR),” 2013.

[37] “MIL-A-8870A (USAF),” 1987.

[38] J. G. Barmby, H. J. Cunningham, and I. E. Garrick, “Study of Effects of Sweep on the Flutter of Cantilever Wings,” *Natl. Advis. Comm. Aeronaut. Rept. 1014,* 1951.

[39] W. J. Bursnall, “Initial Flutter Tests in the Langley Transonic Blowdown Tunnel and Comparison with Free-Flight Flutter Results,” *Natl. Advis. Comm. Aeronaut. RM L52K14,* 1953.

[40] R. Herrera and R. H. Barnes, “An Experimental Investigation of the Flutter of Several Wings of Varying Aspect Ratio, Density, and Thickness Ratio at Mach Numbers from 0.60 to 1.10,” *Natl. Advis. Comm. Aeronaut. RM A54A29,* 1954.

[41] W. G. Molyneux, “The Flutter of Swept and Unswept Wings with Fixed-Root Conditions,” *Minist. Supply, Aeronaut. Res. Counc. Reports Memo. R&M 2796,* 1954.

[42] W. J. Tuovila and J. L. Mccarty, “Experimental Flutter Results for Cantilever-Wing Models at Mach Numbers Up To 3.0,” *NACA RM L55E11*, 1955.

[43] E. C. Yates, “Calculation of Flutter Characteristics for Finite-Span Swept or Unswept Wings at Subsonic and Supersonic Speeds by a Modified Strip Analysis,” *NACA RM L57L10,* 1958.

[44] S. J. Pollock, L. J. Sotomayer, L. J. Huttsell, and D. E. Cooley, “Evaluation of Methods for Prediction and Prevention of Wing/Store Flutter,” *AIAA Dyn. Spec. Conf.*, vol. 19, pp. 492–498, 1981.

[45] E. C. Yates, “AGARD Standard Aeroelastic Configurations for Dynamic Response I-Wing 445.6,” *AGARD Rept. No 765,* 1985.

[46] P. C. Chen, “Damping Perturbation Method for Flutter Solution: The g-Method,” *AIAA J.*, vol. 38, no. 9, pp. 1519–1524, 2000.

[47] R. Samikkannu and A. R. Upadhya, “Wind Tunnel Flutter Testing of

Composite T-Tail Model of a Transport Aircraft with Fuselage Flexibility," *Wind Tunnels Exp. Fluid Dyn. Res.*, 2011.

[48] W. Libo, S. Long, C. Lei, Z. Wu, and C. Yang, "Design and Analysis of a Wind Tunnel Test Model System for Gust Alleviation of Aeroelastic Aircraft," *AIAA J.*, 2012.

[49] M. B. Dalmış, "Flutter Characteristics of Plate Like Structures," Middle East Technical University, 2014.

[50] M. W. Kehoe, "A Historical Overview of Flight Flutter Testing," *NASA TM 4720*, 1995.

[51] J. Cooper, R. Lind, and J. Wright, "Aeroelastic Testing and Certification," *Encycl. Aerosp. Eng.*, pp. 1–12, 2010.

[52] J. R. Wirght and J. E. Cooper, *Introduction to Aircraft Aeroelasticity and Loads*, Second. John Wiley & Sons, Ltd, 2015.

[53] Ü. Gülçat, *Fundamentals of Modern Unsteady Aerodynamics*, Second. Istanbul: Springer, 2016.

[54] R. L. Bisplinghoff, H. Ashley, and R. L. Halfman, *Aeroelasticity*. Dover Publications, 1996.

[55] "ZAERO Theoretical Manual vs. 9.2," *ZONA Technology, Inc.* ZONA Technology, Inc., Scottsdale, AZ, 2018.

[56] "ZAERO User's Manual vs. 9.2," *ZONA Technology, Inc.* ZONA Technology, Inc., Scottsdale, AZ, 2018.

[57] C. A. Irwin and P. R. Guyett, "The Subcritical Response and Flutter of a Swept Wing Model," *R. Aircr. Establ. TR 65187*, 1965.

[58] H. J. Hassig, "An Approximate True Damping Solution of the Flutter Equation by Determinant Iteration," *J. Aircr.*, vol. 8, no. 11, 1971.

[59] "Metallic Materials Properties Development and Standardization (MMPDS)." Federal Aviation Administration, 2013.

[60] D. Cloutier and P. Avitabile, "SHAKER / STINGER EFFECTS ON MEASURED FREQUENCY RESPONSE FUNCTIONS," *IMAC 27*, pp. 1–7.

[61] J. Lau *et al.*, "Ground Vibration Testing Master Class : modern testing and analysis concepts applied to an F-16 aircraft," no. April 2014, 2011.

[62] M. N. Ensan and V. Wickramasinghe, "Methodology for Ground and Flight Vibration Testing of Light Aircraft," no. September 2015, 2014.

[63] K. Ersoy, M. Atasoy, and C. Genc, "Modal Updating of Tail of a Military Helicopter," *IMAC 34*, vol. 9, 2016.

[64] Ö. Serin, K. Ersoy, and C. Genç, “Flutter Analysis of a Wing-Like Structure with Payloads Utilizing Finite Element and Ground Vibration Test Modes,” *AIAC 2017*, 2017.

APPENDICES

A. Finite Element Models

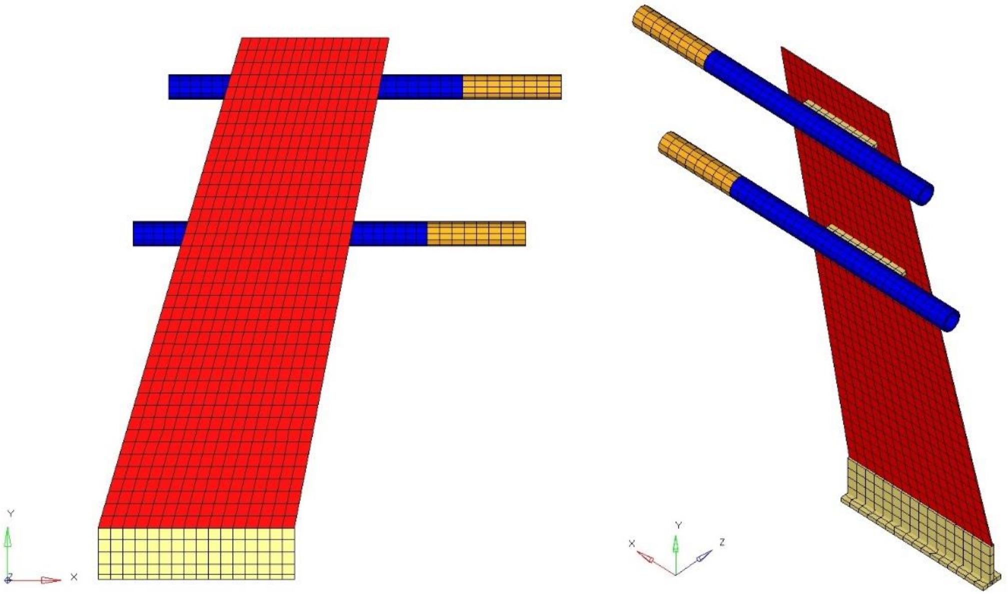

Figure 0-1 Finite Element Model of Configuration-2

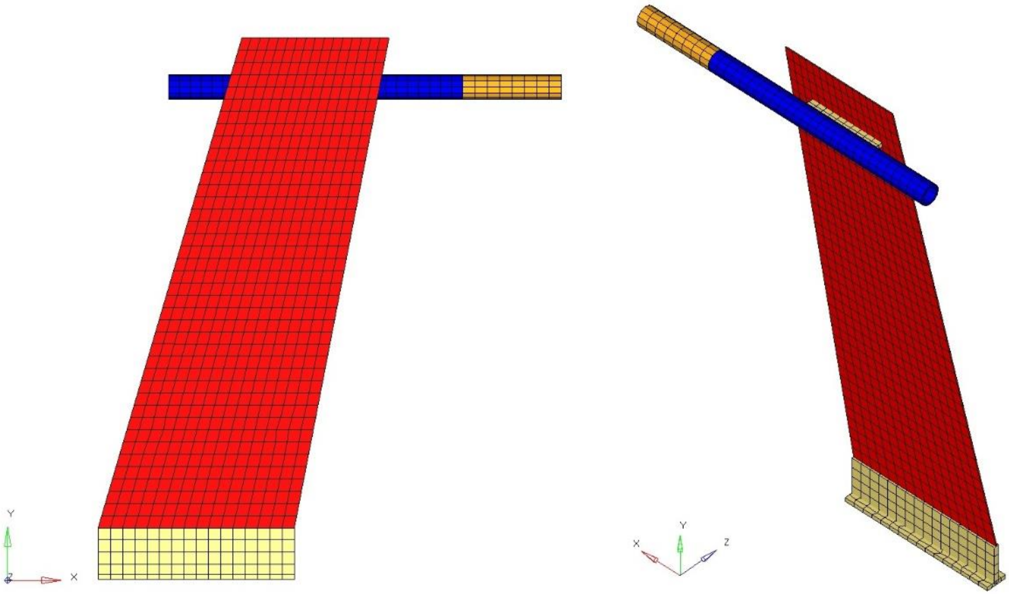

Figure 0-2 Finite Element Model of Configuration-3

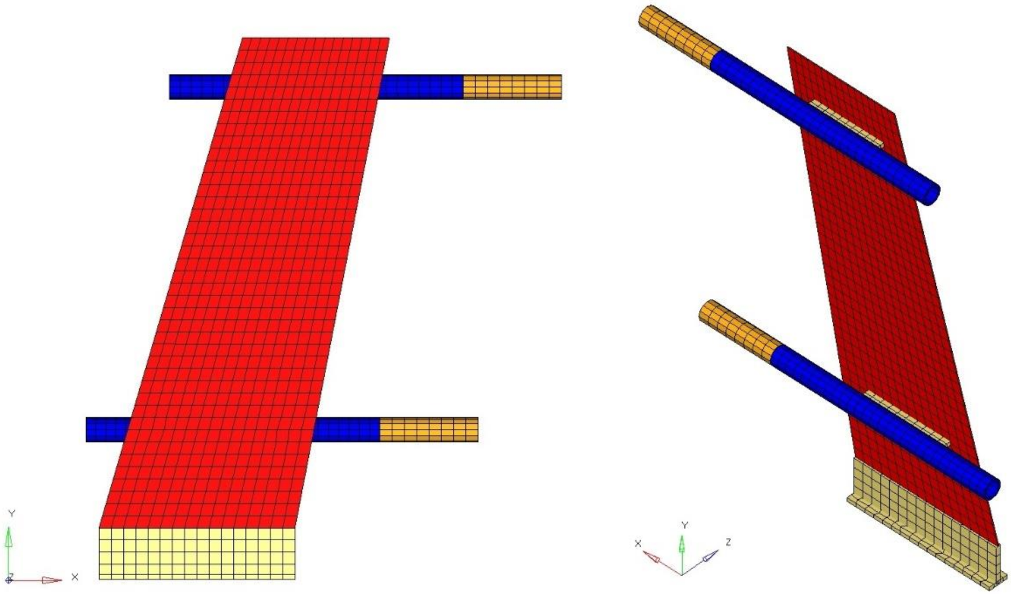

Figure 0-3 Finite Element Model of Configuration-4

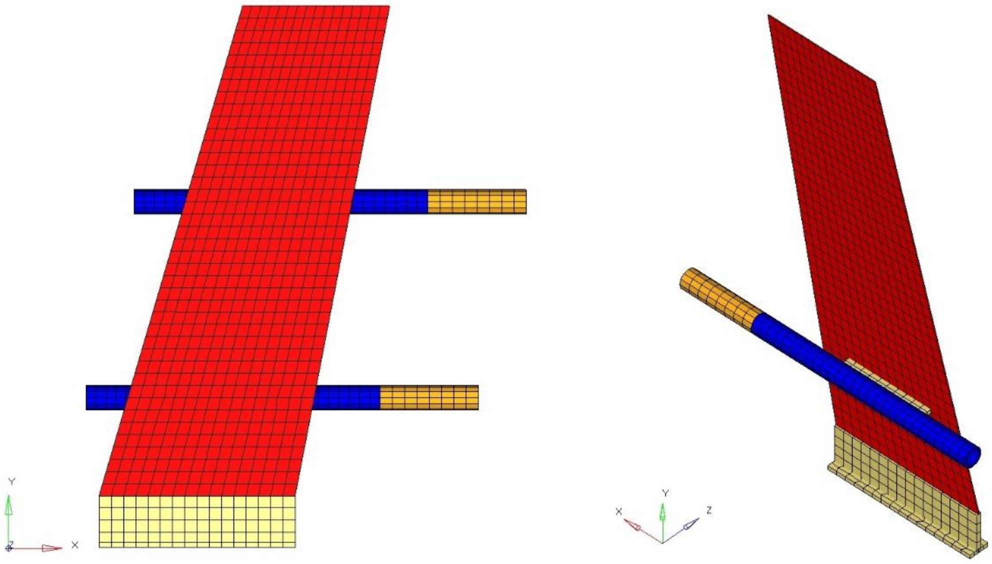

Figure 0-4 Finite Element Model of Configuration-5

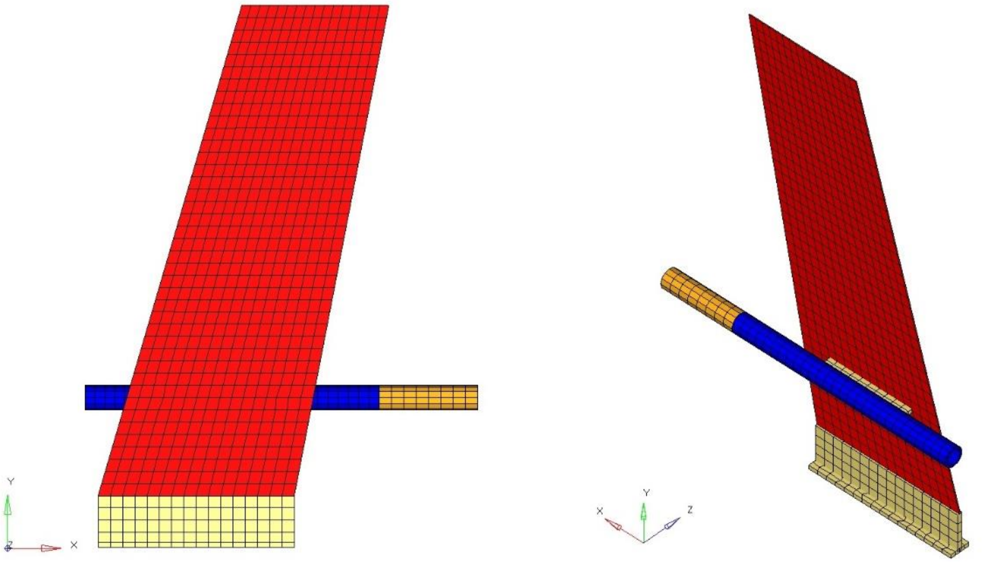

Figure 0-5 Finite Element Model of Configuration-6

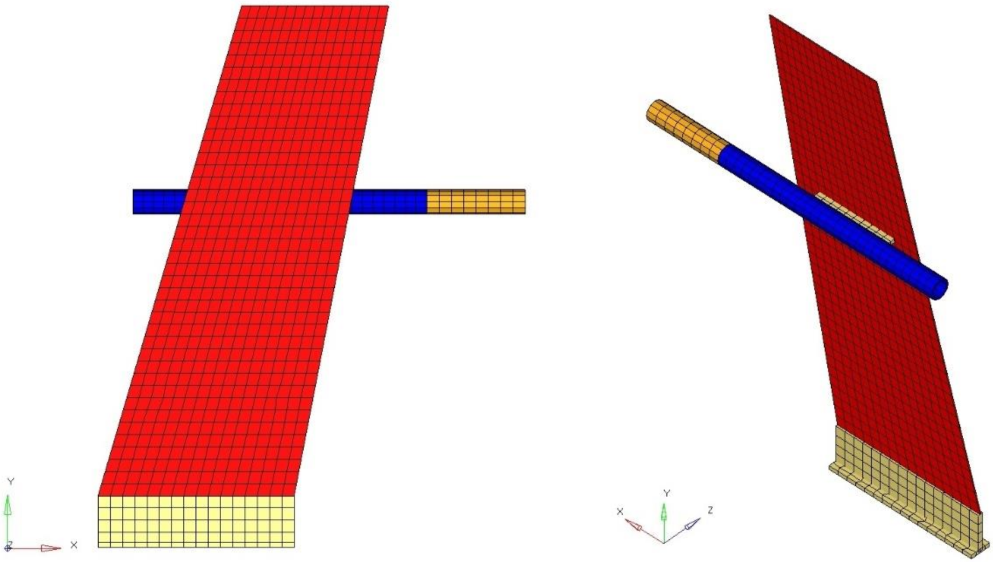

Figure 0-6 Finite Element Model of Configuration-7

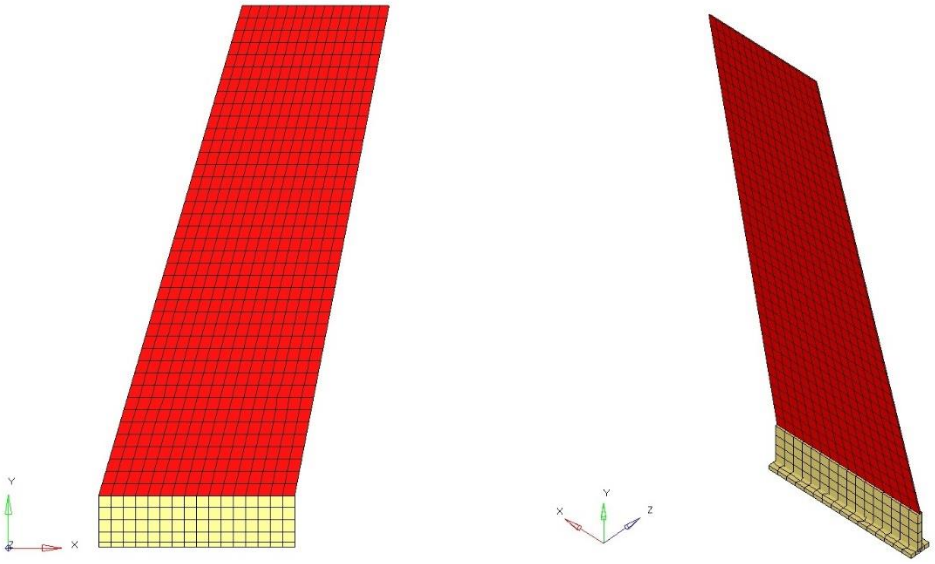

Figure 0-7 Finite Element Model of Configuration-8

B. Mesh Convergence Study with Configuration-1

In order to observe the effect of mesh density on the finite element modal analysis results, three different FE models were created as shown in Figure 0-8, Figure 0-9 and Figure 0-10, respectively. Table 0-1 indicates that all the mesh densities gives similar results and the second one was chosen to be used for the present study.

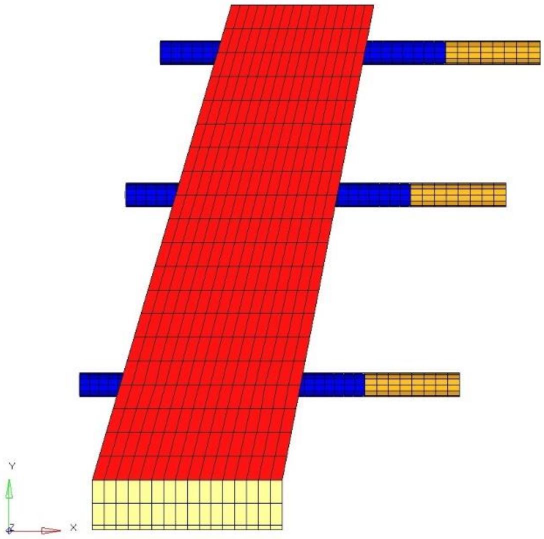

# of Grid Points	3308
# of Elements	2797
# of Degrees of Freedom	15480
# of Non-zero Stiffness Terms	489816

Figure 0-8 Finite Element Model with Mesh Density 1

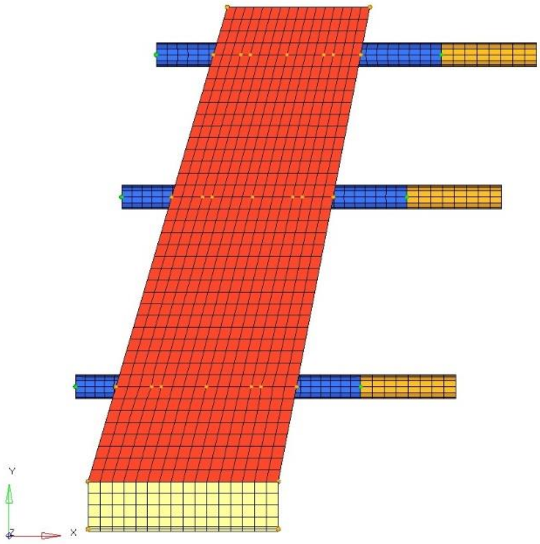

# of Grid Points	3682
# of Elements	3149
# of Degrees of Freedom	17724
# of Non-zero Stiffness Terms	549150

Figure 0-9 Finite Element Model with Mesh Density 2

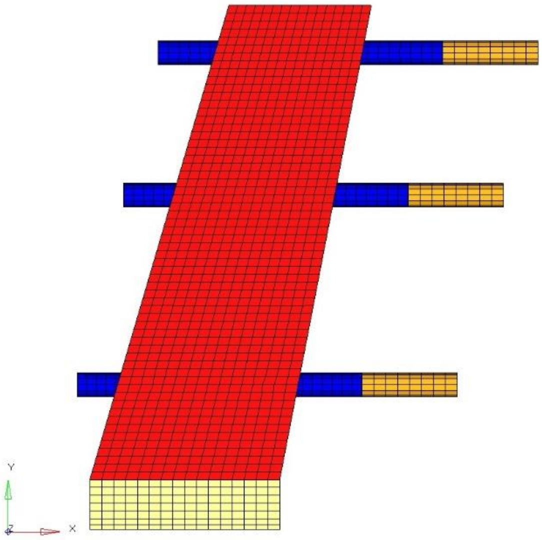

# of Grid Points	4056
# of Elements	3501
# of Degrees of Freedom	19968
# of Non-zero Stiffness Terms	608484

Figure 0-10 Finite Element Model with Mesh Density 3

Table 0-1 Finite Element Modal Analysis Results According to Different Mesh Densities

	Frequency [Hz]		
Mode #	**Mesh Density 1**	**Mesh Density 2**	**Mesh Density 3**
1	1.07	1.07	1.07
2	4.04	4.05	4.05
3	6.33	6.33	6.34

C. The Mass Effect of Transducers on Finite Element Modal Analysis Result

The masses of the accelerometers and the impedance head utilized in the GVT (see Figure 4-6) were modelled as concentrated mass elements, i.e. CONM2, in FEM and their effect on the finite element modal analysis results were examined. Table 0-2 shows that the masses of the transducers do not affect the analysis result. The specification of mechanical impedance sensor and triaxial ICP accelerometer are given in Figure 0-11 and Figure 0-12, respectively.

Table 0-2 Finite Element Modal Analysis Results with and without Transducers

	Frequency [Hz]	
Mode #	**Without Transducer Masses**	**With Transducer Masses**
1	1.07	1.07
2	4.05	4.04
3	6.33	6.33

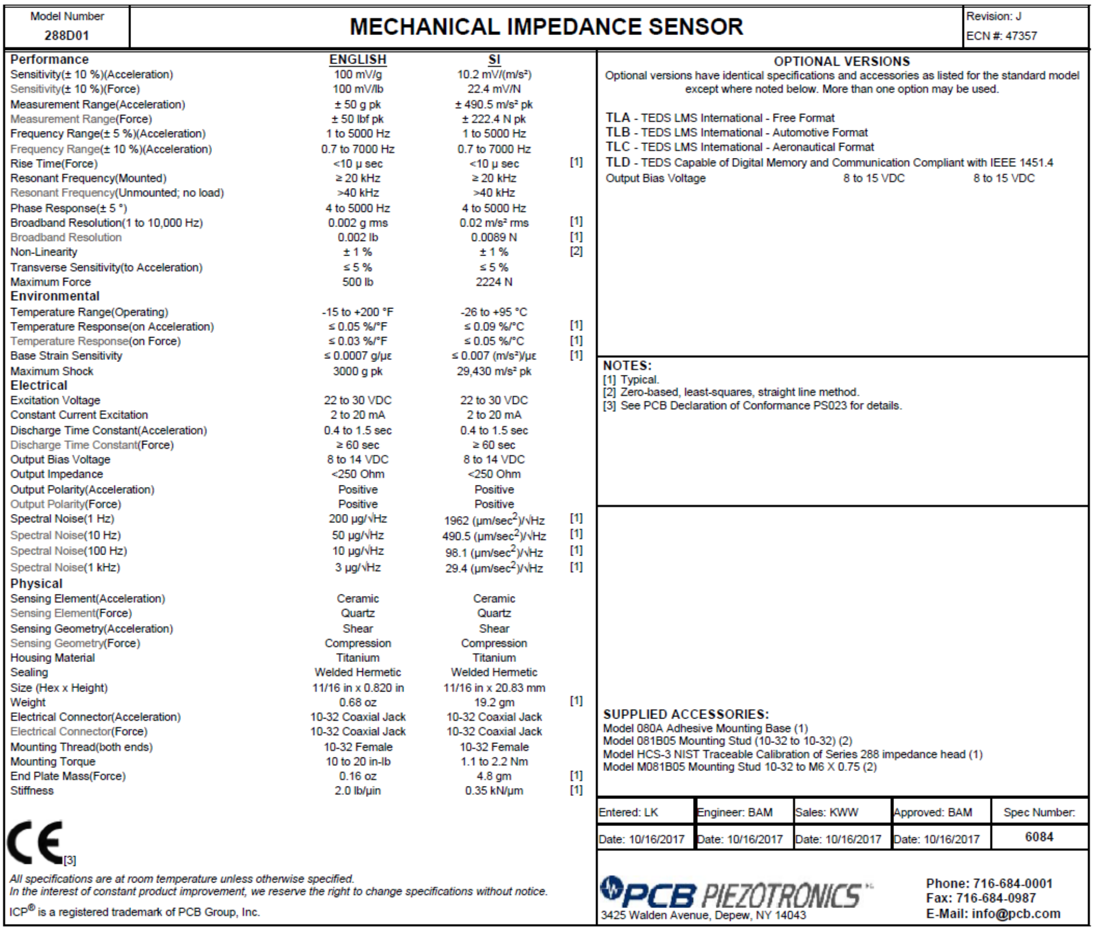

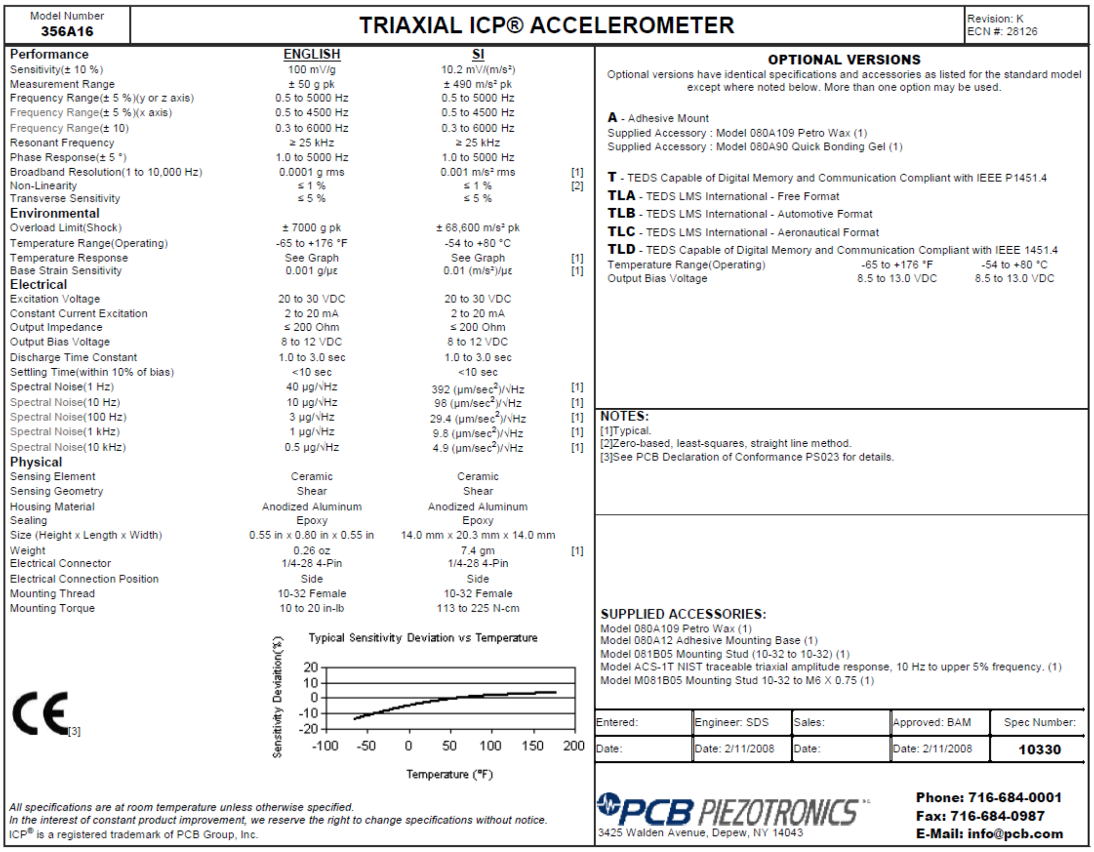
Typical Sensitivity Deviation vs Temperature
Sensitivity Deviaition(%)
20
10
0
-10
-20
-100
-50
0
50
100
150
200
Temperature (°F)

Model Number
356A16

TRIAXIAL ICP® ACCELEROMETER

Revision: K
ECN #: 28126

Performance	**ENGLISH**	**SI**	
Sensitivity(± 10 %)	100 mV/g	10.2 mV/(m/s²)	
Measurement Range	± 50 g pk	± 490 m/s² pk	
Frequency Range(± 5 %)(y or z axis)	0.5 to 5000 Hz	0.5 to 5000 Hz	
Frequency Range(± 5 %)(x axis)	0.5 to 4500 Hz	0.5 to 4500 Hz	
Frequency Range(± 10)	0.3 to 6000 Hz	0.3 to 6000 Hz	
Resonant Frequency	≥ 25 kHz	≥ 25 kHz	
Phase Response(± 5 °)	1.0 to 5000 Hz	1.0 to 5000 Hz	
Broadband Resolution(1 to 10,000 Hz)	0.0001 g rms	0.001 m/s² rms	[1]
Non-Linearity	≤ 1 %	≤ 1 %	[2]
Transverse Sensitivity	≤ 5 %	≤ 5 %	
Environmental			
Overload Limit(Shock)	± 7000 g pk	± 68,600 m/s² pk	
Temperature Range(Operating)	-65 to +176 °F	-54 to +80 °C	
Temperature Response	See Graph	See Graph	[1]
Base Strain Sensitivity	0.001 g/με	0.01 (m/s²)/με	[1]
Electrical			
Excitation Voltage	20 to 30 VDC	20 to 30 VDC	
Constant Current Excitation	2 to 20 mA	2 to 20 mA	
Output Impedance	≤ 200 Ohm	≤ 200 Ohm	
Output Bias Voltage	8 to 12 VDC	8 to 12 VDC	
Discharge Time Constant	1.0 to 3.0 sec	1.0 to 3.0 sec	
Settling Time(within 10% of bias)	<10 sec	<10 sec	
Spectral Noise(1 Hz)	40 μg/√Hz	392 (μm/sec^2)/√Hz	[1]
Spectral Noise(10 Hz)	10 μg/√Hz	98 (μm/sec^2)/√Hz	[1]
Spectral Noise(100 Hz)	3 μg/√Hz	29.4 (μm/sec^2)/√Hz	[1]
Spectral Noise(1 kHz)	1 μg/√Hz	9.8 (μm/sec^2)/√Hz	[1]
Spectral Noise(10 kHz)	0.5 μg/√Hz	4.9 (μm/sec^2)/√Hz	[1]
Physical			
Sensing Element	Ceramic	Ceramic	
Sensing Geometry	Shear	Shear	
Housing Material	Anodized Aluminum	Anodized Aluminum	
Sealing	Epoxy	Epoxy	
Size (Height x Length x Width)	0.55 in x 0.80 in x 0.55 in	14.0 mm x 20.3 mm x 14.0 mm	
Weight	0.26 oz	7.4 gm	[1]
Electrical Connector	1/4-28 4-Pin	1/4-28 4-Pin	
Electrical Connection Position	Side	Side	
Mounting Thread	10-32 Female	10-32 Female	
Mounting Torque	10 to 20 in-lb	113 to 225 N-cm	

CE[3]

All specifications are at room temperature unless otherwise specified.
In the interest of constant product improvement, we reserve the right to change specifications without notice.
ICP® is a registered trademark of PCB Group, Inc.

OPTIONAL VERSIONS

Optional versions have identical specifications and accessories as listed for the standard model except where noted below. More than one option may be used.

A - Adhesive Mount
Supplied Accessory : Model 080A109 Petro Wax (1)
Supplied Accessory : Model 080A90 Quick Bonding Gel (1)

T - TEDS Capable of Digital Memory and Communication Compliant with IEEE P1451.4
TLA - TEDS LMS International - Free Format
TLB - TEDS LMS International - Automotive Format
TLC - TEDS LMS International - Aeronautical Format
TLD - TEDS Capable of Digital Memory and Communication Compliant with IEEE 1451.4

Temperature Range(Operating)	-65 to +176 °F	-54 to +80 °C
Output Bias Voltage	8.5 to 13.0 VDC	8.5 to 13.0 VDC

NOTES:
[1]Typical.
[2]Zero-based, least-squares, straight line method.
[3]See PCB Declaration of Conformance PS023 for details.

SUPPLIED ACCESSORIES:
Model 080A109 Petro Wax (1)
Model 080A12 Adhesive Mounting Base (1)
Model 081B05 Mounting Stud (10-32 to 10-32) (1)
Model ACS-1T NIST traceable triaxial amplitude response, 10 Hz to upper 5% frequency. (1)
Model M081B05 Mounting Stud 10-32 to M6 X 0.75 (1)

Entered:	Engineer: SDS	Sales:	Approved: BAM	Spec Number:
Date:	Date: 2/11/2008	Date:	Date: 2/11/2008	**10330**

PCB PIEZOTRONICS
3425 Walden Avenue, Depew, NY 14043

Phone: 716-684-0001
Fax: 716-684-0987
E-Mail: info@pcb.com

Figure 0-12 PCB Piezotronics, Model 356A16, Triaxial ICP Accelerometer

D. Finite Element Modal Analysis Mode Shapes

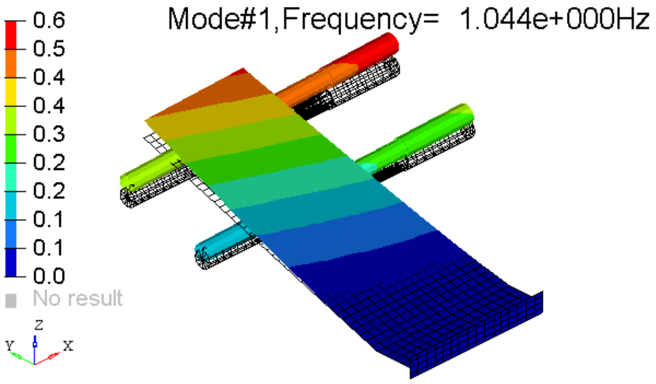
Mode#1,Frequency= 1.044e+000Hz
0.6
0.5
0.4
0.4
0.3
0.2
0.2
0.1
0.1
0.0
No result
Z
Y
X

Figure 0-13 Analysis 1st Bending Mode Shape of Configuration-2

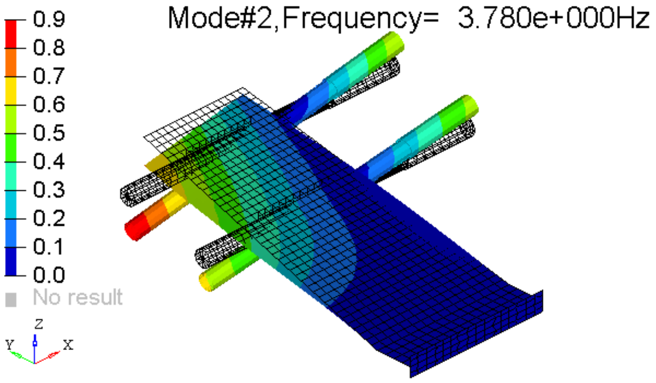
Mode#2,Frequency= 3.780e+000Hz
0.9
0.8
0.7
0.6
0.5
0.4
0.3
0.2
0.1
0.0
No result
Z
Y
X

Figure 0-14 Analysis Torsional Mode Shape of Configuration-2

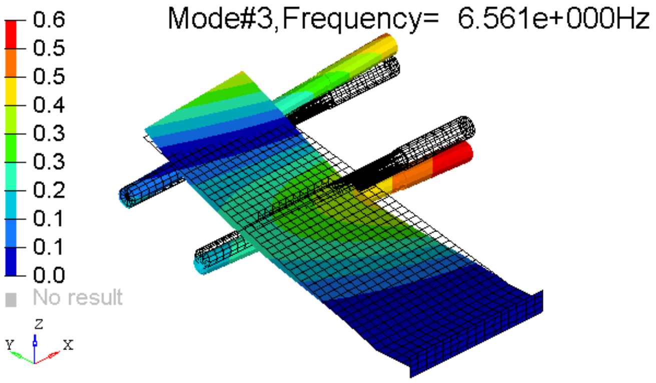
Mode#3,Frequency= 6.561e+000Hz
0.6
0.5
0.5
0.4
0.3
0.3
0.2
0.1
0.1
0.0
No result
Z
Y
X

Figure 0-15 Analysis 2nd Bending Mode Shape of Configuration-2

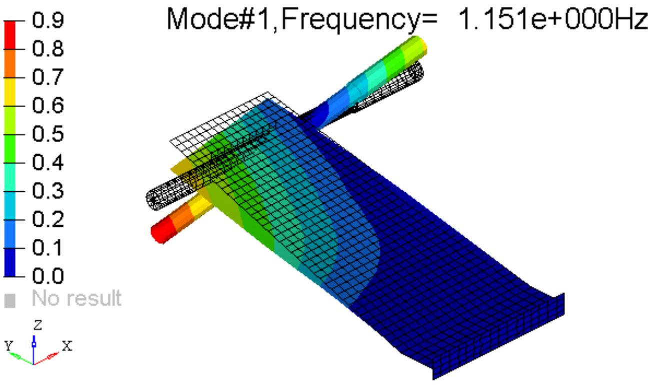
Mode#1,Frequency= 1.151e+000Hz
0.9
0.8
0.7
0.6
0.5
0.4
0.3
0.2
0.1
0.0
No result
Z
Y
X

Figure 0-16 Analysis 1st Bending Mode Shape of Configuration-3

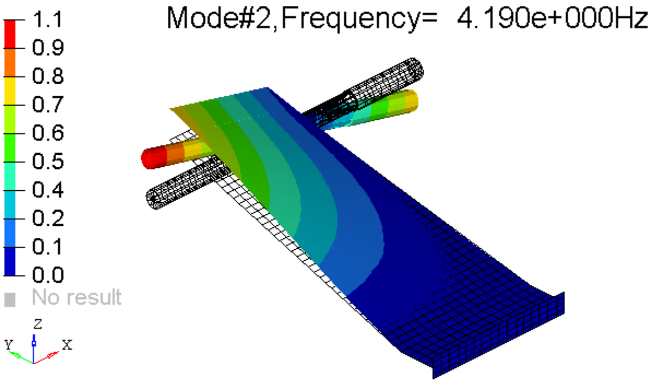
Mode#2,Frequency= 4.190e+000Hz
1.1
0.9
0.8
0.7
0.6
0.5
0.4
0.2
0.1
0.0
No result
Z
Y
X

Figure 0-17 Analysis Torsion Mode Shape of Configuration-3

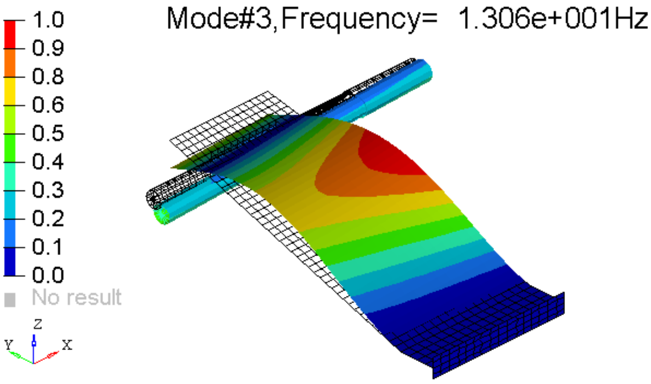
Mode#3,Frequency= 1.306e+001Hz
1.0
0.9
0.8
0.6
0.5
0.4
0.3
0.2
0.1
0.0
No result
Z
Y
X

Figure 0-18 Analysis 2nd Bending Mode Shape of Configuration-3

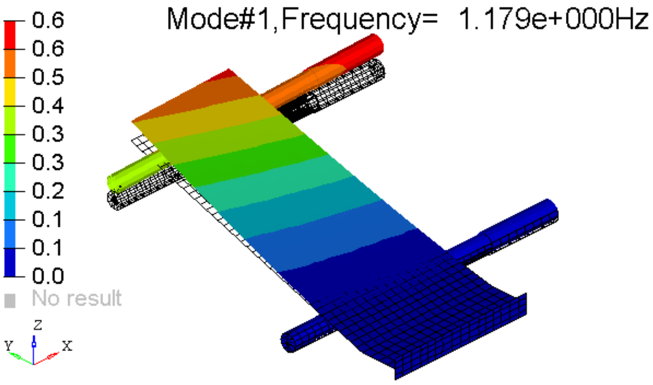
0.6
0.6
0.5
0.4
0.3
0.3
0.2
0.1
0.1
0.0
No result
Z
Y
X
Mode#1,Frequency= 1.179e+000Hz

Figure 0-19 Analysis 1st Bending Mode Shape of Configuration-4

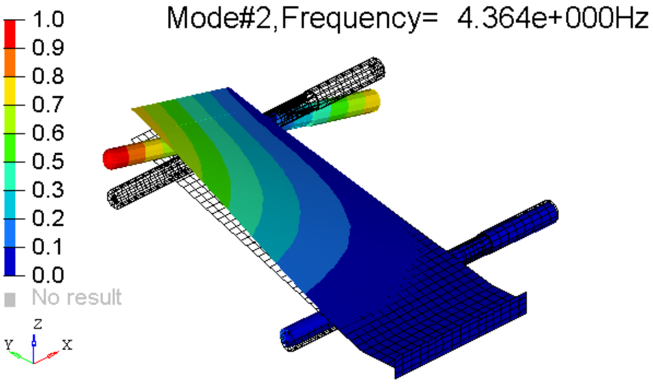
1.0
0.9
0.8
0.7
0.6
0.5
0.3
0.2
0.1
0.0
No result
Z
Y
X
Mode#2,Frequency= 4.364e+000Hz

Figure 0-20 Analysis Torsion Mode Shape of Configuration-4

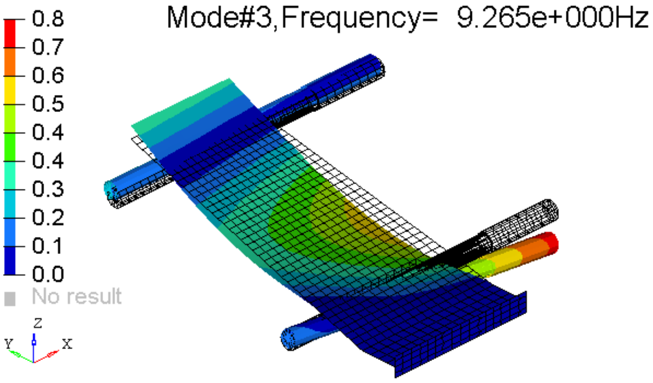
0.8
0.7
0.6
0.5
0.4
0.4
0.3
0.2
0.1
0.0
No result
Z
Y
X
Mode#3,Frequency= 9.265e+000Hz

Figure 0-21 Analysis 2nd Bending Mode Shape of Configuration-4

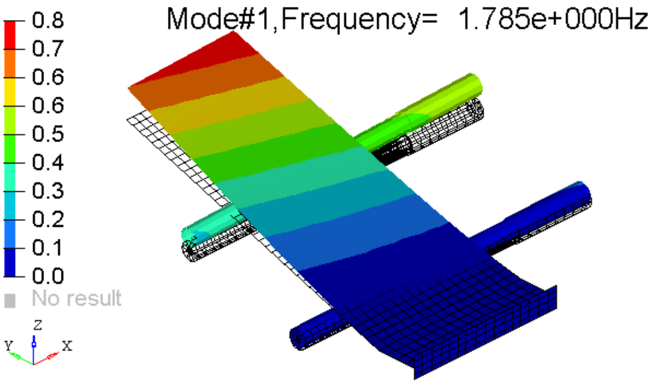
0.8
0.7
0.6
0.6
0.5
0.4
0.3
0.2
0.1
0.0
No result
Mode#1,Frequency= 1.785e+000Hz
Z
Y
X

Figure 0-22 Analysis 1st Bending Mode Shape of Configuration-5

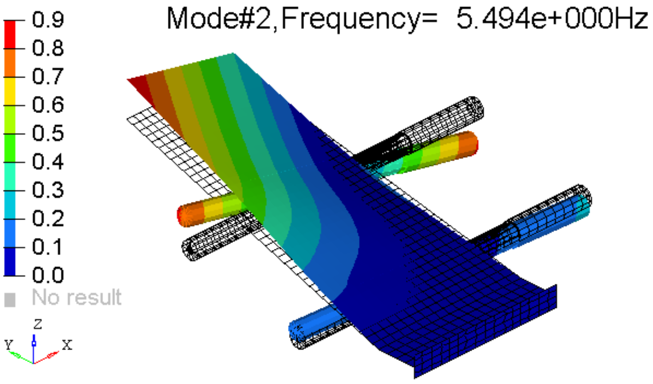
0.9
0.8
0.7
0.6
0.5
0.4
0.3
0.2
0.1
0.0
No result
Mode#2,Frequency= 5.494e+000Hz
Z
Y
X

Figure 0-23 Analysis Torsion Mode Shape of Configuration-5

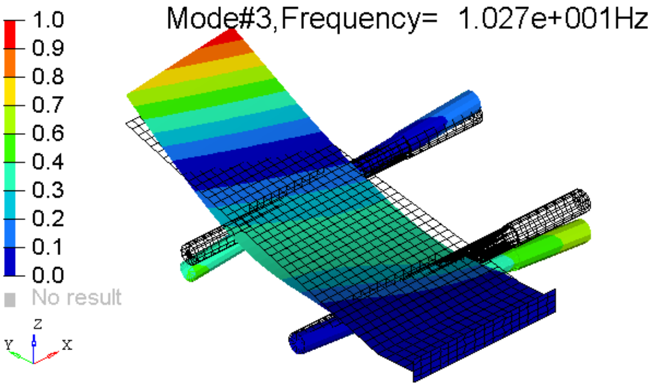
1.0
0.9
0.8
0.7
0.6
0.4
0.3
0.2
0.1
0.0
No result
Mode#3,Frequency= 1.027e+001Hz
Z
Y
X

Figure 0-24 Analysis 2nd Bending Mode Shape of Configuration-5

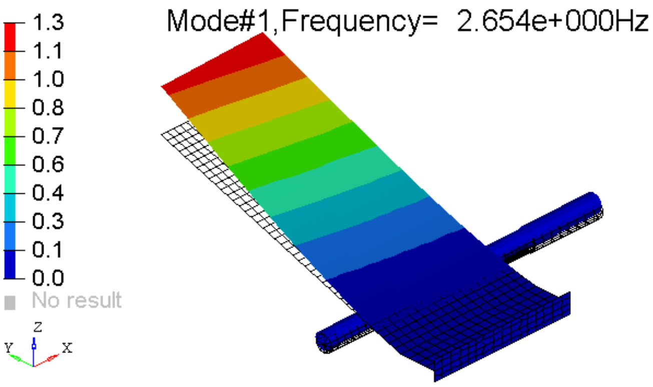
Mode#1,Frequency= 2.654e+000Hz
1.3
1.1
1.0
0.8
0.7
0.6
0.4
0.3
0.1
0.0
No result
Z
Y
X

Figure 0-25 Analysis 1st Bending Mode Shape of Configuration-6

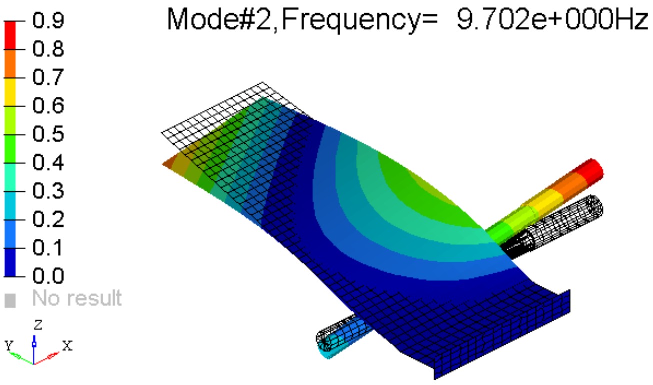
Mode#2,Frequency= 9.702e+000Hz
0.9
0.8
0.7
0.6
0.5
0.4
0.3
0.2
0.1
0.0
No result
Z
Y
X

Figure 0-26 Analysis Torsion Mode Shape of Configuration-6

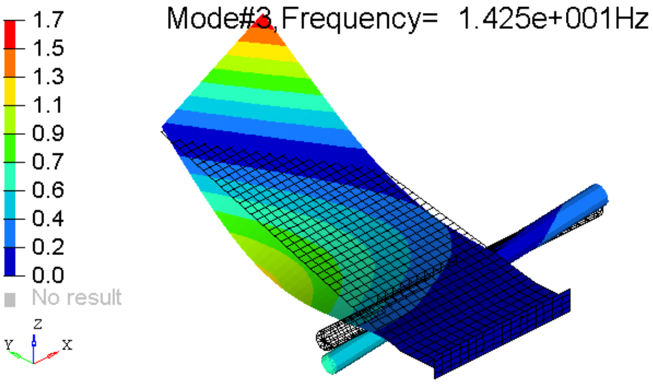
Mode#3,Frequency= 1.425e+001Hz
1.7
1.5
1.3
1.1
0.9
0.7
0.6
0.4
0.2
0.0
No result
Z
Y
X

Figure 0-27 Analysis 2nd Bending Mode Shape of Configuration-6

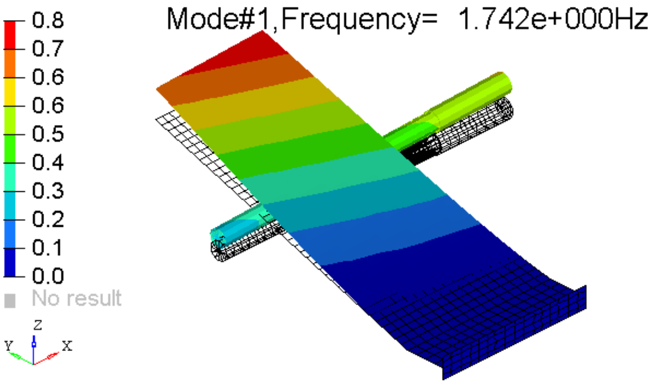
Mode#1,Frequency= 1.742e+000Hz
0.8
0.7
0.6
0.6
0.5
0.4
0.3
0.2
0.1
0.0
No result
Z
Y
X

Figure 0-28 Analysis 1st Bending Mode Shape of Configuration-7

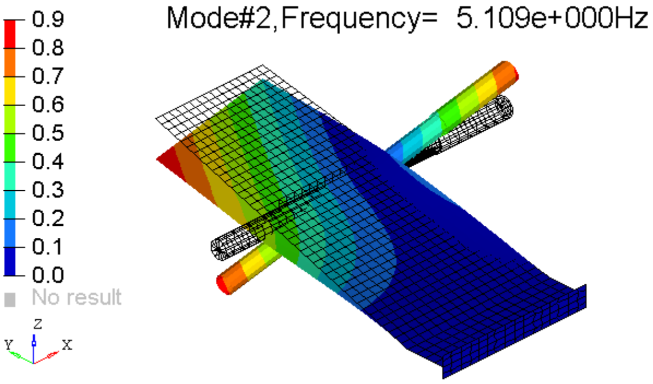
Mode#2,Frequency= 5.109e+000Hz
0.9
0.8
0.7
0.6
0.5
0.4
0.3
0.2
0.1
0.0
No result
Z
Y
X

Figure 0-29 Analysis Torsion Mode Shape of Configuration-7

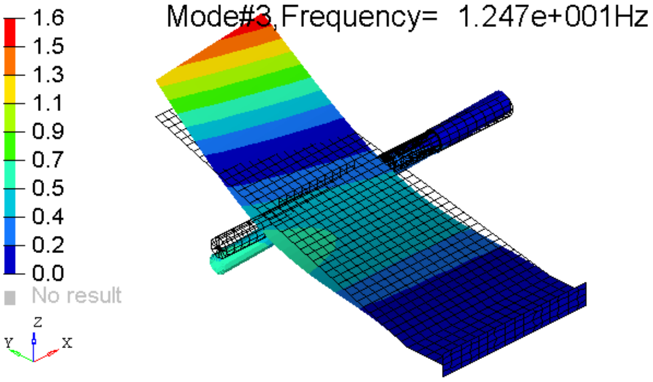
Mode#3,Frequency= 1.247e+001Hz
1.6
1.5
1.3
1.1
0.9
0.7
0.5
0.4
0.2
0.0
No result
Z
Y
X

Figure 0-30 Analysis 2nd Bending Mode Shape of Configuration-7

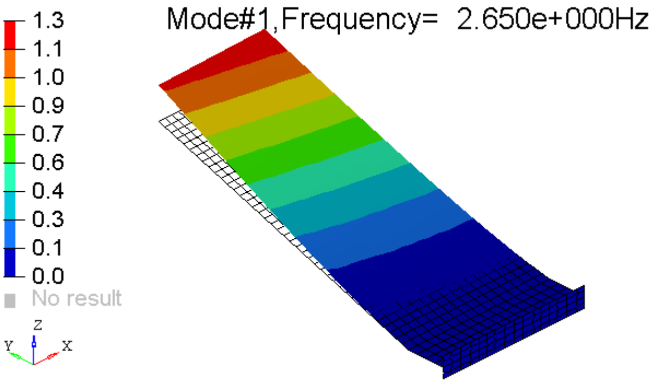
1.3
1.1
1.0
0.9
0.7
0.6
0.4
0.3
0.1
0.0
No result
Z
Y
X
Mode#1,Frequency= 2.650e+000Hz

Figure 0-31 Analysis 1st Bending Mode Shape of Configuration-8

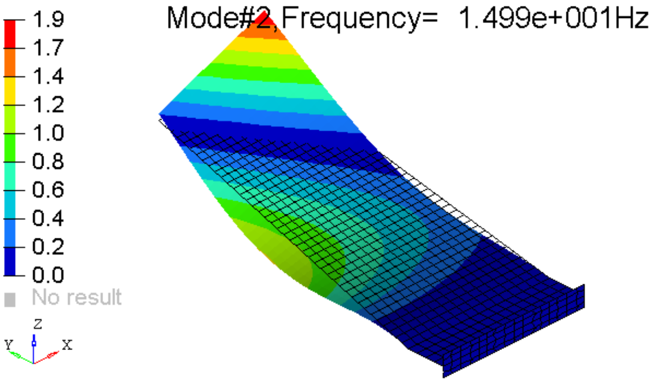
1.9
1.7
1.4
1.2
1.0
0.8
0.6
0.4
0.2
0.0
No result
Z
Y
X
Mode#2,Frequency= 1.499e+001Hz

Figure 0-32 Analysis 2nd Bending Mode Shape of Configuration-8

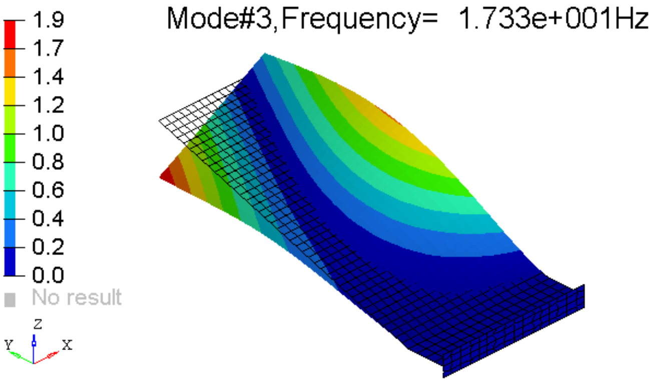
1.9
1.7
1.4
1.2
1.0
0.8
0.6
0.4
0.2
0.0
No result
Z
Y
X
Mode#3,Frequency= 1.733e+001Hz

Figure 0-33 Analysis Torsion Mode Shape of Configuration-8

E. Ground Vibration Test Mode Shapes

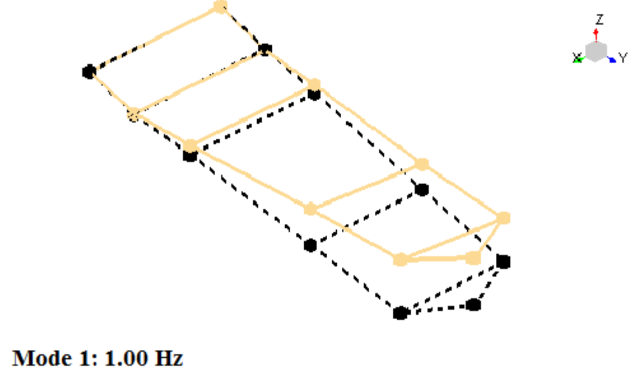
Z
X
Y
Mode 1: 1.00 Hz

Figure 0-34 Test 1st Bending Mode Shape of Configuration-2

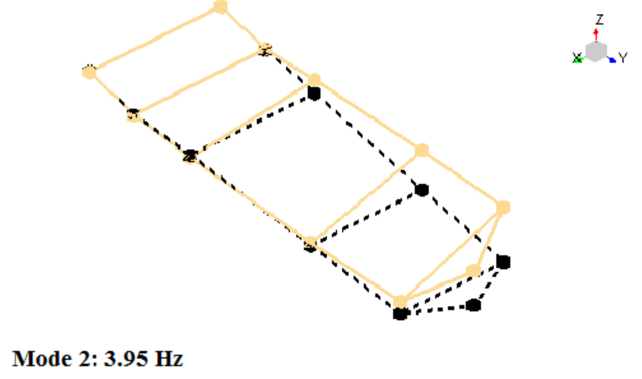
Z
X
Y
Mode 2: 3.95 Hz

Figure 0-35 Test Torsion Mode Shape of Configuration-2

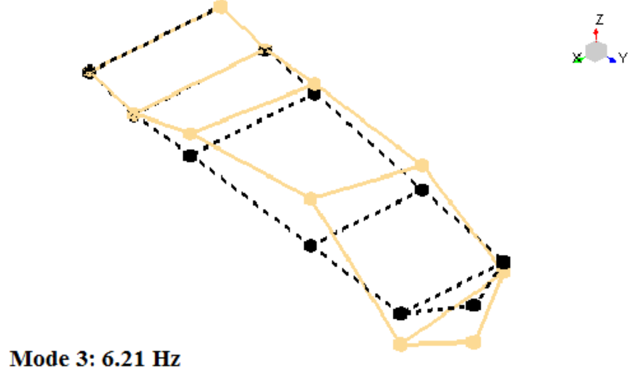
Z
X
Y
Mode 3: 6.21 Hz

Figure 0-36 Test 2nd Bending Mode Shape of Configuration-2

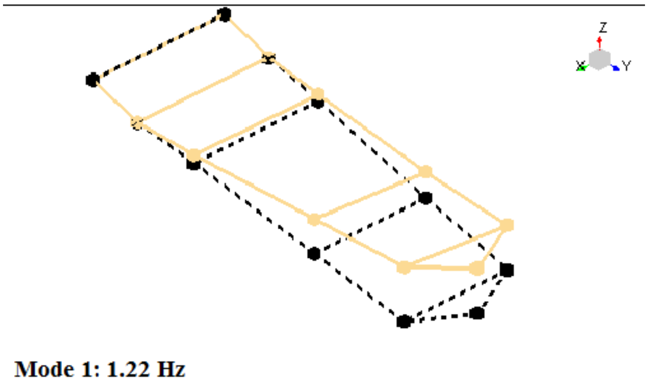
Z
X
Y
Mode 1: 1.22 Hz

Figure 0-37 Test 1st Bending Mode Shape of Configuration-3

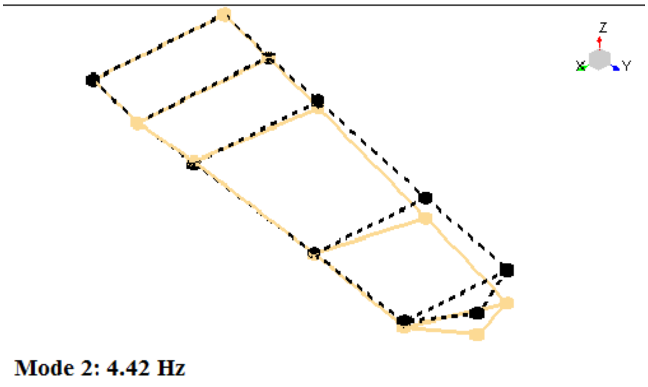
Z
X
Y
Mode 2: 4.42 Hz

Figure 0-38 Test Torsion Mode Shape of Configuration-3

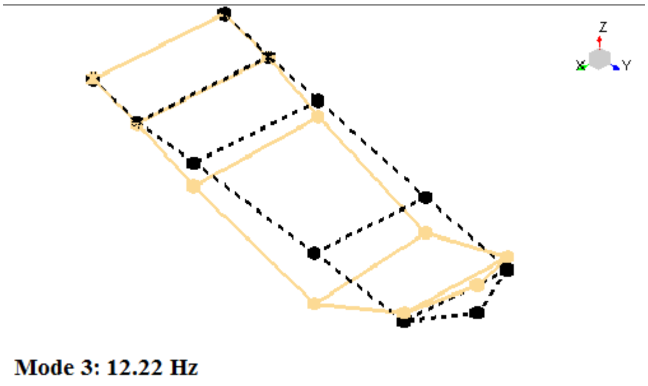
Z
X
Y
Mode 3: 12.22 Hz

Figure 0-39 Test 2nd Bending Mode Shape of Configuration-3

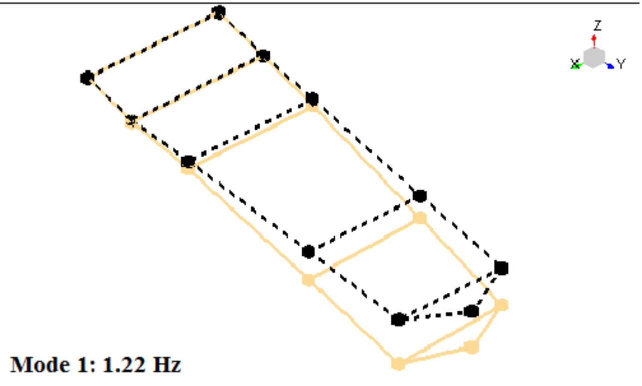
Z
X
Y
Mode 1: 1.22 Hz

Figure 0-40 Test 1st Bending Mode Shape of Configuration-4

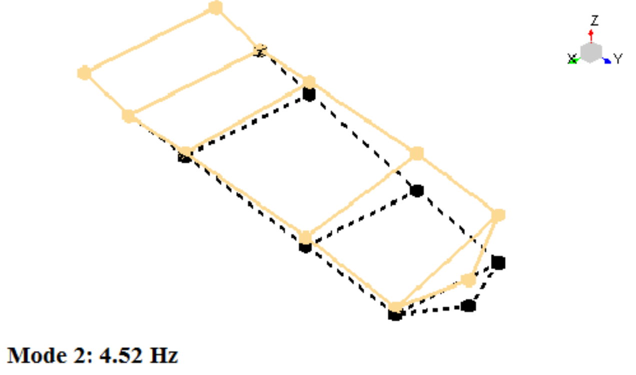
Z
X
Y
Mode 2: 4.52 Hz

Figure 0-41 Test Torsion Mode Shape of Configuration-4

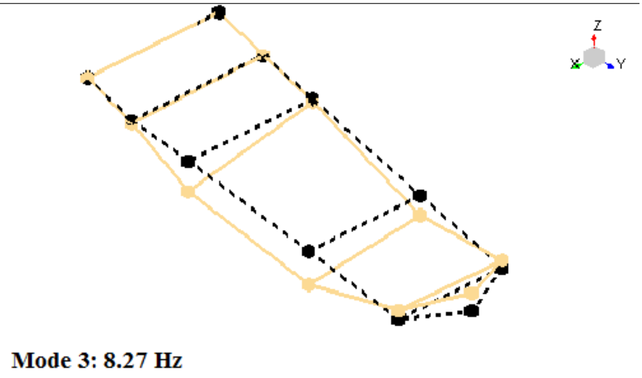
Z
X
Y
Mode 3: 8.27 Hz

Figure 0-42 Test 2nd Bending Mode Shape of Configuration-4

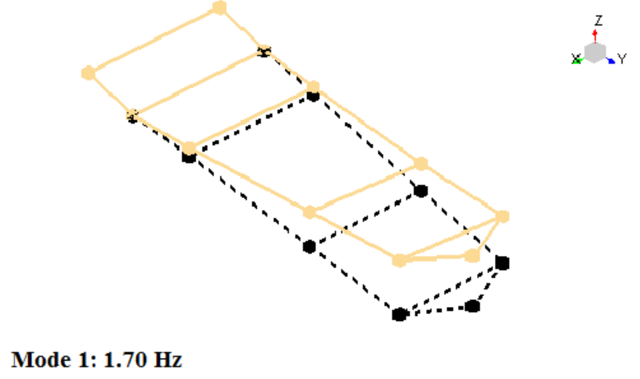
Z
X
Y
Mode 1: 1.70 Hz

Figure 0-43 Test 1st Bending Mode Shape of Configuration-5

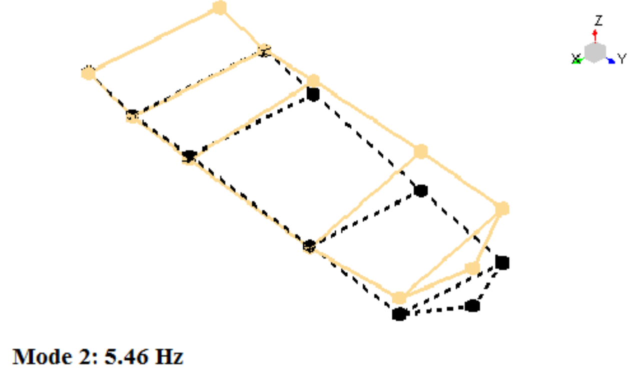
Z
X
Y
Mode 2: 5.46 Hz

Figure 0-44 Test Torsion Mode Shape of Configuration-5

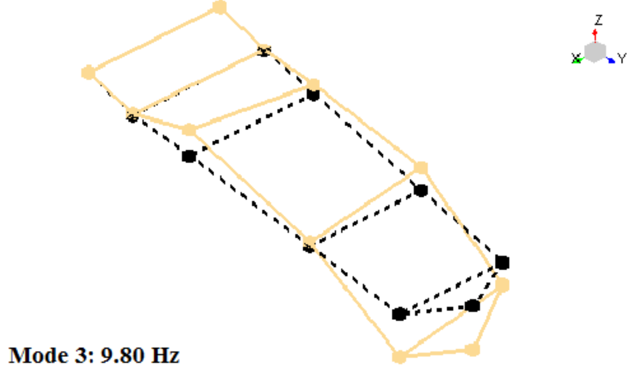
Z
X
Y
Mode 3: 9.80 Hz

Figure 0-45 Test 2nd Bending Mode Shape of Configuration-5

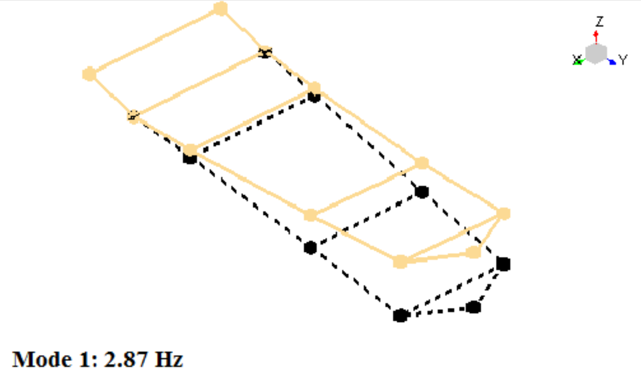
Z
X
Y
Mode 1: 2.87 Hz

Figure 0-46 Test 1st Bending Mode Shape of Configuration-6

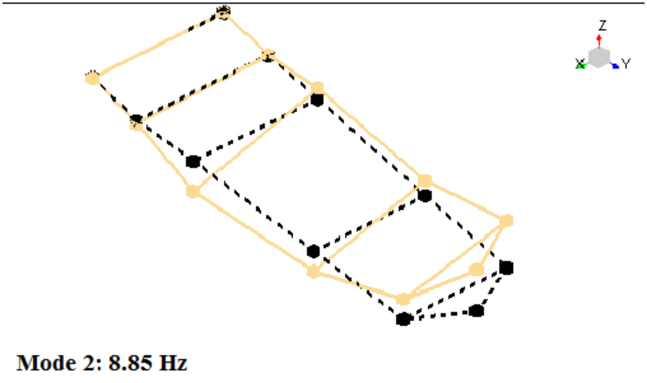
Z
X
Y
Mode 2: 8.85 Hz

Figure 0-47 Test Torsion Mode Shape of Configuration-6

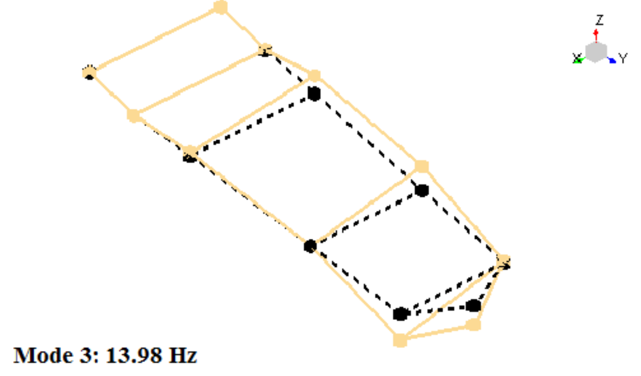
Z
X
Y
Mode 3: 13.98 Hz

Figure 0-48 Test 2nd Bending Mode Shape of Configuration-6

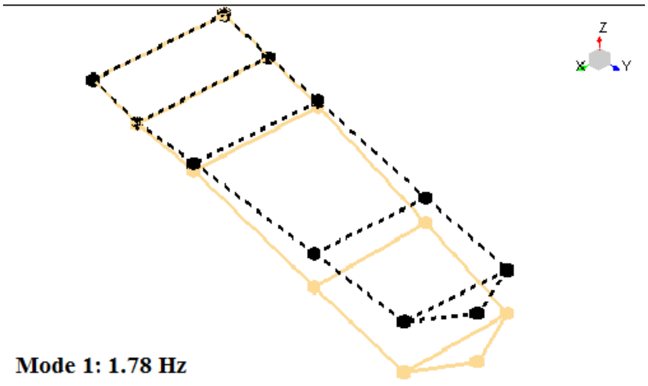
Z
X
Y
Mode 1: 1.78 Hz

Figure 0-49 Test 1st Bending Mode Shape of Configuration-7

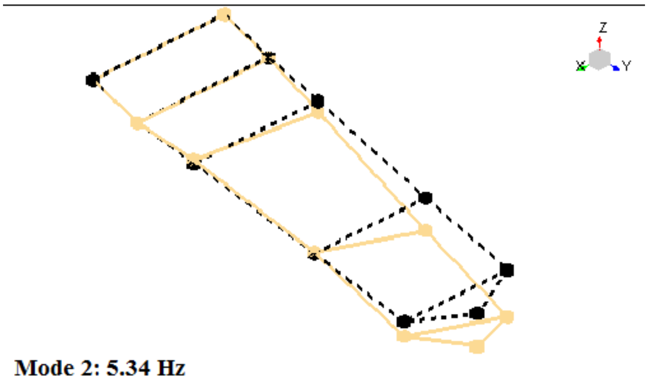
Z
X
Y
Mode 2: 5.34 Hz

Figure 0-50 Test Torsion Mode Shape of Configuration-7

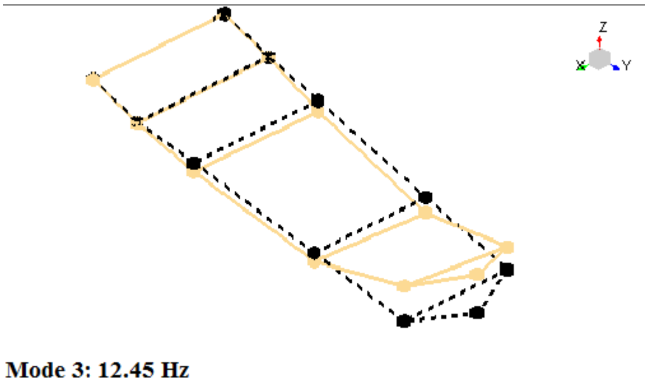
Z
X
Y
Mode 3: 12.45 Hz

Figure 0-51 Test 2nd Bending Mode Shape of Configuration-7

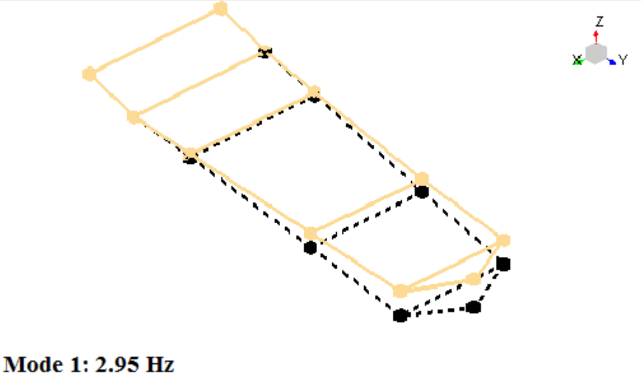
Z
X
Y
Mode 1: 2.95 Hz

Figure 0-52 Test 1st Bending Mode Shape of Configuration-8

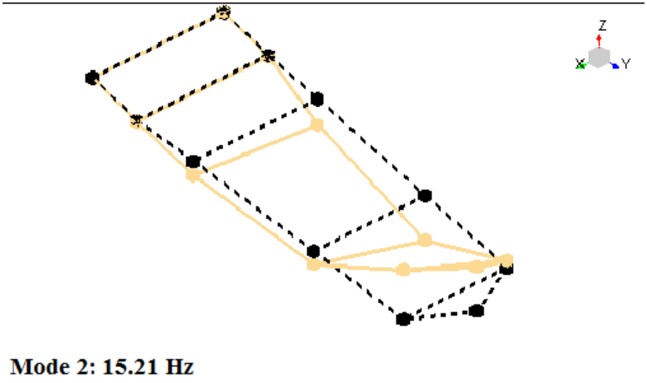
Z
X
Y
Mode 2: 15.21 Hz

Figure 0-53 Test 2nd Bending Mode Shape of Configuration-8

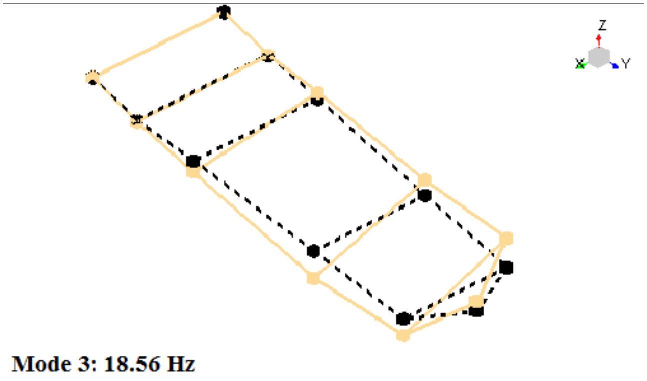
Z
X
Y
Mode 3: 18.56 Hz

Figure 0-54 Test Torsion Mode Shape of Configuration-8

F. Flutter Analysis Results with Not Updated Model, V-g and V-f Diagrams

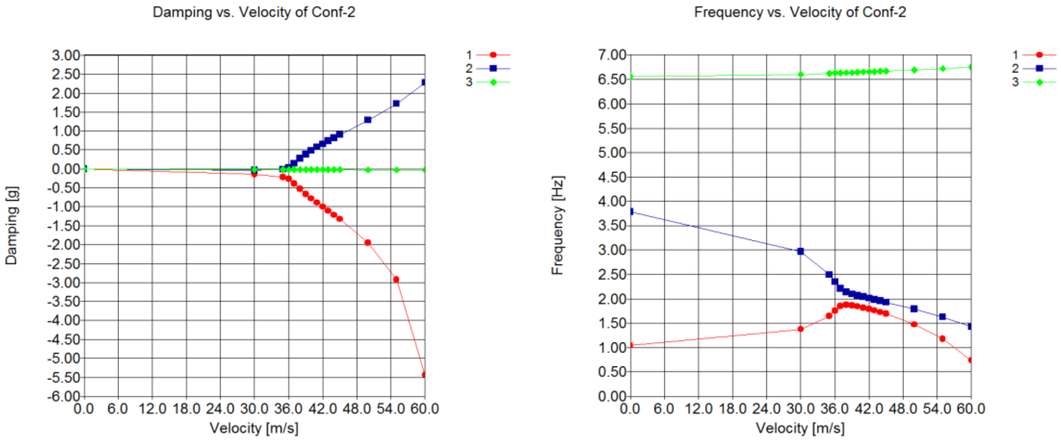

Figure 0-55 V-g and V-f Diagrams of Configuration-2

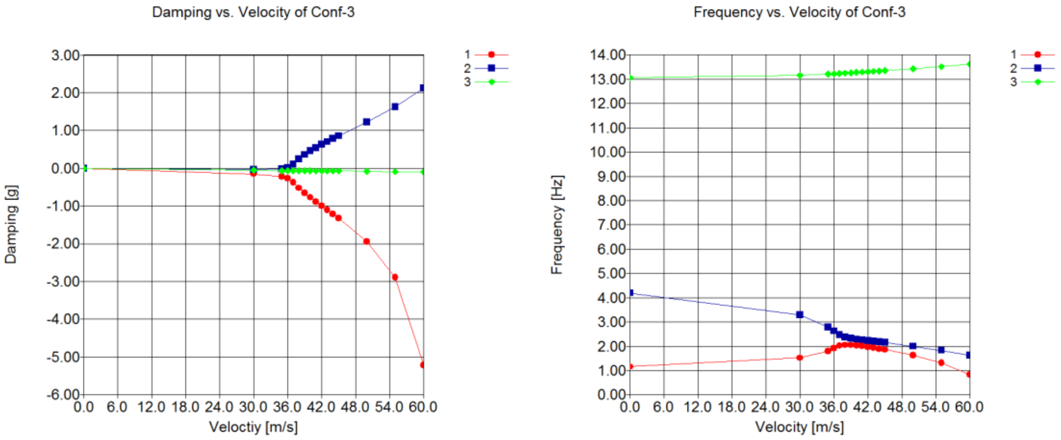

Figure 0-56 V-g and V-f Diagrams of Configuration-3

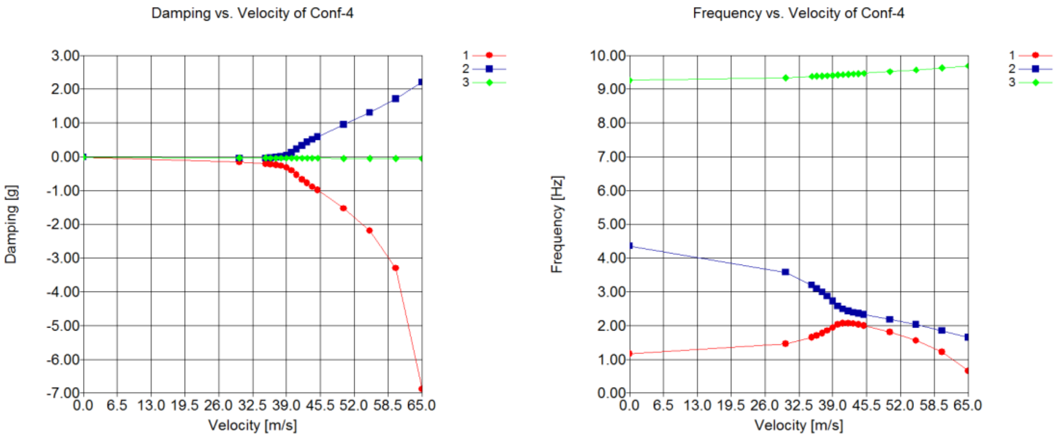

Figure 0-57 V-g and V-f Diagrams of Configuration-4

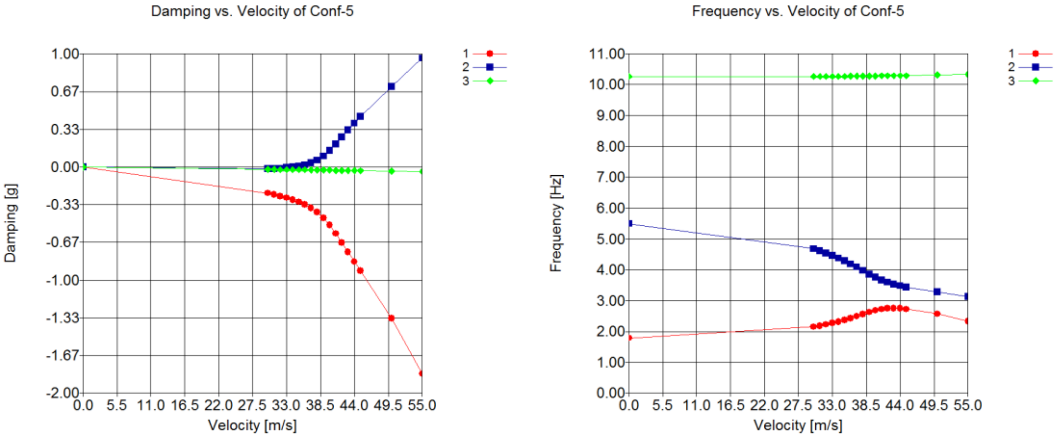

Figure 0-58 V-g and V-f Diagrams of Configuration-5

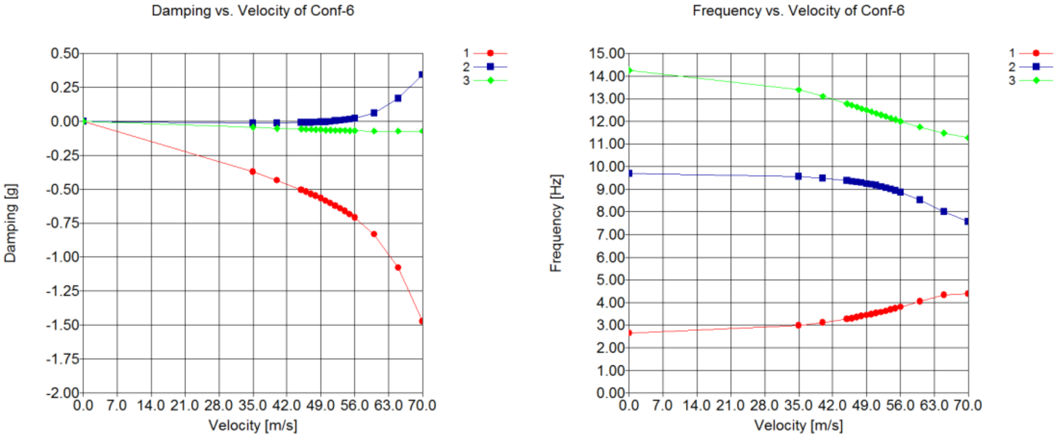

Figure 0-59 V-g and V-f Diagrams of Configuration-6

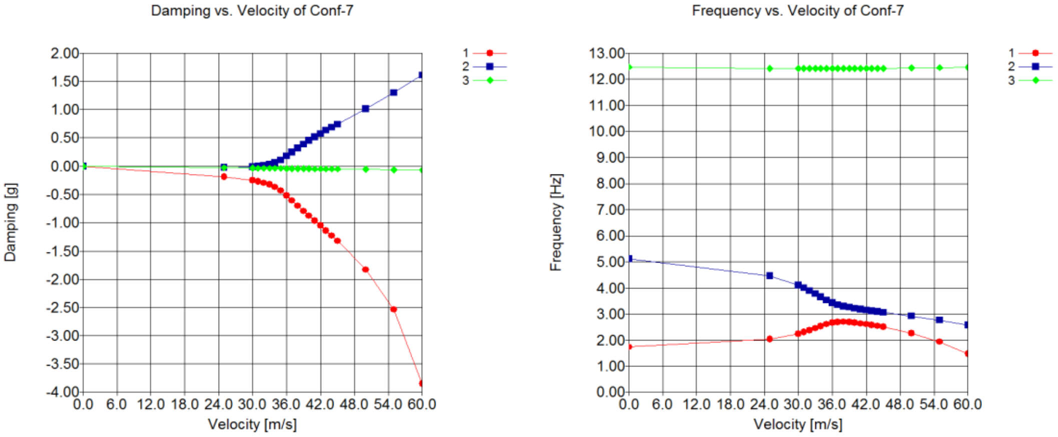

Figure 0-60 V-g and V-f Diagrams of Configuration-7

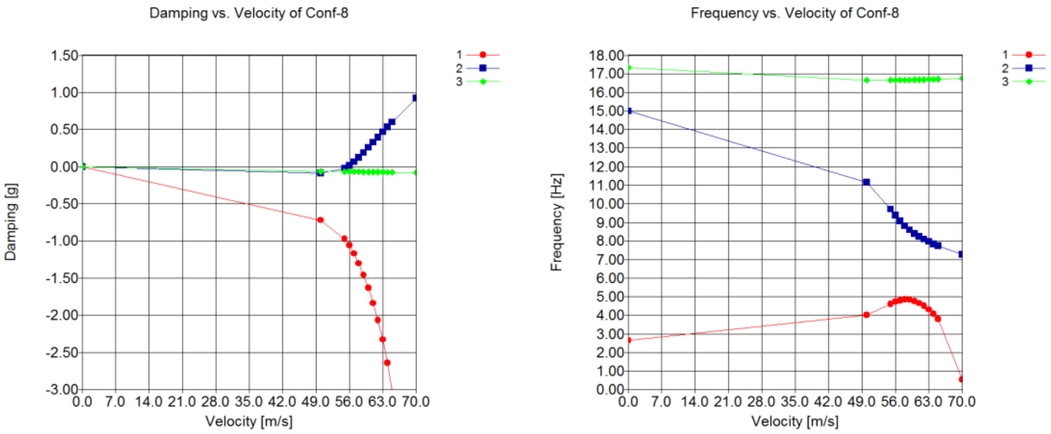

Figure 0-61 V-g and V-f Diagrams of Configuration-8

G. Wind Tunnel Flutter Tests, Strain Gage Time Histories and FFT Results

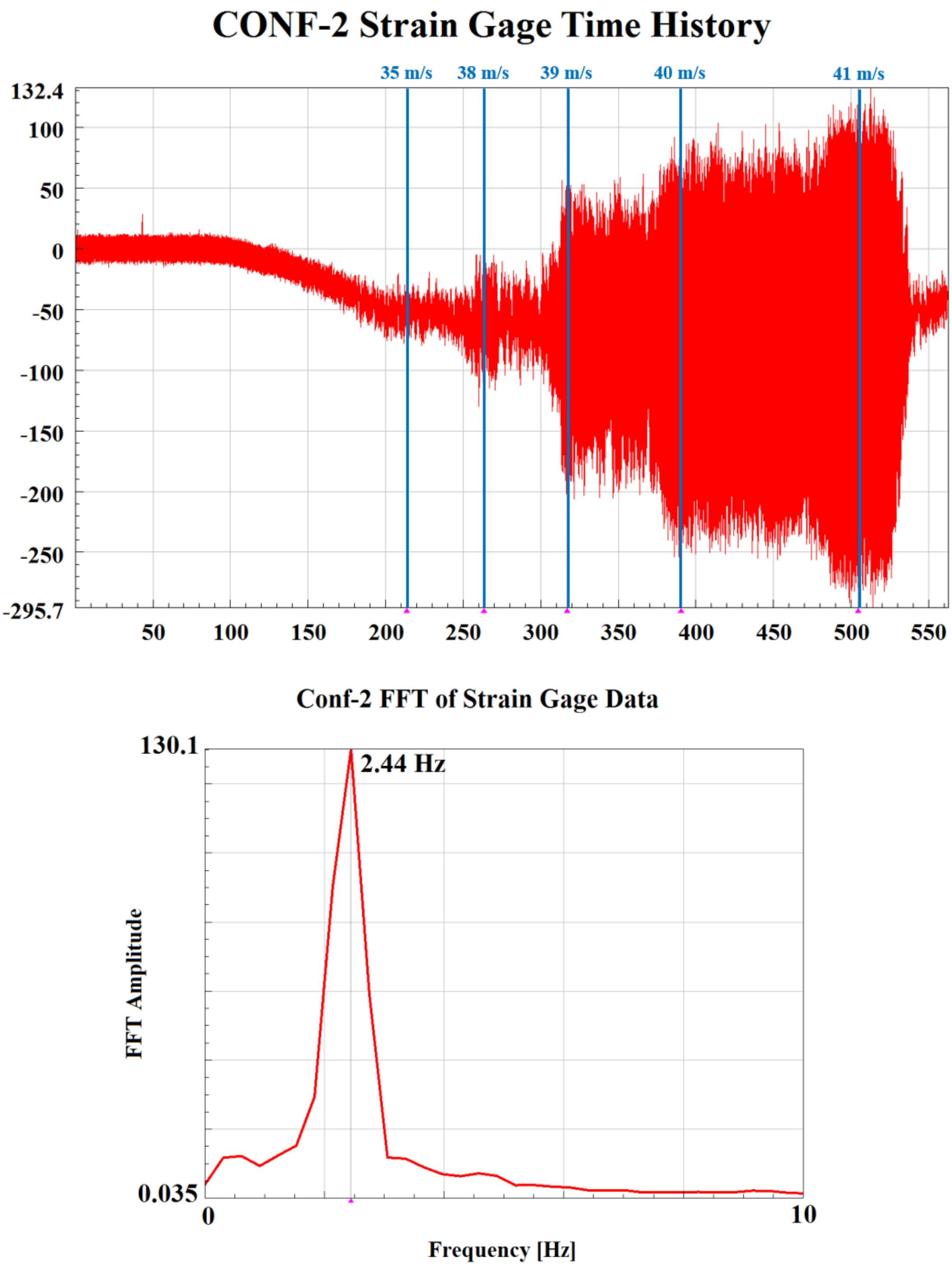

Figure 0-62 Strain Gage Time History and Its FFT Result of Configuration-2

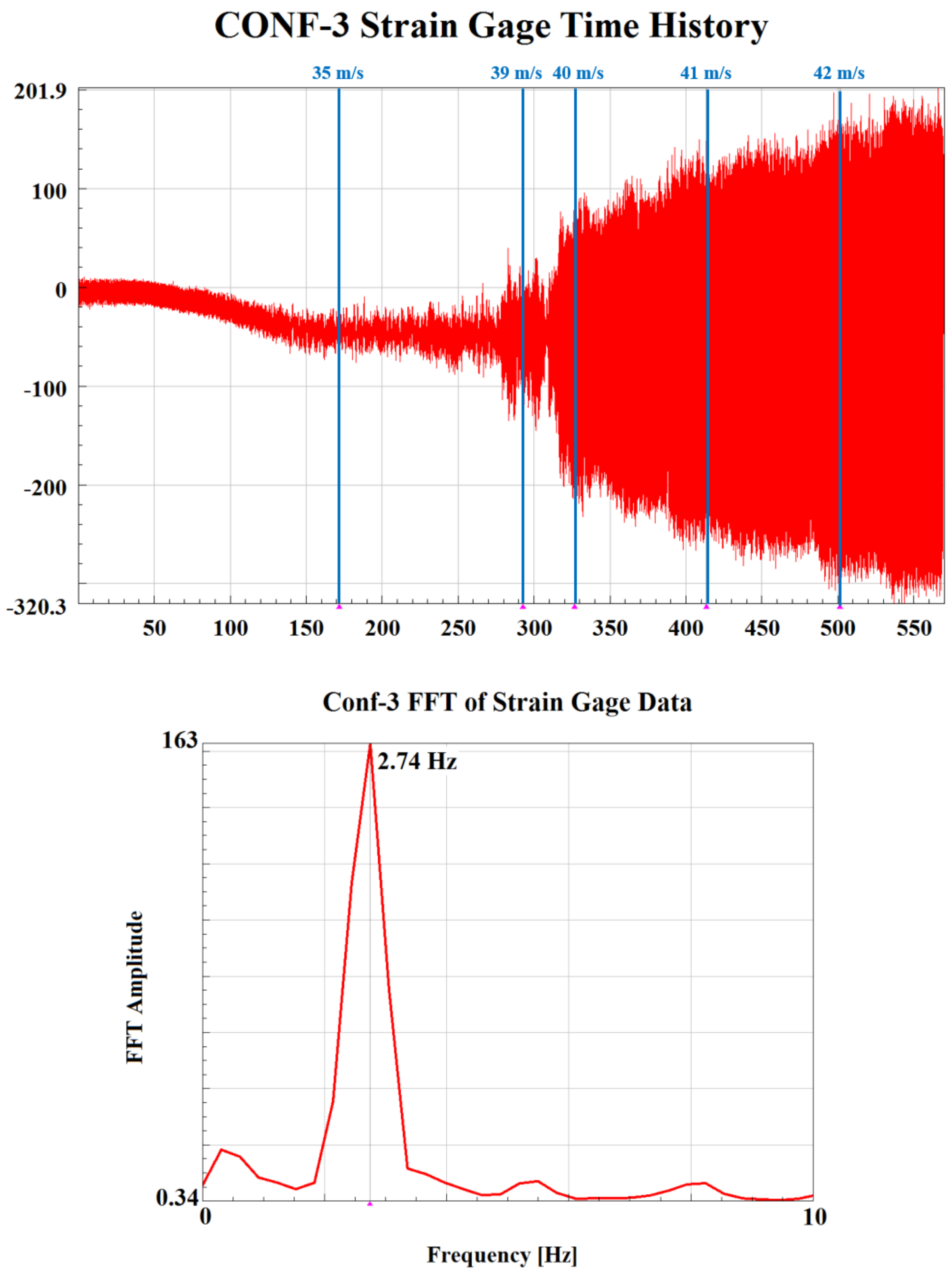

Figure 0-63 Strain Gage Time History and Its FFT Result of Configuration-3

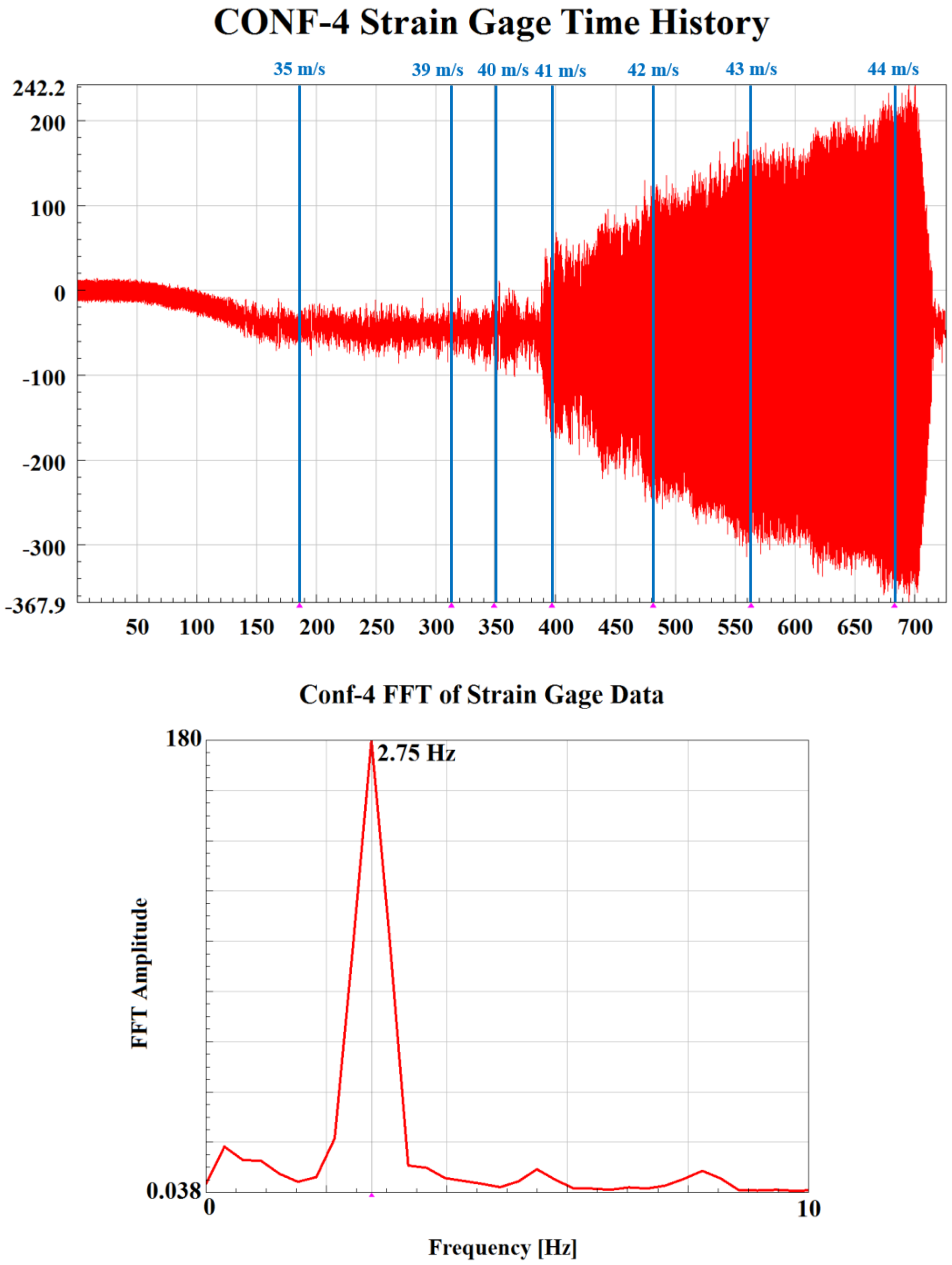

Figure 0-64 Strain Gage Time History and Its FFT Result of Configuration-4

CONF-5 Strain Gage Time History

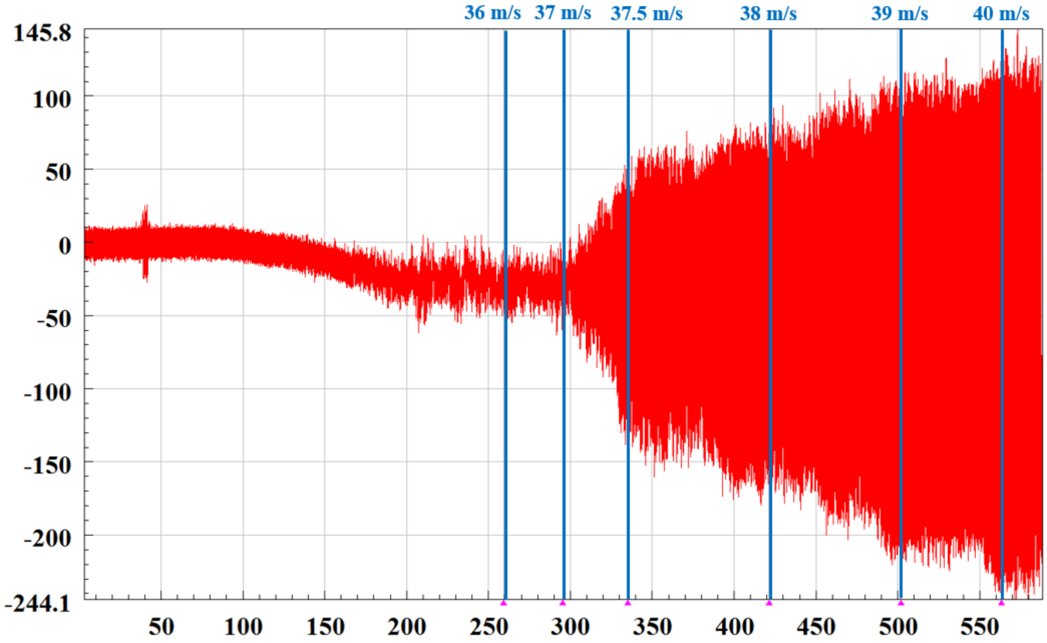

Conf-5 FFT of Strain Gage Data

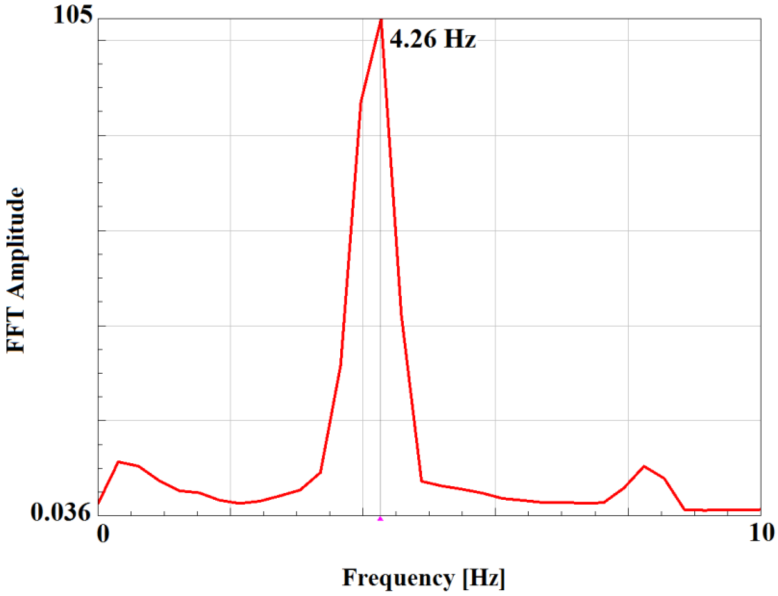

Figure 0-65 Strain Gage Time History and Its FFT Result of Configuration-5

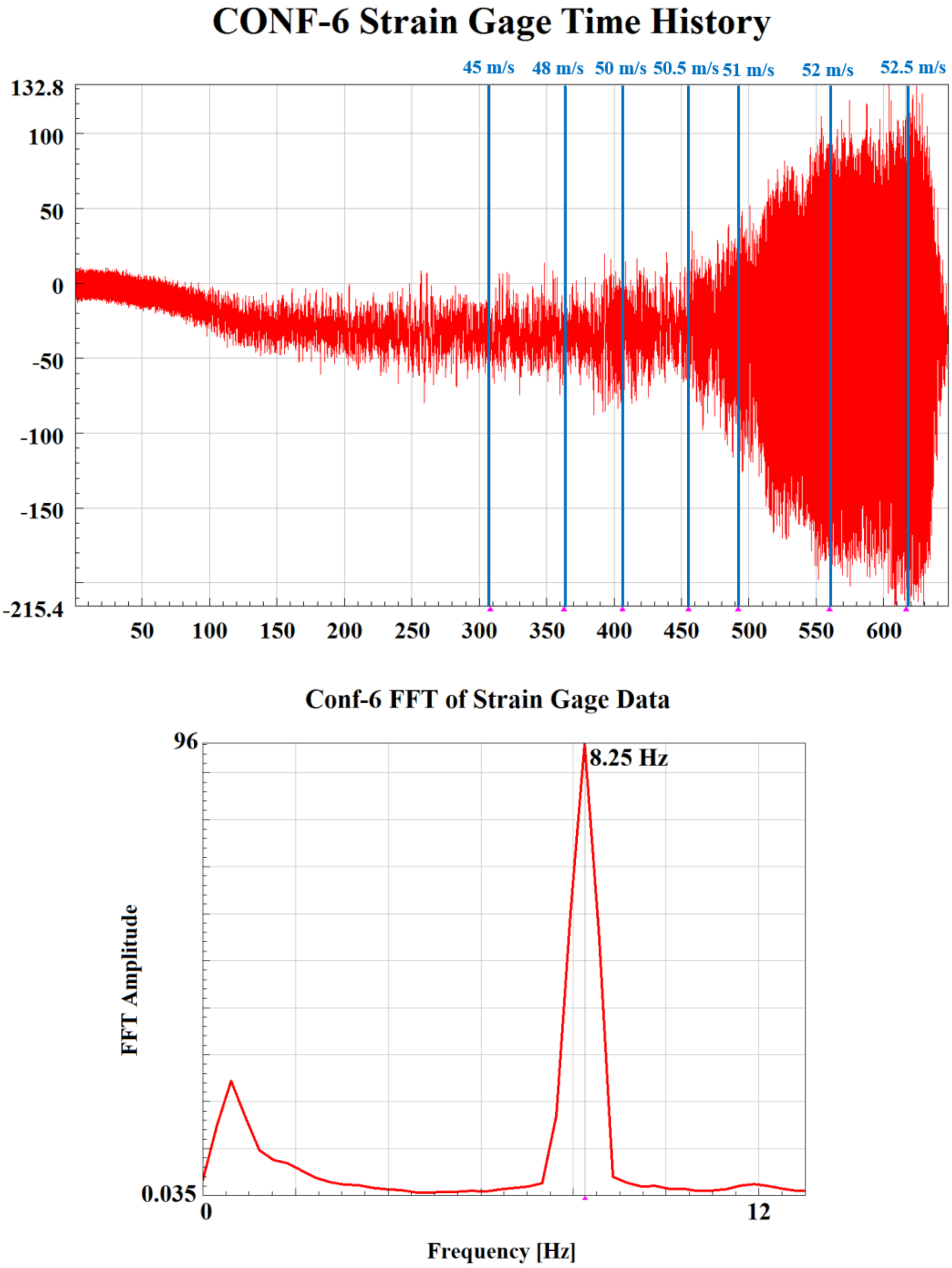

Figure 0-66 Strain Gage Time History and Its FFT Result of Configuration-6

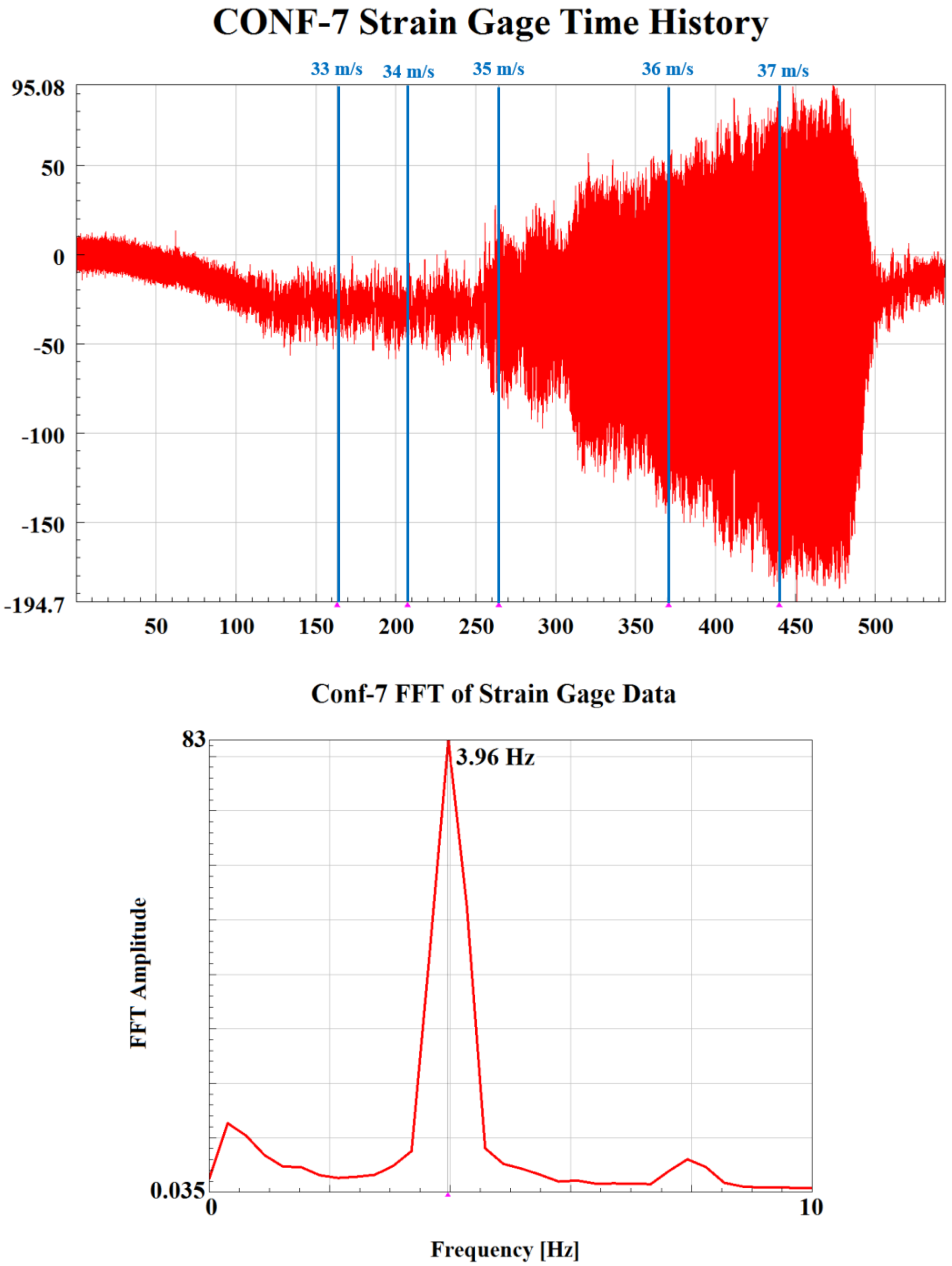

Figure 0-67 Strain Gage Time History and Its FFT Result of Configuration-7

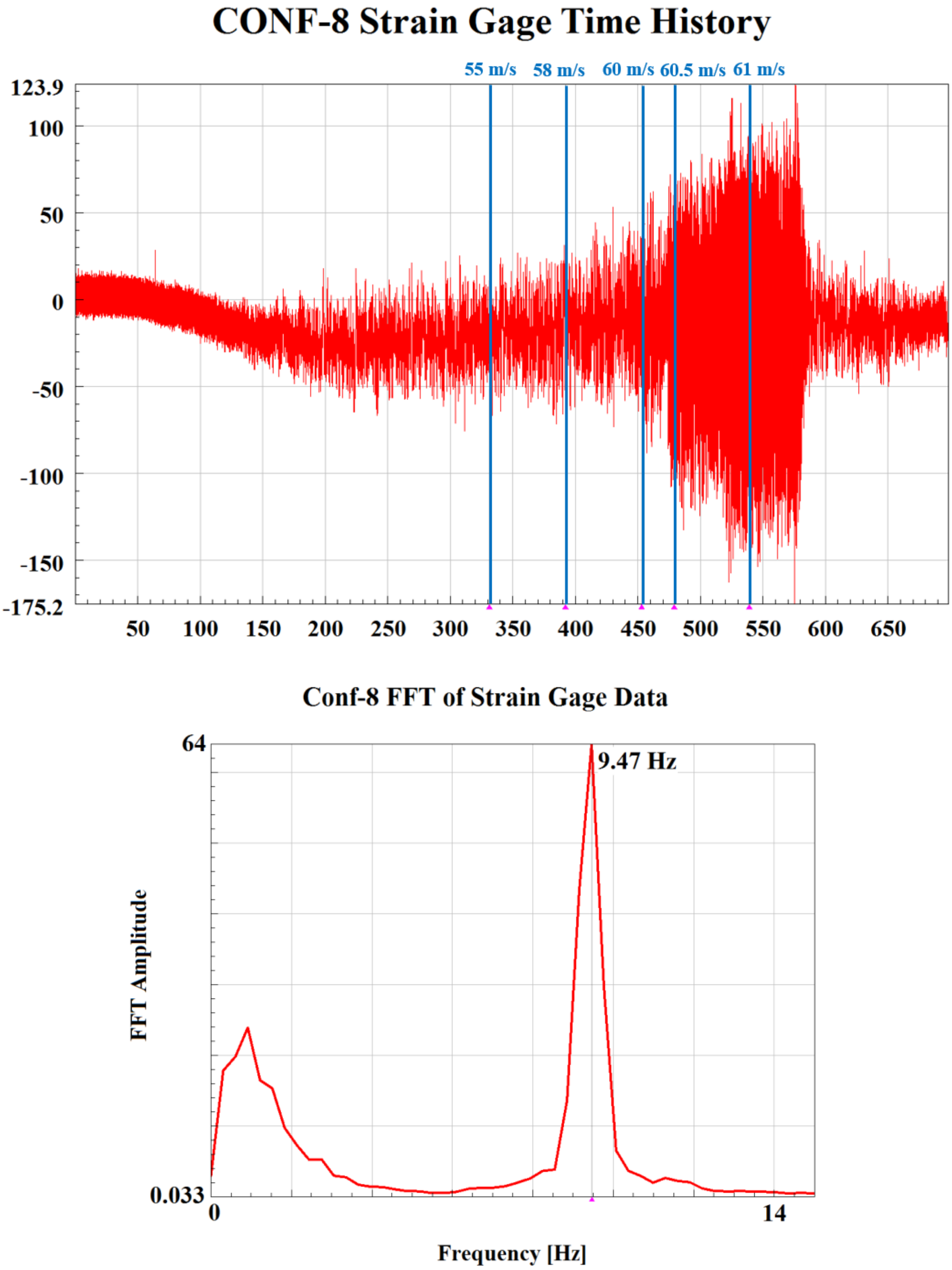
CONF-8 Strain Gage Time History

Conf-8 FFT of Strain Gage Data

Figure 0-68 Strain Gage Time History and Its FFT Result of Configuration-8